Development of a digital phase measuring system with microradian precision for LISA

Von der Fakultät für Mathematik und Physik der
Gottfried Wilhelm Leibniz Universität Hannover

zur Erlangung des Grades
Doktor der Naturwissenschaften
Dr. rer. nat.

genehmigte Dissertation
von

Dipl.-Phys. Joachim Kullmann

geboren am 19.10.1970 in Großburgwedel

2012

Abstract

LISA (Laser Interferometer Space Antenna) is a proposed spaceborne gravitational wave detector that will observe gravitational waves in the frequency range from 10^{-4} to $1\,\mathrm{Hz}$. The measuring principle of this detector is based on heterodyne interferometry with beat-note frequencies between 2 and $20\,\mathrm{MHz}$. The phase of these beat-notes has to be measured with microradian precision. For this purpose a high sensitive phase metrology system is required.

For this thesis a digital phasemeter based on a DPLL (Digital Phase-Locked Loop) designed at AEI Hannover was investigated and further developed.

The phase noise performance of this system was characterised by differential phase measurements between two electronically generated sinusoidal input signals that are split and applied to two channels (zero measurement). One of the dominant noise sources of the phasemeter was the time jitter noise of the ADC (Analog-to-Digital Converter) sampling process that directly induced phase noise. This noise contribution could successfully be corrected for in post-processing by using information about the differential time jitter obtained from a simultaneously injected calibration tone. The requirements were met even for signals generated by optical beat-notes of two offset phase-locked Nd:YAG NPRO lasers whereas a measurement using free running lasers showed excess phase noise. A further problem was the phase noise introduced by the analog front end electronics. Since the recommended transformers turned out to be unsuitable to reach the desired sensitivity other ADC driving schemes were investigated. A design based on the implementation of fully differential operational amplifiers (OpAmps) showed satisfying noise behaviour. The phase measuring system, including noise of the ADC driving units, met the desired requirements over the whole frequency range of interest (10^{-4} to $1\,\mathrm{Hz}$) for all chosen sinusoidal input signals with frequencies between 2 and $20\,\mathrm{MHz}$.

The sensitivity of the phasemeter was also characterised with respect to frequency modulated input signals which led to a 'common mode peak' in the spectrum obviously caused by differential delays between the ADC clock signals. This peak could successfully be removed by applying a time-delay correction scheme.

By imprinting a tiny phase modulation on one of the two input signals it was shown for the first time that a phase measuring system for LISA is capable of differentially detecting a tiny (sub-μrad) phase modulation in the presence of a LISA-like frequency drift while delivering the required performance.

Amplitude modulations and frequency modulations at certain frequencies were identified to cause additional peaks in the phase noise which could not be removed by any correction scheme.

The frequency noise of a free running Nd:YAG NPRO laser was measured by means of a balanced detector yielding the first results for Fourier frequencies between 1 and $20\,\mathrm{MHz}$.

keyword: LISA, phasemeter, laser noise

Kurzzusammenfassung

LISA (Laser Interferometer Space Antenna) ist ein satellitengestützter Gravitations-wellendetektor, der Gravitationswellen im Frequenzbereich von 10^{-4} bis $1\,\mathrm{Hz}$ messen wird. Das Messprinzip dieses Detektors basiert auf heterodyner Interferometrie wobei die Schwebungsfrequenzen zwischen 2 und $20\,\mathrm{MHz}$ liegen werden. Die Phasen dieser Schwebungssignale müssen mit einer Genauigkeit im Bereich von Mikroradian gemessen werden. Hierfür wird ein hochempfindliches Phasenmesssystem benötigt. Für die vorliegende Arbeit wurde ein am AEI Hannover entwickeltes, auf dem Prinzip einer DPLL (Digital Phase Locked Loop) basierendes, digitales Phasenmeter untersucht und weiterentwickelt.

Die Phasenempfindlichkeit dieses Systems wurde mittels differentieller Phasenmessungen an einem elektrischen Eingangssignal, das nach Aufsplittung in zwei Eingangskanäle eingebracht wurde, charakterisiert (Null-Messung). Eine der dominaten Rauschquellen war das zeitliche Schwanken der Abtast Zeitpunkte der AD-Wandler, welches unmittelbar zu Phasenrauschen führte. Mit Hilfe eines zeitgleich in das System eingebrachten Kalibrierungssignals konnte das differentielle zeitliche Schwanken des Abtastvorgangs bestimmt werden und so dieser Rauschbeitrag in der der Messung folgenden Datenbearbeitung eliminiert werden. Die Anforderungen konnten sogar für Signale, die aus Schwebungssignalen zweier phasengekoppelter Nd:YAG Laser resultierten, erfüllt werden. Die entsprechende Messung mit zwei freilaufenden Lasern wies ein zu hohes Rauschniveau auf. Als weiteres Problem stellte sich die den AD-Wandlern vorgeschaltete Elektronik heraus. Da die zum Ansteuern der AD-Wandler empfohlenen Transformatoren sich für die benötigte Empfindlichkeit als ungeeignet erwiesen, wurden andere Möglichkeiten untersucht. Nur Operationsverstärker erwiesen sich hierbei als ausreichend rauscharm. Selbst mit dem zusätzlichen Rauschbeitrag dieser Operationsverstärker genügte das Phasenmeter den Anforderungen über den gesamten Frequenzbereich von 10^{-4} bis $1\,\mathrm{Hz}$ für alle getesteten Eingangsfrequenzen zwischen 2 und $20\,\mathrm{MHz}$.

Die Empfindlichkeit des System wurde auch bezüglich frequenzmodulierter Eingangssignale charakterisiert. Trotz der symmetrischen Einbringung der Signale zeigte sich im Spektrum ein Peak bei der Modulationsfrequenz, der auf eine zeitliche Verzögerung zwischen den Taktsignalen der AD-Wandler zurückgeführt werden konnte. Mit Hilfe eines diesen Zeitversatz korrigierenden Algorithmus konnte dieser Peak eliminiert werden.

Durch Aufbringung einer sehr kleinen Phasenmodulation auf eines der beiden Eingangssignale, welche bereits eine Frequenzschwankung aufwiesen wie sie im Rahmen des LISA Projektes zu erwarten ist, konnte erstmals gezeigt werden, dass das System geignet ist, eine solche Phasenmodulation mit einer Amplitude unterhalb eines Mikroradian zu detektieren. Die Anforderungen an das Rauschverhalten des Systems wurden dabei nicht überschritten.

Desweiteren wurde das Frequenzrauschen eines freilaufenden Nd:YAG NPRO Lasers

für Fourier Frequenzen zwischen 1 und 20 MHz mit Hilfe eines sog. ausbalancierten Detektors gemessen.
Schlüsselwörter: LISA, Phasenmeter, Laserrauschen

Contents

Contents

List of Abbreviations and Acronyms

AAF : Anti-Aliasing Filter
ADC : Analog-to-Digital Converter
AEI : Albert Einstein Institute in Hannover
AU : Astronomical Unit
Balun: Balanced-unbalanced (converter)
DPLL : Digital Phase-Locked Loop
EPP: Enhanced Parallel Port
ESA : European Space Agency
FPGA : Field Programmable Gate Array
HW : Hardware
LISA : Laser Interferometer Space Antenna
LO : Local Oscillator
LPF : Lowpass Filter
LPSD : Linear Power Spectral Density
LSB : Least Significant Bit
LTP: LISA Technology Package
LUT : Look-Up Table
NCO : Numerically Controlled Oscillator
NPRO: Non-Planar Ring Oscillator
OLTF: Open Loop Transfer Function
OpAmp : Operational Amplifier
PA : Phase Accumulator
PAAM : Point-Ahead Actuator Mechanism
PCB: Printed Circuit Board
PD : Photo Detector
PIC : Proportional-Integral Controller
PIR : Phase Increment Register
PLL : Phase-Locked Loop
PMS : Phase Measurement System
pp: peak-to-peak
PRN : Pseudo-Random Noise
RF: Radio Frequency
rms: root mean square
SB: Sideband
SMD : Surface-Mounted Device
SNR : Signal-to-Noise Ratio
STF: System Transfer Function
TDI : Time Delay Interferometry
USO : Ultra Stable Oscillator
VHDL: Very high speed integrated circuit Hardware Description Language

Contents

10

List of Figures

1 Introduction

In this chapter the theory of gravitational wave propagation using the linearized weak field approximation and the effect of gravitational waves on free particles is briefly presented (section 1.1). In section 1.2 an overview of ground-based gravitational detectors and of LISA is given. LISA will be the first gravitational wave detector to operate in space.

Comprehensive reviews of gravitational wave detection can be found in [1],[2],[3].

1.1 Theoretical Background

1.1.1 Gravitational Waves in Linearized Theory

The description given here is based on [4],[5],[6] (see also e.g. [7],[8],[9]).

In General Relativity the paths of free particles are geodesics in the geometry of spacetime. The curvature of this spacetime (generated by all forms of energy and energy fluxes) is characterised by the metric $g_{\alpha\beta}$. For weak gravitational fields it can be approximated by a very small perturbation $h_{\alpha\beta}$ ($|h_{\alpha\beta}| \ll 1$) on the flat space-time (Minkowski) metric $\eta_{\alpha\beta} = \mathrm{diag}(-1,1,1,1)$:

$$g_{\alpha\beta} = \eta_{\alpha\beta} + h_{\alpha\beta}. \tag{1.1}$$

By defining the *trace-reverse*

$$\bar{h}_{\alpha\beta} := h_{\alpha\beta} - \frac{1}{2}\eta_{\alpha\beta}h \tag{1.2}$$

with $h := h^{\mu}{}_{\mu}$ the components of the Einstein tensor can be written as

$$G^{\alpha\beta} = -\frac{1}{2}\left(-\frac{\partial}{\partial t^2} + \Delta\right)\bar{h}^{\alpha\beta}. \tag{1.3}$$

Hence the Einstein field equations using geometrical units

$$G^{\alpha\beta} = 8\pi T^{\alpha\beta} \tag{1.4}$$

($T^{\alpha\beta}$ being the components of the stress-energy tensor) simplify to

$$\left(-\frac{\partial}{\partial t^2} + \Delta\right)\bar{h}^{\alpha\beta} = -16\pi T^{\alpha\beta}. \tag{1.5}$$

These are the field equations of *linearized theory*.

Far from any source of gravity in vacuum ($T^{\alpha\beta} \equiv 0$) Equation (1.5) becomes

$$\left(-\frac{\partial}{\partial t^2} + \Delta\right)\bar{h}^{\alpha\beta} = 0. \tag{1.6}$$

This wave equation has solutions of the form

$$\bar{h}^{\alpha\beta} = A^{\alpha\beta} e^{ik_\mu x^\mu}. \tag{1.7}$$

These solutions describe gravitational waves which do not exist in Newtonian theory. They travel at the speed of light.

By choosing appropriate gauge conditions ($\bar{h}^{\alpha\beta}{}_{,\beta} = 0$, Lorentz gauge) one can set restrictions on the waves' complex amplitude $A^{\alpha\beta}$:

$$A^{\alpha\beta} k_\beta = 0 \tag{1.8}$$

$$A^\alpha{}_\alpha = 0 \tag{1.9}$$

and

$$A_{\alpha\beta} U^\beta = 0 \tag{1.10}$$

for U^β being the components of some fixed four-velocity $\vec{U}$. Equations (1.8) to (1.10) are referred to as the *transverse-traceless gauge*. This gauge implies that

$$\bar{h}^{\alpha\beta} = h^{\alpha\beta} \tag{1.11}$$

and the amplitude of the wave simplifies to

$$(A_{\alpha\beta}) = \begin{pmatrix} 0 & 0 & 0 & 0 \\ 0 & A_{xx} & A_{xy} & 0 \\ 0 & A_{xy} & -A_{xx} & 0 \\ 0 & 0 & 0 & 0 \end{pmatrix} \tag{1.12}$$

for a wave travelling in z-direction. Such a wave having only A_{xx} components ($A_{xy} = 0$) is said to be '+'(plus)-polarised and a wave with amplitude components A_{xy} ($A_{xx} = 0$) is called '×'(cross)-polarised. The corresponding perturbations $h_{\alpha\beta}$ of the Minkowski metric $\eta_{\alpha\beta}$ can be written as

$$(h_{\alpha\beta}) = \begin{pmatrix} 0 & 0 & 0 & 0 \\ 0 & h_+ & 0 & 0 \\ 0 & 0 & -h_+ & 0 \\ 0 & 0 & 0 & 0 \end{pmatrix} \tag{1.13}$$

with $h_+ = A_{xx} e^{ik_\alpha x^\alpha}$ ('+'-polarisation) and

$$(h_{\alpha\beta}) = \begin{pmatrix} 0 & 0 & 0 & 0 \\ 0 & 0 & h_\times & 0 \\ 0 & h_\times & 0 & 0 \\ 0 & 0 & 0 & 0 \end{pmatrix} \tag{1.14}$$

with $h_\times = A_{xy} e^{ik_\alpha x^\alpha}$ ('×'-polarisation) and $\vec{k} = (\omega, 0, 0, \omega)$ for a wave propagating with velocity c in the z-direction.

How gravitational waves having one of these polarisation states affect free particles is explained in the next section.

1.1.2 Effects on free Particles

In can be seen from Equations (1.13) and (1.14) that the two polarisation states of a gravitational wave propagating in the z-direction yield line elements $ds^2 = g_{\alpha\beta}dx^\alpha dx^\beta$ of the form

$$ds^2 = -dt^2 + (1 + h_+)dx^2 + (1 - h_+)dy^2 + dz^2 \tag{1.15}$$

for the pure '+'-polarisation and

$$ds^2 = -dt^2 + (1 + h_\times)dxdy + (1 + h_\times)dydx + dz^2 \tag{1.16}$$

for the pure '×'-polarisation.

Such (time varying) metrics induce effects on the proper distance between geodesics marked by free test particles as shown in Figure 1.1. It shows the distortions of a
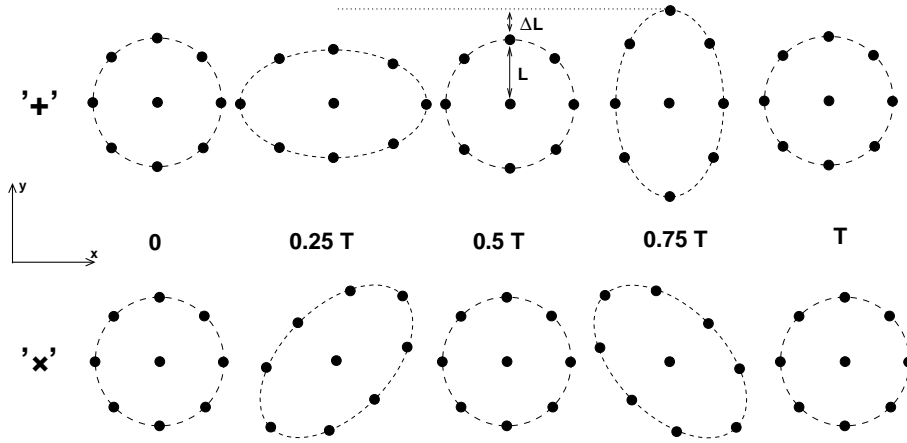
Figure 1.1: *The distortion of a circle of free particles in the rest frame of the centre particle due to tidal accelerations over one wave period T differs for the '+' and the '×'-polarisation. The ratio $\Delta L/L$ is defined as the strain of the wave.*

circle of testmasses for a '+' and a '×' polarised gravitational wave incident from the z-direction. These distortions are depicted for distinct times within a wave period T. Each of the test particles is assumed to be free falling. The figure depicts the tidal accelerations seen in the rest frame of the centre particle due to the time varying metric.

The amplitude of the wave (usually denoted as h) is defined as

$$h := 2\frac{\Delta L}{L} \tag{1.17}$$

whereas the relative deformation $\Delta L/L$ is called the *strain* of the gravitational wave.

1.2 Gravitational Wave Detectors

1.2.1 Ground-based Detectors

The first attempts to measure gravitational waves were based on the effects of varying tidal forces (explained above) on resonances of metal bars ('bar'-detectors). These

measurements were performed by Joseph Weber in the 1960s. Though increased in sensitivity until today these type of detectors could not reach the required sensitivity. Currently there are only 2 bar detectors in operation worldwide (Auriga and Nautilus).

The most promising method to measure the tiny changes in the test particle separation is to sense them by interferometry. A Michelson interferometer placed within the circle of test masses shown in Figure 1.1 is predestined to fulfil this task. In Figure 1.2 the corresponding measuring principle is sketched. The recombination beam splitter is located in the centre of the circle and the two mirrors of the interferometer act as 'test particles' moving on geodesics. (At least they should be free floating along the sensitive axis of the corresponding arm.) Such an interferometer measures the changes in the differential armlength caused by a gravitational wave. All interferometric ground-based detectors are based on the principle of a Michelson interferometer.

Figure 1.2: *Principle of measuring the tidal effects of a gravitational wave by means of a Michelson interferometer*

At present there is a whole network of those types of detectors in operation: the LIGO project (USA, 4 and 2 km armlength), GEO600 (Germany, 600 m), Virgo (Italy, 3 km) and TAMA300 (Japan, 300 m). These detectors search for gravitational waves in the bandwidth from about 10 Hz up to a few kHz. The lowest limit in frequency for these detectors is set by the Earth's Newtonian gravitational field which is too noisy. For a review of ground-based detectors based on interferometry see e.g. [10]. However, a large variety of the strongest and scientificly interesting sources are expected to emit gravitational radiation in the mHz range. To detect waves in this part of the gravitational spectrum it is necessary to go to space. LISA (Laser Interferometer Space Antenna) is a proposed space mission to detect gravitational radiation in the frequency band below 1 Hz (down to about 10^{-4} Hz) and will be presented below.

1.2.2 LISA

LISA is a space mission for the detection of gravitational waves in the frequency range from 10^{-4} to 1 Hz. It comprises three spacecraft (satellites) separated by $5 \cdot 10^6$ km forming an equilateral triangle. This constellation will orbit the sun at a distance of 1 AU and trailing the earth by 20° (see Figure 1.3). The three satellites are linked by laser beams forming *in principle* three giant Michelson interferometers. Recent cost saving studies also consider versions with 1 million km armlength and 4 links between 3 spacecraft. The reference points of these interferometers are free floating gold-platinum cubes shielded by the spacecraft from the suns radiation pressure and solar wind. 'Free floating' means that these cubes (referred to as 'test mass' or 'proof mass') are markers for geodesics. The proper distance between these geodesics will change when a gravitational wave passes the detector and the effect
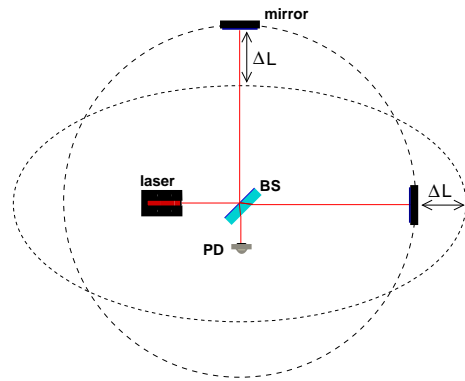
(the relative tidal acceleration of the test masses) will be sensed interferometrically. The received light at each satellite is already quite weak ($\sim$300 pW) after a travel of $5 \cdot 10^6$ km. This light can not be directly reflected back from the test masses since
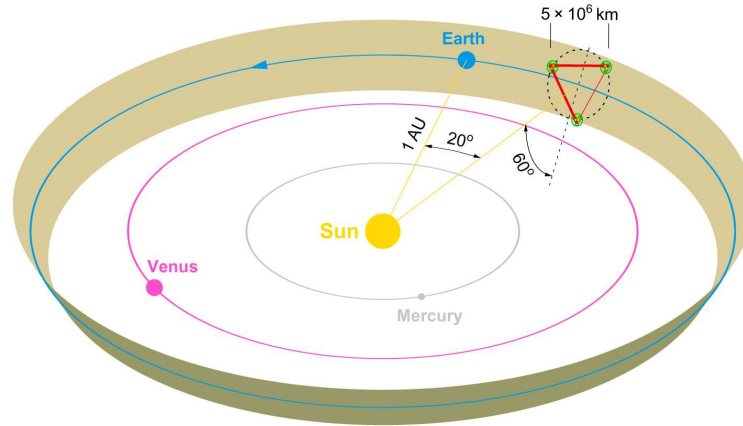
Figure 1.3: *The LISA constellation orbits the sun 20° behind the Earth. Its orbital plane is tilted relative to the ecliptic by 60°. The distance between Earth and satellites of approximately $50 \cdot 10^6$ km is a trade-off between minimisation of the Earth's gravitational influence and proper data communication.*

it would be too weak for detection after the second propagation along the arm. For that reason a transponder scheme is implemented meaning that a local laser is offset phase-locked to the received light coming from the remote satellite and sends back a frequency shifted copy of this light (preserving the phase information) with 2 W output power. The frequency shift between outgoing and incoming beam is necessary since due to the relative movement of the satellites (caused by their individual orbits) the interferometer can not be kept at a certain working point. Hence the principle of heterodyne detection has to be employed. It will be explained in chapter 2. The frequency shift guarantees that the heterodyne frequencies remain within a frequency range between 2 and 20 MHz.

LISA will make observations complementary to those of ground-based detectors. It will deliver information about the formation of intermediate black holes to generate massive black holes in galactic nuclei. It will explore the populations of stellar-mass compact objects in galactic nuclei and study the signals from thousands of stellar-mass close binaries in the galaxy. It will observe highly relativistic mergers of black holes binaries and will provide strong tests of General Relativity. LISA will also probe new physics and search for unforseen gravitational wave sources ([16]). It will open a new window to the universe.

2 Phasemeter Fundamentals

In this chapter the phasemeter developed and tested at AEI Hannover will be introduced. It will be explained why the phasemeter is an essential component for the LISA mission (section 2.1) and what the basic functioning principle is (section 2.2). After briefly presenting the hardware used (section 2.3) it will be shown that the system successfully passed the first fundamental functionality tests (section 2.4). Furthermore a theoretical description of the phase-locked loop (the logical core of the phasemeter) and the first adjustments performed will be presented (section 2.5).

2.1 Field of Applications in LISA

2.1.1 Overview

The interferometric science measurement of LISA is based on heterodyne interferometry (the basics will be explained in the next subsection) meaning that laser beams having different frequencies ν_1 and ν_2 are brought to interference which results in an optical beat-note of frequency $\Delta\nu = \nu_1 - \nu_2$. The phase of this beat-notes contain the desired information about optical pathlength changes caused by gravitational waves passing the detector.

The basic principle (omitting e.g. polarisation states of the laser beams) for the determination of these length changes between two test masses located on different satellites (single link) is sketched in Figure 2.1. The complete length measurement of one LISA link (transmit/receive) is divided into 3 parts:

- the distance measurement between the optical bench of one satellite (A) and the bench of the remote one (B),

- the distance measurement between the optical bench and the test mass of satellite A and of satellite B, respectively.

For the bench-to-bench measurement the light received by satellite B is used to offset phase-lock laser B on this incoming light. Then laser B sends a frequency shifted copy (maintaining the phase information) of the incoming light back to satellite A where it is interfered with the initial light from laser A (main science interferometer).

For determining the test mass motion relative to the optical bench the test mass interferometer and the reference interferometer are used. For this purpose the interference of the light from e.g., laser A with light received via a backlink fibre connection from the second laser onboard the same satellite is used as depicted in Figure 2.1.

For all these measurements the phase changes in the beat-notes with frequency $\Delta\nu$ have precisely to be determined by some phase measuring system.

Additionally this system must be able to
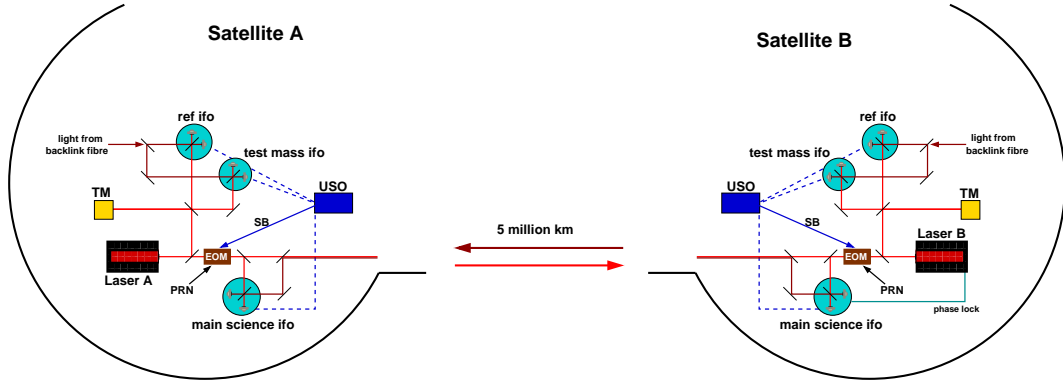
Figure 2.1: *The LISA science measurement is divided into 3 different length measurements: test mass to optical bench (satellite A), optical bench satellite A to optical bench satellite B and optical bench to test mass (satellite B).*

- track beat-notes between GHz-sidebands imprinted on the outgoing laser beams by means of the EOMs to compare clock noise between the USOs

- modulate and demodulate PRN codes for absolute distance measurements (ranging, see e.g. [24],[25]) between the satellites (input for TDI, see e.g. [23])

- measure beam misalignment in the science interferometer, the test mass interferometer and the PAAM (not sketched in Figure 2.1) by differential wavefront sensing ([26],[27])

- deliver output for offset phase-lock of lasers

- prepare filtered and downsampled data for transmission to ground

This thesis is focused on the determination of phase changes in electrical signals obtained from the optical main and sideband beat-notes. Due to Doppler shifts caused by the relative motion of the satellites (the 'breathing' of the LISA constellation) these beat notes will have frequencies between 2 and 20 MHz with a maximum Doppler drift of 4 Hz/s.

2.1.2 Main Science Measurement

The principle of a heterodyne beat-note measurements is depicted in Figure 2.2. The interference of two light fields having frequencies $\omega_{\mathrm{LO}} = 2\pi\nu_{\mathrm{LO}}$ (local oscillator, laser A) and $\omega_{\mathrm{R}} = 2\pi\nu_{\mathrm{R}}$ and phases φ_{LO} and φ_{R} yields a photocurrent (assuming a perfect 50:50 beamsplitter and 100% contrast)

$$I_{\mathrm{PD}} \quad \propto \quad \frac{1}{2}E_{\mathrm{LO}}{}^2 + \frac{1}{2}E_{\mathrm{R}}{}^2 + E_{\mathrm{LO}}E_{\mathrm{R}}\sin(\Delta\omega t + \Delta\varphi) \tag{2.1}$$

$$\propto \quad \frac{1}{2}P_{\mathrm{LO}} + \frac{1}{2}P_{\mathrm{R}} + \sqrt{P_{\mathrm{LO}}P_{\mathrm{R}}}\sin(\Delta\omega t + \Delta\varphi) \tag{2.2}$$

where P denotes the power of the light beams, $\Delta\omega = \omega_{\mathrm{R}} - \omega_{\mathrm{LO}}$ the difference between the angular frequencies of the two light fields and $\Delta\varphi = \varphi_{\mathrm{R}} - \varphi_{\mathrm{LO}}$ the

corresponding phase differences. This photocurrent is converted into a voltage by means of a transimpedance amplifier (attached to the photodetector) and is input for the phasemeter. The noise contribution of this phasemeter must not exceed $2\pi\,\mu\mathrm{rad}/\sqrt{\mathrm{Hz}}$ between $0.3\,\mathrm{mHz}$ and $1\,\mathrm{Hz}$ Fourier frequency per readout channel (this requirement corresponds to approximately $1\,\mathrm{pm}/\sqrt{\mathrm{Hz}}$ and will be derived in the beginning of chapter 3). The important phase information is contained in $\Delta\varphi = \varphi_{\mathrm{R}} - \varphi_{\mathrm{LO}}$ since φ_{R} is the phase the light has picked up on its way to the remote satellite and back. This phase can be converted into optical pathlength information ΔL by

$$\Delta L = \frac{\lambda}{2\pi} \cdot \Delta\varphi \tag{2.3}$$

where λ is the wavelength of the laser light.
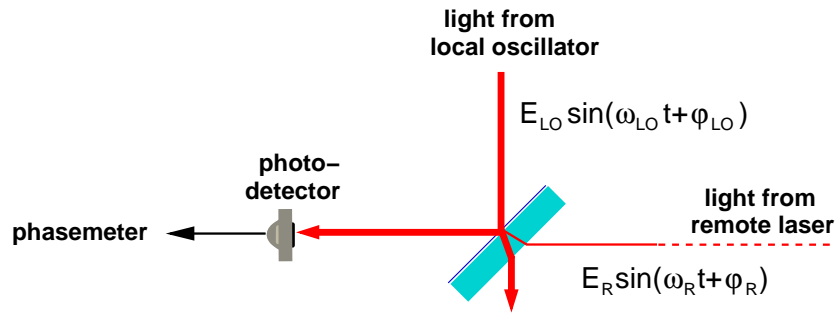
Figure 2.2: *The light from the local oscillator interferes with the received light from the remote laser yielding a beat-note with angular frequency $\Delta\omega = \omega_{\mathrm{R}} - \omega_{\mathrm{LO}}$. The phase of this beat-note contains the desired information about optical pathlength changes caused by gravitational waves. The interference pattern at the second port of the beamsplitter contains basically the same information and will also be sensed by an equivalent system for increased SNR and hot redundancy.*

2.2 Phase-Locked Loop Basics

2.2.1 Possible Phase Detection Techniques

As mentioned above the phasemeter has to measure the phase of beat-note signals with frequencies between 2 and $20\,\mathrm{MHz}$ having a maximum frequency drift of $4\,\mathrm{Hz/s}$. It has to be capable to simultaneously track 3 of these tones (main beat-note and two sideband beat-notes) plus the pilot tone being present in one and the same input signal. Additionally the PRN code has to be demodulated. The required PMS sensitivity for the main beat-note detection is $6\,\mu\mathrm{rad}/\sqrt{\mathrm{Hz}}$ (this will be derived in the beginning of chapter 3). For the other tones there are relaxed requirements.

Since this phase measuring system has to store and transmit data and since it should be easy to modify it for testing purposes, a *digital* system is the preferred choice.

There are basically 3 different digital phase detection methods that have been investigated by different experimental groups: zero crossing timing, use of the LTP phasemeter and a DPLL (Digital Phase-Locked Loop).

The zero crossing timing ([31],[28]) measures the time between the zero crossing of

an AC signal with respect to a reference clock. The main drawback of this methods amongst others is that it is unsuitable for tracking multiple tone signals.

The use of the LTP phasemeter ([30],[29]) requires a downmixing of the input signal to a fixed frequency of a few kHz before phase detection. This in turn requires a variable PLL due to the variable input frequency. Another disadvantage is that due to the 'image frequency' ending up at the signal frequency as well, the SNR will be reduced by a factor of $\sqrt{2}$ which is not acceptable.

The most promising method capable to fulfil all the desired tasks without any apparent drawbacks is a Digital Phase Locked Loop (DPLL) which is under investigation by several groups[1] worldwide ([32],[33],[34],[35],[36]).

2.2.2 Working Principle DPLL

The Digital Phase Locked Loop is a digital feedback control system that tracks the phase of an incoming digitised signal by trying to keep the error signal (out$_{\text{LPF}}$) at zero. A block diagram of such a control loop is sketched in Figure 2.3. It comprises a digital mixer (multiplier), a LPF, a PI (Proportional-Integral) Controller, a PIR (Phase Increment Register), a Phase Accumulator (PA) and a Sine Look-Up-Table (LUT). The entity consisting of the PIR, the PA and the LUT is referred to as NCO (Numerically Controlled Oscillator).
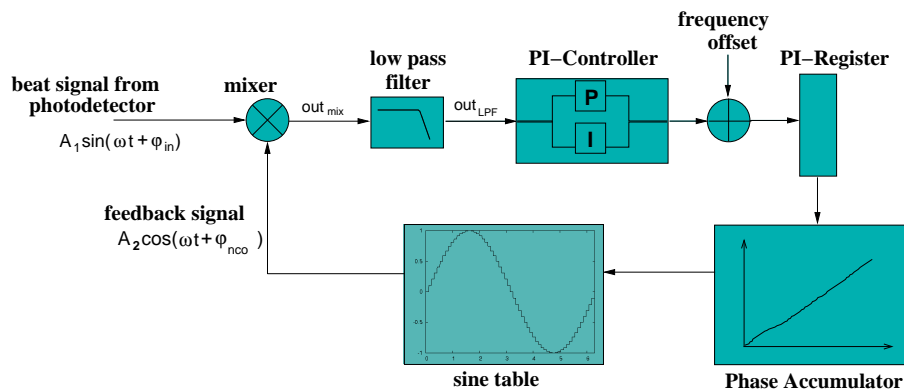
Figure 2.3: *A PLL is feedback control system that tracks the incoming signal by generating a feedback signal that matches (despite of a 90° phase shift) the phase of the input signal. It only works in closed loop condition*

A phase difference between the incoming and the feedback signal (assuming that their angular frequencies ω are equal, which should be the case if the system tracks the input signal properly) leads to a mixer output of

$$\text{out}_{\text{mix}} = A_1 \sin(\omega t + \varphi_{\text{in}}) \cdot A_2 \cos(\omega t + \varphi_{\text{nco}}) \tag{2.4}$$

$$= \frac{1}{2} A_1 A_2 [\sin(\varphi_{\text{in}} - \varphi_{\text{nco}}) + \sin(2\omega t + (\varphi_{in} + \varphi_{\text{nco}}))] \tag{2.5}$$

---

[1]NASA/JPL, University of Florida and AEI Hannover

which gives after low pass filtering

$$
\begin{aligned}
\text{out}_{\text{LPF}} &= \frac{1}{2} A_1 A_2 \sin(\varphi_{\text{in}} - \varphi_{\text{nco}}) && (2.6)\\
&= \frac{1}{2} A_1 A_2 \sin \Delta\varphi && (2.7)\\
&\approx \frac{1}{2} A_1 A_2 \Delta\varphi && (2.8)
\end{aligned}
$$

This is the error signal of the loop which depends linearly on the signal amplitudes and also *linearly* on the phase error $\Delta\varphi$ for small phase differences. This linearity is a precondition to analyse the system by the concept of a transfer function. This error signal (Equation (2.8)) is amplified (PIC), a frequency offset value is optionally added (to help the system to get into lock) and the resulting value is sent to the PIR. The values of the PIR (which are a measure for the current NCO frequency) are integrated in the PA giving the phase ramp that can be seen in Figure 2.3. The fractional part (of one cycle) of the PA addresses the LUT where the amplitude values of one cycle of a sine wave are stored (see also Figure 2.5 of section 2.2.4). This yields a sinusoidal output that is mixed with the incoming signal.

The NCO output is basically a 90° phase-shifted copy of the input signal (the *quadrature* signal Q). Any phase deviation $\Delta\varphi$ between the incoming and the NCO signal will lead to a change in the NCO output phase to suppress this error. Direct readout of the phase of this feedback signal yields the desired phase information about the input signal. The main benefit of this architecture is that the analog phase of the input signal is converted into digital form. The readout and phase reconstruction schemes will be explained in section 2.2.4. This digital PLL is implemented on an FPGA (Field Programmable Gate Array) chip using the VHDL Programming language.

One PLL is able only to track *one* signal. For e.g. 4 different signals to be tracked there need to be 4 PLLs implemented on the FPGA chip. In the remainder of this thesis the DPLL will also be denoted just as 'PLL' or 'PLL core'.

2.2.3 PLL Core Description

The principle of how a PLL tracks an incoming signal is based on the Quadrature ('Q') mixing scheme since the incoming signal and the feedback signal are 90° (quadrature) out of phase. To completely analyse an incoming signal the In-Phase ('I') mixer output (containing information about the signal's amplitude) should also be considered. Figure 2.4 shows a complete overview over a PLL and depicts how all necessary information to completely characterise the tracked signal are obtained:

- The **PA Register** contains information of the phase of the incoming signal plus a phase offset due to the lock-in process. Its fractional phase can be used to determine the differential phase between two PLL channels for e.g. differential wavefront sensing.

- The **PI Register** contains the phase increment (the 'phase step') during one NCO duty cycle. Basically this is the information about the instantaneous frequency of the signal.

- The **I-mixer readout** is a measure for the current amplitude of the input signal. It is obtained by multiplying the digitised input signal with the *in-phase* feedback signal giving an mixer output of

$$
\begin{aligned}
\mathrm{out_{mix}} &= A_1 \sin(\omega t + \varphi_{\mathrm{in}}) \cdot A_2 \sin(\omega t + \varphi_{\mathrm{nco}}) && (2.9) \\
&= \frac{1}{2} A_1 A_2 [\cos(\varphi_{\mathrm{in}} - \varphi_{\mathrm{nco}}) - \cos(2\omega t + (\varphi_{in} + \varphi_{\mathrm{nco}}))] && (2.10)
\end{aligned}
$$

which gives after low pass filtering ('$2f$-filter' meaning that the signal having the sum-frequency of the input signals is rejected)

$$
\begin{aligned}
\mathrm{out_{LPF}} &= \frac{1}{2} A_1 A_2 \cos(\varphi_{\mathrm{in}} - \varphi_{\mathrm{nco}}) && (2.11) \\
&= \frac{1}{2} A_1 A_2 \cos\Delta\varphi && (2.12) \\
&\approx \frac{1}{2} A_1 A_2 && (2.13)
\end{aligned}
$$

for small $\Delta\varphi$.

- The **Q-mixer readout** is the error signal of the loop proportional to $\frac{1}{1+G(s)}$ where $G(s)$ is the Open Loop Gain. For $G(s)$ being infinite this signal would be zero. If necessary, this readout can be used in combination with the 'I'-readout to correct for the phase error $\Delta\varphi$ of the feedback signal with respect to the incoming signal. From Equation (2.8) and Equation (2.13) it follows that

$$
\Delta\varphi = \arctan(\frac{Q}{I}) \tag{2.14}
$$
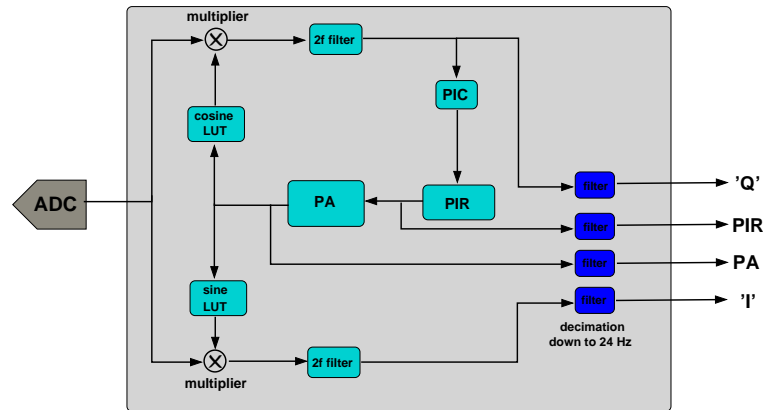
Figure 2.4: *From the PLL all desired information of the input signal can be obtained: Phase (PA), frequency (PIR) and amplitude ('I'-readout). The 'Q'-readout can be used to correct for phase errors due to finite loop gain.*

For the phasemeter protoype investigated for this thesis the data are read out with a frequency of 24 Hz downsampled and averaged from 50 MHz operating frequency of the system. The system developted according to [17] will run at 80 MHz clock frequency.

It should be emphasised that all values obtained from this PLL outputs are digital numbers that have to be converted into quantities with physical meaning. This will be explained for the PIR output in the following section.

2.2.4 Phase Reconstruction

Since the PA register content is a rapidly increasing ramp of a 84 bit register, the phase of the feedback signal is reconstructed from the PIR output. For some initial basic measurements the PA readout was evaluated, but due to more comfortable filtering possibilities the reconstruction from the PIR is the preferred method for nearly all measurements presented in this thesis. As already mentioned above the content of the PIR is a measure for the instantaneous frequency of the tracked signal. How this content (which is actually only a digital number) is scaled to a frequency value can easily be seen from Figure 2.5 showing the working principle in more detail than Figure 2.3. The full scale of the PIR is 60 bit which is 2^{60} in decimal representation (actually it is 2^{60}-1, but this makes no difference in practice). This
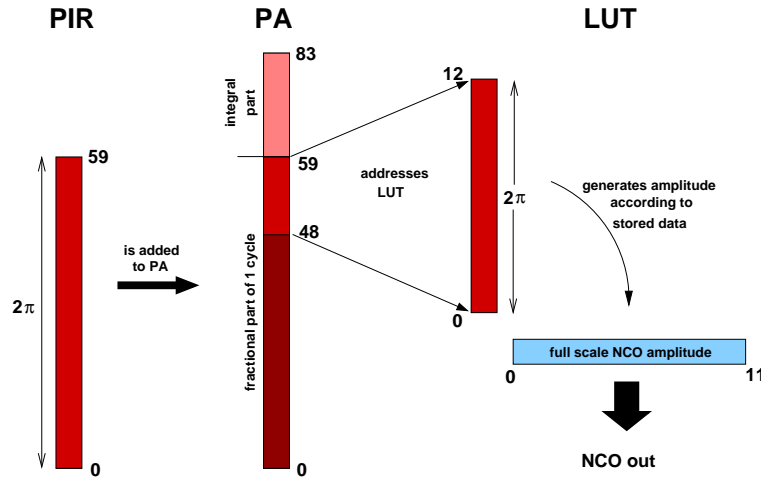
Figure 2.5: *Principle of NCO signal generation (the numbers assigned to the bars refer to bits): the fractional part from the 48th to the 59th bit of the Phase Accumulator (PA) is used to address the Look-Up-Table (LUT) to generate the feedback signal.*

value would correspond to a phase step (phase increment) of 2π during one clock cycle (corresponding to 20 ns for 50 MHz operating frequency) of the phasemeter. Hence the full range of the PIR corresponds to 50 MHz meaning that the frequency can be calculated as

$$f = \text{PIR} \cdot \frac{50\,\text{MHz}}{2^{60}} \tag{2.15}$$

where PIR is the content of the PI register converted into a digital number after EPP readout. This is the averaged frequency value over 2^{21} clock cycles (50 MHz downsampled to 24 Hz readout). So the whole phase step $\Delta\varphi$ processed by the NCO during one readout cycle (40 ms) is

$$\Delta\varphi = 2\pi \cdot f \cdot \Delta t \tag{2.16}$$

and the *phase* (the accumulated phase steps) after m readout periods is

$$\varphi(m \cdot \Delta t) = \sum_{i=1}^{m} 2\pi \cdot f_i \cdot \Delta t \qquad (2.17)$$

with

f_i : averaged frequency of i-th readout cycle

Δt : period of one readout cycle ($2^{21} \cdot 20$ ns)

$\varphi(t)$: corresponding phase

This is the desired phase information used for further investigations.

2.3 Hardware Implementation

Figure 2.6 shows a photograph of the PMS demonstration model developed and tested at the AEI. Its components are located on a 4-layer specially designed Printed Circuit Board (PCB).

Signals can be injected via 4 analog inputs that are digitised by 4 ADCs (AD 8446, 16 bit, 100 MHz maximum sampling rate) initially driven by one transformer (MC ADT1-1WT+, recommended by ADC manufacturer) each. These digitised data are further processed on an FPGA (ProAsics A3PE 3000 or 1500 with 3 or 1.5 million system gates, respectively) which contains the desired number of PLLs. These FPGA-Chips were chosen because there exist space qualified comparable versions. The system operates at 50 MHz sampling frequency (corresponds to 20 ns duty cycle time) which is generated by an onboard crystal oscillator.

The data of interest, i.e. information about phase, frequency and amplitude of the injected signals, are filtered and downsampled to about 24 Hz on the FPGA for readout via an Enhanced Parallel Port (1024 bit packets) for post-processing on a computer (LINUX operating system).

2.4 Functionality Tests

2.4.1 Tracking of unmodulated Signals

One of the very first test measurements performed with the phasemeter is depicted in Figure 2.7. The goal was to check if the system is capable to lock on an input signal, to track it and to put out a reasonable frequency value (PIR readout). For this purpose a sinusoidal 12 MHz signal was injected. From the PI register the measured frequency was read out via the EPP. The results of this measurement, i.e. the time series of the measured frequency, can be seen in Figure 2.8. Obviously the system is capable to lock on the 12 MHz signal (this process takes at most 200 ms) and to hold lock over a period of one hour. The decrease in frequency within the first 30 minutes is not caused by an imprecision of the measurement but by the warm-up process of the frequency generator. Whether the fast sub-Hertz fluctuations in the time series are noise of the phase measuring system or frequency variations that are actually present in the input signal (frequency noise of the generator) can not be distinguished by this type of measurement.
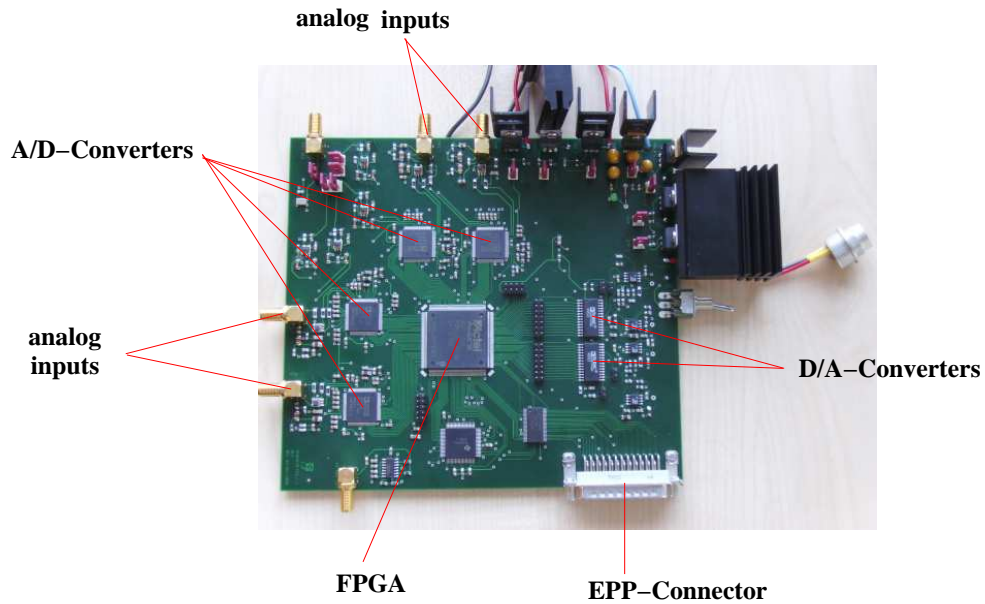
Figure 2.6: *A photograph of the 1st generation phasemeter tested and used for further development. The FPGA chip is the logical core of the phasemeter and contains the PLL code.*
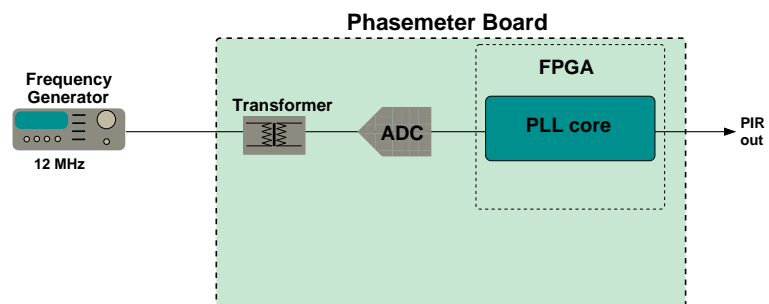
Figure 2.7: *The purpose of the first functionality test was to check if the system is able to track an injected RF signal and if there is a correct frequency output of the PIR.*
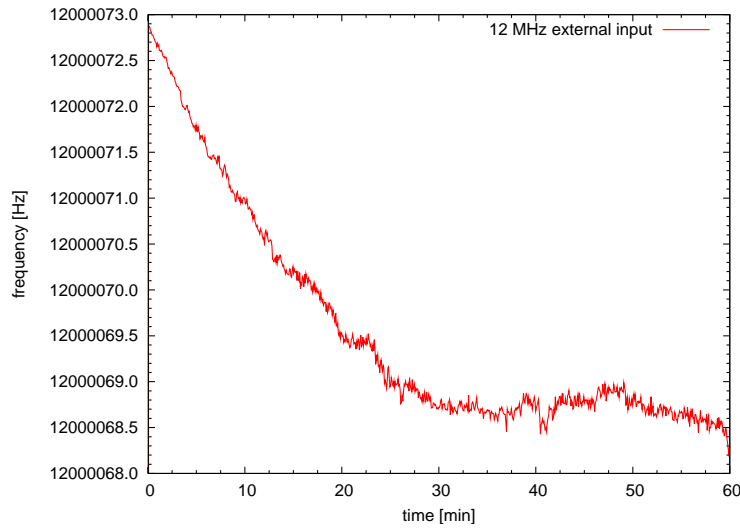
Figure 2.8: *Time series of the PIR readout for a 12 MHz input signal: the phasemeter delivers reasonable data and is able to keep lock condition over at least one hour. The frequency deviation from the exact value of 12 MHz is caused by the fact that the clock of the frequency generator is not locked on the clock of the phasemeter.*

2.4.2 Tracking of phase modulated Signals

An additional test was carried out to confirm that the phasemeter is also capable of detecting a known phase modulation applied to a MHz input signal. The setup for this measurement is depicted in Figure 2.9. The input signal (5 MHz) was phase modulated with a modulation depth of 1 radian peak-to-peak and a modulation frequency of 0.01 Hz. The information about the signal's phase was obtained by reading out the PA register. As already mentioned the PA output is a rapidly increasing ramp with slope $5 \cdot 10^6 \cdot 2\pi \,\mathrm{rad/s}$. On such a ramp the phase modulation is not visible. For this reason a 'reference ramp' was generated by means of the NCO of one PLL running also at 5 MHz. After subtraction the average ramp was
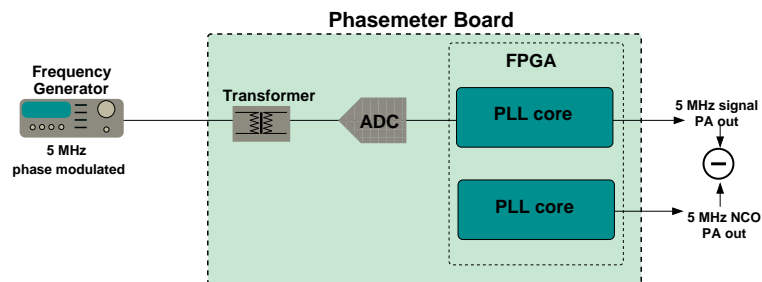
Figure 2.9: *From the PA readout one phase modulated ramp and one not phase modulated ramp with nearly identical slopes are obtained. After subtraction the average phase is flat.*

removed and the phase modulation became clearly visible as shown in Figure 2.10. From this graph it can clearly be seen that the phase modulation of the input signal
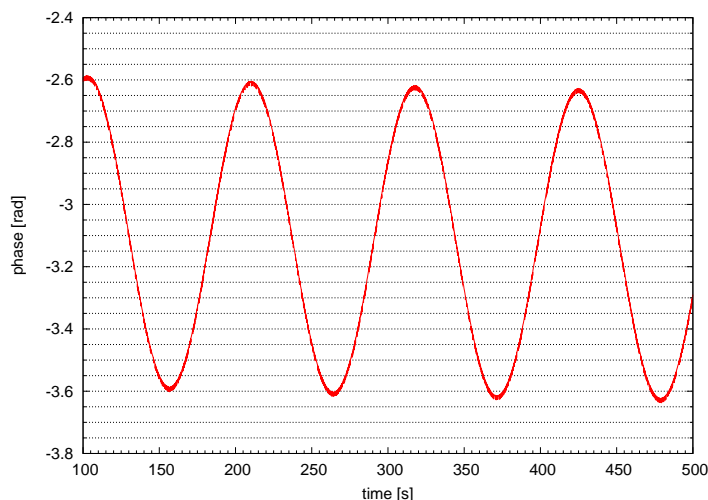
Figure 2.10: *The sinusoidal phase modulation is clearly visible in the time series of the measured phase yielding correct amplitude and modulation frequency without any distorsions.*

can be determined by means of the phasemeter with correct frequency (0.01 Hz) and amplitude (0.5 rad) and without any apparent distortions. The average phase difference shown in Figure 2.10 is slightly decreasing which means that the apparent frequency of the NCO generated signal is slightly higher than that of the frequency generator, but this phase detection principle works.

This way of determining the phase modulation of a known phase modulated input signal is used in the next section to measure the transfer function of the PLL.

2.5 Loop Analysis

In principle every PLL is inherently nonlinear making it hard to be analysed. But, as already emphasised in section 2.2.2 where the basic working principle of a PLL was explained, for a small phase error $\Delta\varphi$ there are linear techniques to analyse the loop. In particular the very powerful concept of a transfer function describing the relation between the input and the output of a linear system in Laplace domain (continuous) or z-domain (discrete) can be applied (see e.g. [13],[14]). Although the PLL described in this thesis is a digital system it will be shown that a linear analog (continuous) model is an appropriate tool to analyse this system.

2.5.1 Linear Analog Model

To analyse the PLL presented in this thesis the loop model sketched in Figure 2.11 was used. It is basically a model of a continuous system meaning that it is analysed in the Laplace domain. The simplification to a continuous model is justified since the operating frequency (50 MHz) is much higher than the frequencies of interest. It should be emphasised that this model describes the behaviour of the system with respect to *phase changes* in the input signal. This means that frequencies referred

to by the Laplace variable s are not the amplitude frequencies of the input signals (MHz range) but the frequencies of phase oscillations of these signals.

The starting point for an analysis using the concept of a transfer function is to
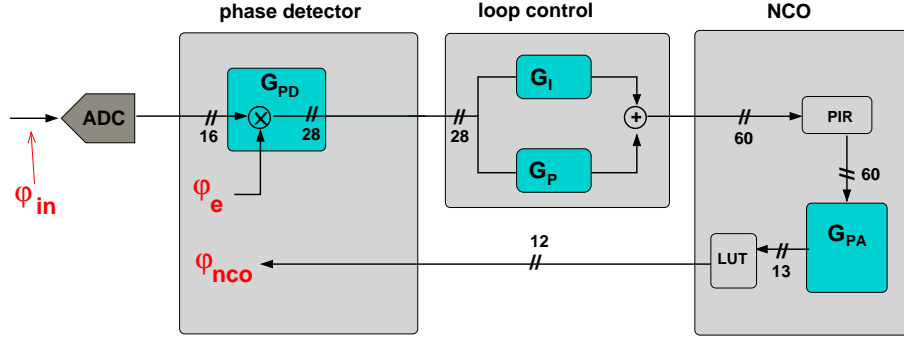
Figure 2.11: *The principle of measuring the open loop transfer function depicted here can not be used to measure it but this linear continuous model of the PLL can be used to derive the transfer functions of the system (see text). The numbers assigned to the signal lines refer to bus width in bits.*

determine the open loop transfer function (OLTF) $G(s)$ of the system being defined as

$$G(s) := \frac{\varphi_{\mathrm{nco}}(s)}{\varphi_{\mathrm{e}}(s)} \tag{2.18}$$

where the 'e' subscript stands for 'error'. Unfortunately, the principle depicted in Figure 2.11 can not be used to *measure* the open loop transfer function since the system only works in closed loop condition. The open loop gain can only be formally derived from the cascade of the loop elements (phase detector, loop control and NCO) that the error signal φ_{e} has to pass. For the system sketched in Figure 2.11 the OLTF is

$$G(s) = \frac{\kappa(T_{\mathrm{c}}s + 1)}{s^2 T^2} \tag{2.19}$$

with

$$\kappa = G_{\mathrm{PD}} \cdot G_{\mathrm{PA}} \cdot G_{\mathrm{i}} \tag{2.20}$$

$$T_{\mathrm{c}} = \frac{G_{\mathrm{p}} \cdot T}{G_{\mathrm{i}}} \tag{2.21}$$

and T being the sampling frequency.

From this expression the so-called system transfer function (STF) $H(s)$ can be derived as

$$H(s) \quad := \quad \frac{\varphi_{\mathrm{nco}}(s)}{\varphi_{\mathrm{in}}(s)} \tag{2.22}$$

$$= \quad \frac{G(s)}{1 + G(s)} \tag{2.23}$$

$$= \quad \frac{\kappa(T_{\mathrm{c}}s + 1)}{s^2 T^2 + \kappa T_{\mathrm{c}}s + \kappa} \tag{2.24}$$

Since this is a closed loop transfer function (see Figure 2.12) it can be measured as will be shown below. The denominator of this transfer function is of second degree
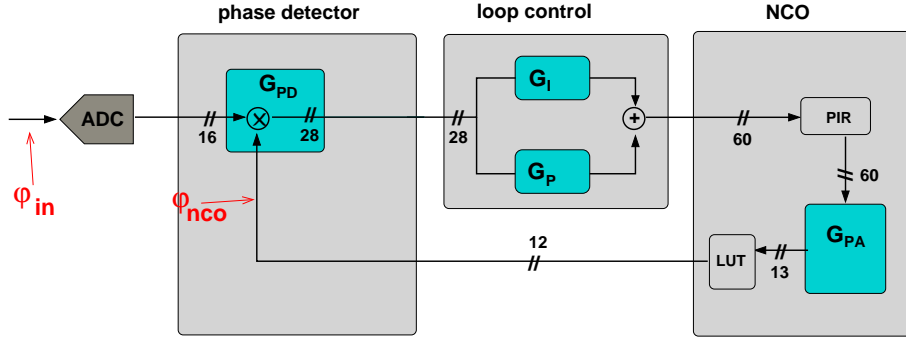
Figure 2.12: *The system transfer function is defined as $\frac{\varphi_{\mathrm{nco}}(s)}{\varphi_{\mathrm{in}}(s)}$ and can be measured with the setup sketched in Figure 2.9.*

in s. For this reason the PLL here is said to be a *second order* PLL. Since the PLL contains *two* integrators in total (phase accumulator and integral gain register of the controller) it is denoted as a *type 2* PLL (of second order). These type of PLL is widely used since it does not introduce steady state phase errors if a phase or a frequency step occurs in the RF input signal (assuming the system to remain locked on the signal).

2.5.2 Transfer Function Measurement

To confirm that the model derived in the previous section is an appropriate description of the loop, its predictions have to be compared to measured data. The setup that was chosen to perform the corresponding measurement is the same as already depicted in Figure 2.9. A phase modulated signal generated by means of the frequency generator (Rohde & Schwarz SML-03) was injected in one phasemeter channel. The signal frequency was constant at 12 MHz with input amplitude of $2\,\mathrm{V_{pp}}$. The depth (amplitude) of the phase modulation was kept fixed at 0.6 radian peak-to-peak. Nine different measurements where performed with phase modulation frequencies between 100 Hz and 2 kHz. The amplitude of the feedback phase was determined by applying the readout scheme shown in Figure 2.9 and Figure 2.10 to calculate the ratio of feedback and input phase (see Equation (2.22)). These experimental derived ratios were compared with the theoretical values for $H(s)$ ($G_i = 2^{20}, G_p = 2^6$). The results of this measurement can be seen in Figure 2.13. It shows the Bode plot of the system transfer function $H(f)$. It can clearly be seen that the measured data match quite well the theory. $H(f)$ behaves in principle like a low pass filter. The gain peak has a maximum at about 400 Hz Fourier frequency. Gain peaking *always* appears in the system transfer function of second order type 2 PLLs (see e.g. [37] for details). Furthermore it can be seen that the relation between feedback and input phase approaches a one-to-one relation the lower the Fourier frequency is. This is the reason why phase oscillations of the input signal in the mHz regime can be directly determined by the feedback signal.

These results show that the linear continuous model is an appropriate tool to describe the control loop.
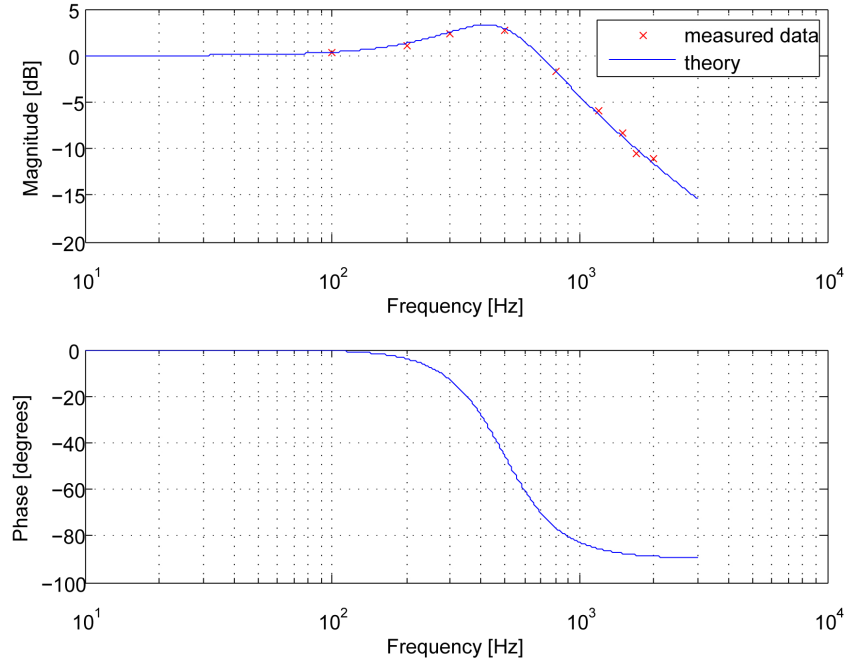
Figure 2.13: *The Bode plot for the measured and the calculated STF clearly shows the compliance of theory and measurement (top). For completeness the theoretical phase behaviour is also plotted (bottom).*

2.5.3 Loop Gain Adjustment

In the previous section the PLL was characterised by the gains of the loop elements and the sampling frequency. A second order type 2 PLL can also be completely described by two different loop parameters: the undamped natural frequency ω_n and the dimensionless damping factor ζ. With these parameters the system transfer function can be described by

$$H(s) = \frac{2\zeta\omega_\mathrm{n}s + \omega_\mathrm{n}^2}{s^2 + 2\zeta\omega_\mathrm{n}s + \omega_\mathrm{n}^2} \tag{2.25}$$

with

$$\omega_\mathrm{n} = \frac{\sqrt{G_\mathrm{PD} \cdot G_\mathrm{PA} \cdot G_\mathrm{i}}}{T} \tag{2.26}$$

and

$$\zeta = \frac{1}{2}G_\mathrm{p} \cdot \sqrt{\frac{G_\mathrm{PD} \cdot G_\mathrm{PA}}{G_\mathrm{i}}}. \tag{2.27}$$

A preferred value of the damping constant ζ is 0.707 (critical damping). From Equation (2.27) it follows that G_i and G_p can be adjusted like

$$G_\mathrm{i} = \frac{G_\mathrm{PD} \cdot G_\mathrm{PA}}{(2\zeta)^2} \cdot G_\mathrm{p}^2 \tag{2.28}$$

to get a desired value of 0.707 for ζ. In Figure 2.14 the theoretical curve for G_i and G_p to get the system critically damped is plotted. The assumed input amplitude

was $3.2\,\mathrm{V_{pp}}$ (ADC full range). This graph served as a guideline for the choice of gain combinations.
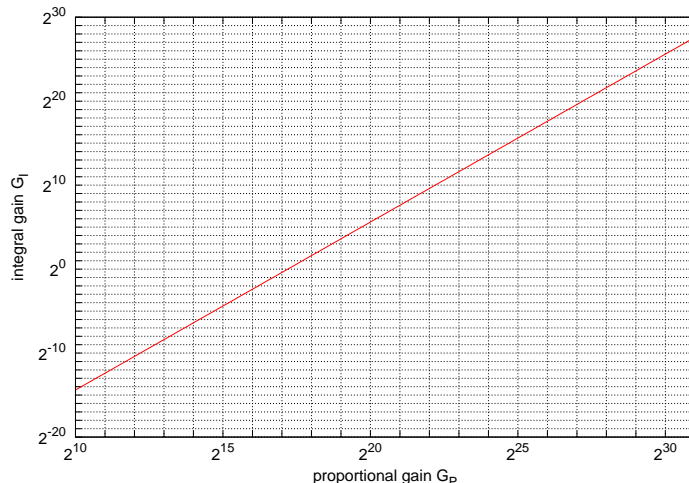
Figure 2.14: *PIC combinations to achieve critical damping according to Equation (2.28)*
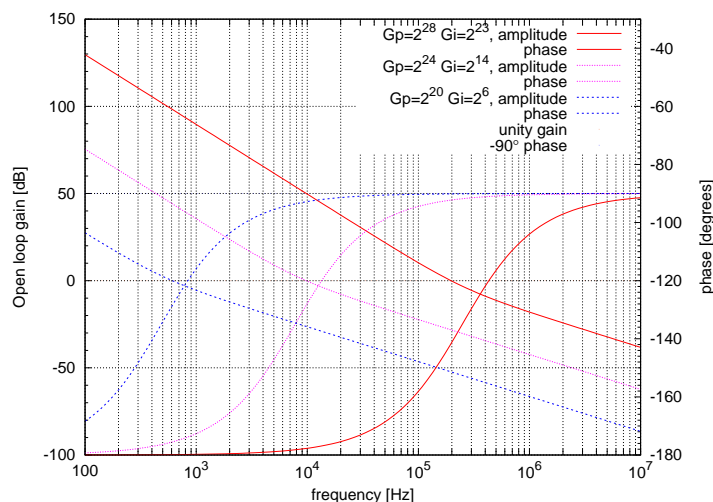
Figure 2.15: *The open loop transfer function indicates that $G_i = 2^{23}$ and $G_p = 2^{28}$ are gain combinations with acceptable unity gain frequency and sufficient phase margin.*

Figure 2.15 shows the Bode plot of the open loop transfer function for three different gain combinations for the system to be approximately critically damped. For the system to have a proper one-to-one relation between input and feedback phase without the necessity of performing an I/Q correction the unity gain frequency should be sufficiently high. Furthermore a high unity gain will be needed for digital locking of lasers which requires a bandwidth of approximately 30 kHz. The gain combination $G_i = 2^{23}$ and $G_p = 2^{28}$ seemed to be an appropriate choice. The unity gain frequency is 200 kHz and the phase margin is 40°.

To test if this gain combination is really a good choice the measurement depicted in Figure 2.16 was carried out. An NCO onboard the FPGA was used to generate a 12 MHz signal which was input for a PLL. The tracked phase was read out from the PA register. Several measurements were performed using different gain combinations. The results of the obtained spectral densities of the phase for these one-channel measurements are shown in Figure 2.17. (The requirement for the phasemeter is set to $2\pi\,\mu\mathrm{rad}/\sqrt{\mathrm{Hz}}$. This will be derived in the beginning of the next chapter.) From the left graph of Figure 2.17 it can be seen that the noise floor of the measurement using a pro-

Figure 2.16: *Setup for investigating the noise dependence of one PLL channel on the gain combinations*

portional gain of 2^{30} is above those for proportional gains of 2^{29} and 2^{28}. The noise
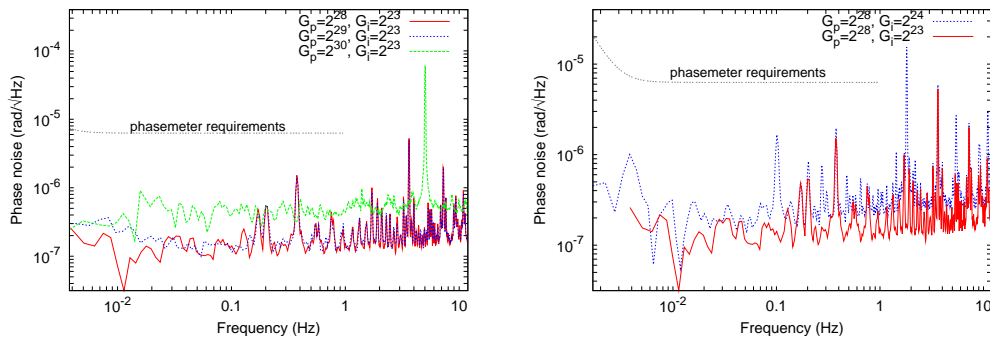
Figure 2.17: *Results of the measurement depicted in Figure 2.16: To choose a proportional gain of 2^{28} or 2^{29} and an integral gain of 2^{23} seemed to be most promising. No other gain combination showed better noise behaviour with respect to this measurement*

of the measurement using $G_{\mathrm{p}} = 2^{30}$ did not change significantly when changing the integral gain G_{i} (not sketched). Increasing G_{i} for $G_{\mathrm{p}} = 2^{28}$ (left graph of Figure 2.17) led to an increase of the noise floor. All noise curves show a large number of peaks but for $G_{\mathrm{p}} = 2^{28}(2^{29})$ these peaks are below the requirements.

The measurements done here indicate that a good choice for the gains of the loop control were $G_{\mathrm{p}} = 2^{28}(2^{29})$ and $G_{\mathrm{i}} = 2^{23}$. During the further work on the phasemeter it came out that this gain combinations delivered best results.

3 Phasemeter Sensitivity Investigations

In this chapter the way from the first already quite promising phase noise performance results towards a satisfying phasemeter sensitivity with respect to unmodulated sinusoidal input signals will be presented.

In the first two sections (3.1 and 3.2) the requirements on the phase noise of the phasemeter are briefly discussed and termini like 'sensitivity' and 'performance' (which will be used synonymously) are defined. In the sections that follow (3.3 and 3.4) the most serious noise sources with respect to the experiments described in this chapter are identified. It will be described how they could be eliminated to a sufficient degree. The focus lies on the so-called ADC time jitter noise and on the noise introduced by different analog front end designs. In section 3.5 the results are summarised and it will be shown that the phasemeter sensitivity defined in section 3.2 meets the desired requirements. This opens the door for a more sophisticated and detailed analysis of the phasemeter performance (chapter 4) and for the first applications more directly related to the LISA project (section 4.3).

3.1 Phasemeter Requirements

The requirements on the full LISA/NGO instrument is basically derived from the scientific objectives, the transfer function of the interferometer and a 35 % margin on strain sensitivity ([15],[16],[19]).

The scientific objectives to obtain information from astrophysical sources in the frequency band from $1 \cdot 10^{-4}$ Hz to 1 Hz (goal: $3 \cdot 10^{-5}$ Hz to 1 Hz) with a SNR of $5\,\sigma$ over 1 year integration time defines the requirement on strain sensitivity of the full detector ([21],[20]). A 35 % system margin is applied to this strain sensitivity for the instrumental requirements being below the scientific ones ([19]). Furthermore the transfer function of the interferometer, i.e., the frequency dependent response to a gravitational wave passing the detector, has to be taken into account ([22],[1]). This chain results in a simplified ([19]) requirement for the optical pathlength noise for a single link (transmit/receive) of

$$\tilde{s}_{sl} = 12\,\frac{\mathrm{pm}}{\sqrt{\mathrm{Hz}}} \cdot \sqrt{1 + \left(\frac{2.8\,\mathrm{mHz}}{f}\right)^4} \tag{3.1}$$

One fundamental noise contribution is the shot noise due to the weak light received from the remote satellite. It gives a frequency independent contribution of about $8\,\mathrm{pm}/\sqrt{\mathrm{Hz}}$ assuming 100 pW of received light after the beam has passed the components of the optical chain prior to the photo detector ([19],[16]). This noise contribution is already included in the $12\,\mathrm{pm}/\sqrt{\mathrm{Hz}}$ requirement stated in Equation (3.1). The situation differs for NGO since the armlengths are shorter by a factor of 5 and the received power is 270 pW corresponding to about $5\,\mathrm{pm}/\sqrt{\mathrm{Hz}}$ shot noise contribution

([15]). For the phase readout not to give a significant contribution compared to the shot noise expected for LISA the phasemeter sensitivity requirement (excluding optics and residual clock noise) is allocated at $1\,\mathrm{pm}/\sqrt{\mathrm{Hz}}$ with the frequency dependent shape given by Equation (3.1) ([16]). This corresponds to $2\pi\,\mu\mathrm{rad}/\sqrt{\mathrm{Hz}}$ for a laser wavelength of $1\,\mu\mathrm{m}$ (this is the wavelength of the Nd:YAG NPRO laser baselined for LISA). A graphical presentation of the requirements are shown in Figure 3.1. In the remainder of this thesis the differential phase noise between two phasemeter channels will be used to characterise the phasemeter's sensitivity and will be compared with the $2\pi\,\mu\mathrm{rad}/\sqrt{\mathrm{Hz}}$ requirement. This is one topic of the subsequent section.
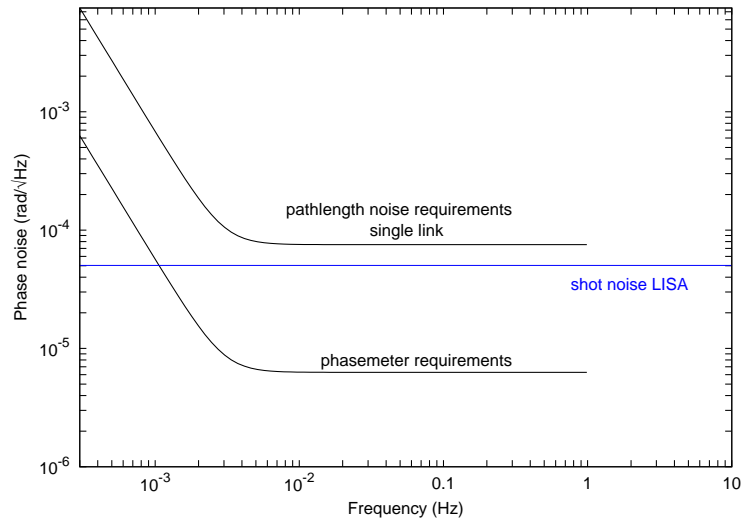
Figure 3.1: *Requirements for a single phasemeter channel and for a single interferometer link*

3.2 Initial Sensitivity Measurements

3.2.1 Principle of Zero Measurement

For determining the phase noise of the phasemeter a zero measurement is an appropriate tool. The basic principle of such a measurement is sketched in Figure 3.2. The output signal of a frequency generator is split before being injected into two phasemeter channels. For each single channel the phase is reconstructed from the PIR output and for each readout cycle these phases are subtracted in post-processing on a computer indicated by 'phase difference' in Figure 3.2. The basic functioning principle of such a measurement is that noise introduced to the signal by one arbitrary component before splitting cancels by subtraction, since it is the very same in both readout channels. In the case of the measurement shown in Figure 3.2 the noise of the generator cancels and the phase noise of the transformers, of the ADCs and of the PLLs remain. Depending on which noise contribution is to be investigated this basic setup (Figure 3.2) can be modified as will be explained in the subsequent sections.
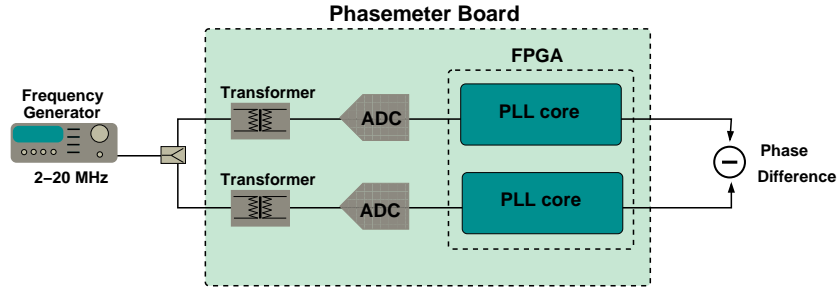
Figure 3.2: *Setup zero measurements: the noise of the frequency generator cancels by subtraction. The phase difference is reconstructed from the PIR content.*

If the PMS would be noise-free the difference between the two channels would be flat at zero or at most at a constant value, due to initial offsets during the lock-in process. The deviation of the phase difference from zero between these two channels is used to *define* the sensitivity of the PMS with respect to a certain setup.

The practical approach of measuring this sensitivity by this method is explained in section 3.2.2. It should be emphasized that such a zero-measurement can not be
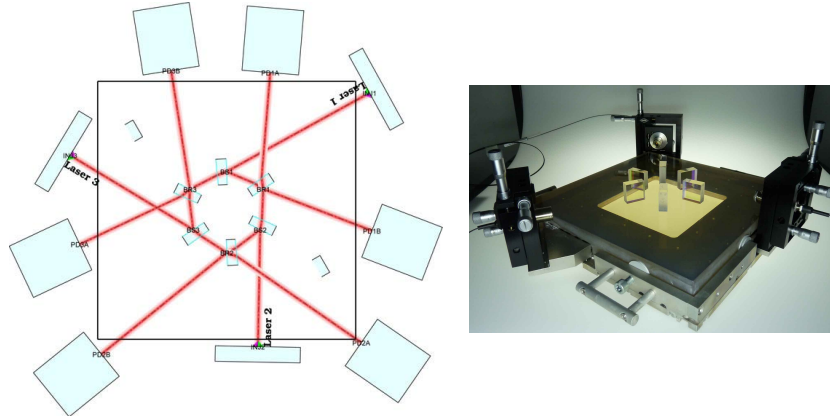
Figure 3.3: *The hexagon interferometer is designed such that the beat-notes obtained by interference of the 3 laser beams can be used to test the linearity of the phasemeter. The photograph shows the prototype designed and built at AEI.*

used to test the linearity of the system since the two phasemeter channels basically have to track identical signals. In further investigations it has to be shown that the system works linear in the sense that:

$$OUT[\sin(\omega_1 t + \varphi_1(t)] + OUT[\sin(\omega_2 t + \varphi_2(t)] = OUT[\sin((\omega_1 + \omega_2)t + \varphi_1(t) + \varphi_2(t)] \tag{3.2}$$

where "OUT" assigns the phasemeter output that yields the phase information. To test this linearity the system will have to track signals with frequencies ω_1, ω_2 and ω_3 and phases $\varphi_1(t)$, $\varphi_2(t)$ and $\varphi_3(t)$, respectively. These signals must be constructed such that

$$(\omega_1 t + \varphi_1(t)) + (\omega_2 t + \varphi_2(t)) - (\omega_3 t + \varphi_3(t)) = 0. \tag{3.3}$$

This can be achieved by creating them as differences $(a-b), (b-c)$ and $(a-c)$ from independent sources a, b, c. If the system works linearly only the noise of 3 phasemeter channels remains after adding the signals to verify Equation (3.3). This test can be implemented in the digital domain, with analog signals (including analog components and ADCs) and finally in an optical system which includes photo diodes etc.. The optical test was implemented by means of the hexagon interferometer depicted in Figure 3.3. The beat-notes obtained by interference of the 3 laser beams deliver signals that fulfil the condition stated in Equation (3.3). Such a hexagon interferometer has been designed and implemented at the AEI. Investigation on this system are succesfully ongoing but are not topic of this thesis.

3.2.2 First Sensitivity Results

One of the first measurements to characterise the sensitivity of the phasemeter with respect to the setup depicted in Figure 3.2 was carried out using a 12 MHz input signal. The time series of the frequency difference obtained from the two phasemeter PIRs and the reconstructed phase difference are shown in Figure 3.4. The frequency difference fluctuates around zero with a peak amplitude of about 20 μHz (blue curve, left). The corresponding phase difference (red curve, right) shows fluctuations in the order of hundreds of microradians.

The linear power spectral density of this time series is the desired measure for the phasemeter sensitivity. The result for the time series of the phase difference in Figure 3.4 (right graph) is shown in Figure 3.5.
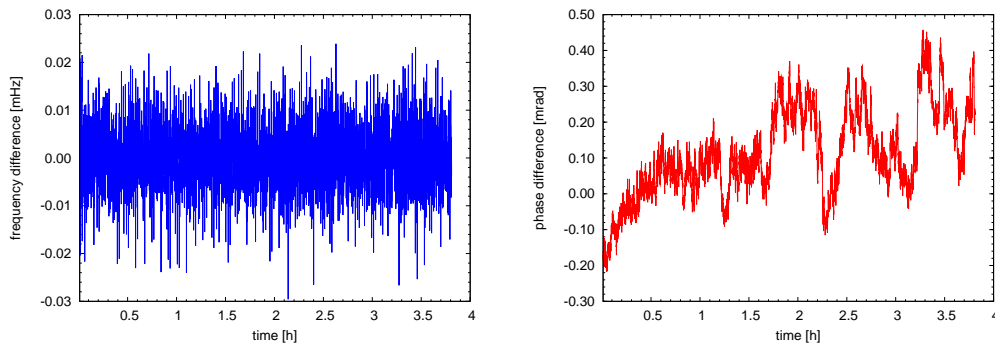
Figure 3.4: *Time series of differential frequency measurement (left) and the corresponding reconstructed phase difference (right) for a 12 MHz zero measurement using two transformers*

For Fourier frequencies between 0.3 mHz and 400 mHz the noise curve is above the requirements. It increases to lower frequencies with approximately $1/f$. Furthermore there appear peaks in the differential phase noise which seem to be harmonics of 0.86 Hz.

Figure 3.6 shows the results for measurements performed with different input frequencies between 2 and 20 MHz. The noise is above the requirements for Fourier frequencies below 400 mHz for each chosen input signal frequency. A clear dependence between input frequency and phase noise is not observable although there are differences in phase noise of up to one order of magnitude (e.g. at 10 mHz). In particular for lower input frequencies (2, 4 and 6 MHz) the noise shows a shoulder-
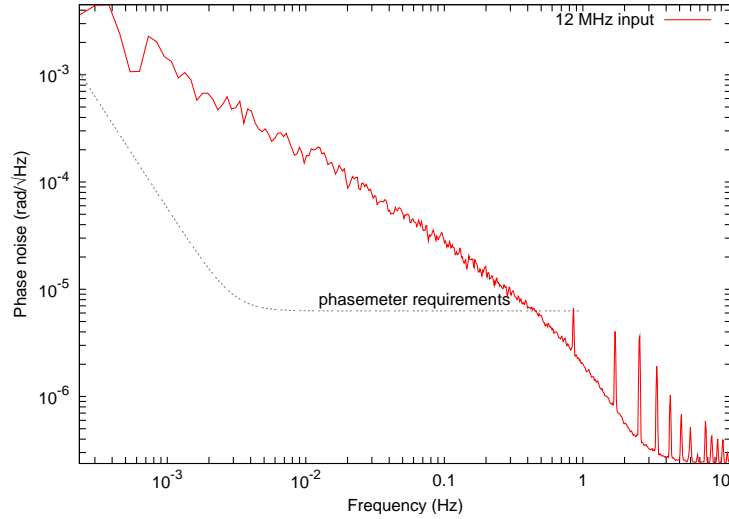
Figure 3.5: *Spectral density of differential phase measurement for a 12 MHz input signal derived from the time series shown in Figure 3.4; the noise is above the requirements for nearly the whole frequency range of interest. The peaks appearing above 1 Hz Fourier frequency are most probably explainable by differential PLL noise (cf. Figure 2.17).*
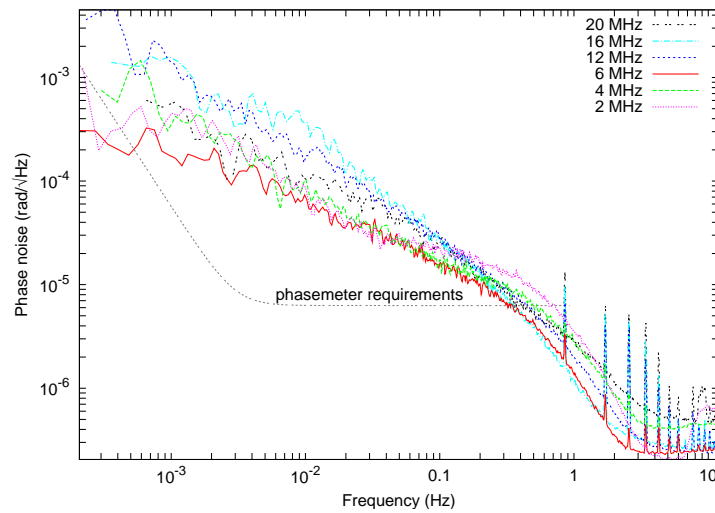
Figure 3.6: *First sensitivity measurements using input frequencies between 2 and 20 MHz show unsatisfying noise performance.*

like spectrum. The peaks already visible for the 12 MHz measurement in Figure 3.5 appear at the very same Fourier frequencies independent of the input frequency. One possible explanation for this peaks might be the behaviour of the PLLs. In section 2.5.3 it was shown that a single PLL tracking a digital NCO output shows comparable peaks (Figure 2.17) to those in Figure 3.6. If two PLLs do not get the very same signal the peaks might not cancel in subtraction as it is the case for two PLLs tracking the very same signal from one ADC (this will be shown below).

This performance is of course unsatisfying and further investigations had to be done to improve it.

3.2.3 Influence of Loop Gains

One could be tempted to assume that a bad choice of the gains (or of the gain combinations) of the PLLs is the origin of this phase noise. Figure 3.7 shows the results for a 12 MHz measurement using different gain combinations. Obviously this has no influence on the sensitivity. The phase noise remains the same apart from usual statistical fluctuations of the noise curves. Also the peaks remain at the same frequencies with the same peak heights.
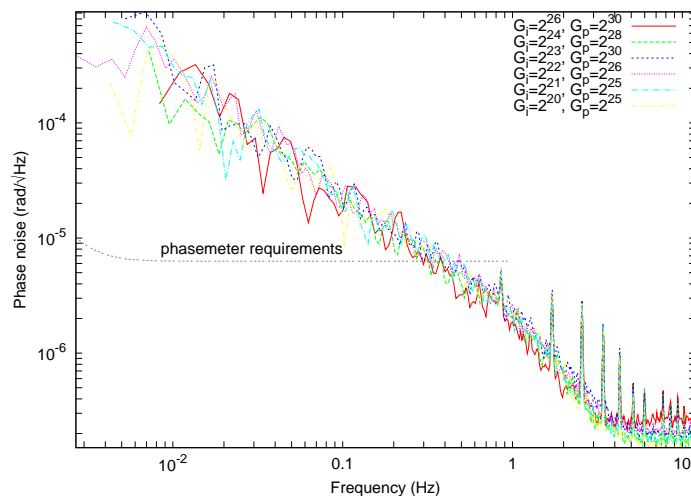
Figure 3.7: *Phase noise for a 12 MHz input signal using different PLL gain combinations; the choice of gains is not the source of the poor performance*

3.2.4 Input Amplitude Digitisation Noise

Another possible reason for the poor noise behaviour could be the amplitude of the input signal. To investigate this, measurements with different amplitudes of a 12 MHz input signal were performed using the setup depicted in Figure 3.2. The results can be seen in the left graph of Figure 3.8. Although no improvement was possible an amplitude dependence of the phase noise can clearly be seen. By decreasing the amplitude of the input signal below $1\,V_{pp}$ there is an increase in the

flat noise floor limiting the performance at the high frequency end (above the LISA band). Since this noise floor is white and increases with decreasing input amplitude it is most probably caused by the digitising process of the input signal. This type of noise is usually proportional to the inverse of the amplitude ($\tilde{n}_{dig} \propto 1/\text{amplitude}$). The right graph of Figure 3.8 shows that for this experiment this relation is obviously valid for input amplitudes up to $1\,\text{V}_{pp}$. A further increase in input amplitude does not enhance the performance so there must be some additional limiting factor. The assumption is that this is the limit set by the digital output of the NCO which is mixed in the PLLs with the digitised input signal. This amplitude output is by design fixed in amplitude and LSB width. Probably this NCO output dominates the digitising noise of the phasemeter for input amplitudes higher than $1\,\text{V}_{pp}$. Since this noise is well below the requirements for sufficient high input amplitudes it should not be a limiting noise source in further considerations. The problem is still the $1/f$ noise behaviour that obviously has a different origin than the white digitisation noise.
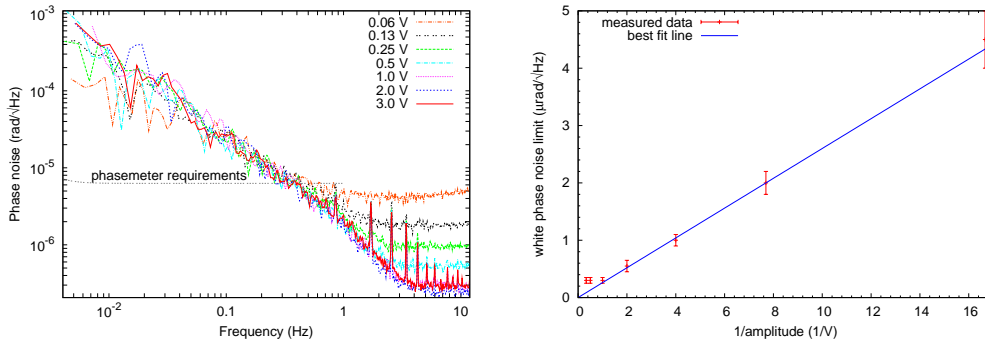
Figure 3.8: *Phase noise dependence on the input signal amplitude clearly shows the expected reciprocal relation.*

3.2.5 Modified Zero Measurements

As already mentioned in the beginning of this section the setup sketched in Figure 3.2 can easily be modified to exclude potential noise sources and add them back in step by step to the measurement chain. Since the origin for the poor noise performance shown e.g. in Figure 3.6 was still unknown the setups depicted in Figure 3.9 were used to find out which components are the main noise sources. The upper sketch in Figure 3.9 shows the setup for investigating the noise of the PLLs since noise introduced by the transformers or the ADCs cancels in subtraction. The result of this measurement was that the differential signal of two PLLs receiving the very same signal from one ADC is flat at zero. In this sense the PLLs are noise free. This does not mean that each single PLL is noise free but that the noise that might be introduced is perfectly common mode. But even twice the noise measured for a single PLL-NCO combination (cf. section 2.5.3) would not explain the excess phase noise presented in the previous sections.

The next step was to implement two ADCs into the measurement chain as is depicted in the lower sketch of Figure 3.9. This includes the ADCs as noise source, but not

the transformers since the transformer noise is common mode in both channels. Again a differential phase measurement was performed using a 12 MHz input signal. The results of this measurement can be seen in Figure 3.10 compared to the results
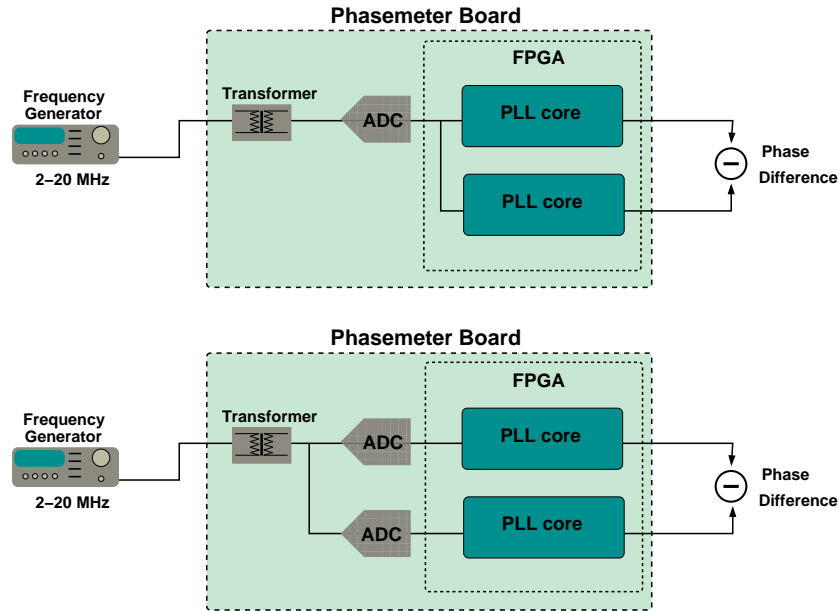
Figure 3.9: *Different setups for investigating the noise contributions of the PLLs (top) and the contributions of the PLLs plus ADCs (bottom)*

obtained by using the setup sketched in Figure 3.2. From this graphical presentation 3 important informations can be extracted:

- The phase noise of the measurement using two transformers is obviously dominated by the noise introduced right by these devices below 1 Hz.

- The performance using only one transformer is limited for frequencies below 3 Hz by ADC noise since noise of the transformer cancels by subtraction and the PLLs are at most responsible for the peaks above 0.8 Hz Fourier frequency.

- Though improved significantly when using only one transformer the sensitivity is dominated by some ADC noise that still shows an unacceptable $1/f$ shape that does not meet the requirements.

In the subsequent section the origin of this noise source will be further investigated.

3.3 ADC Time Jitter Noise

In this section the ADC noise will be identified to be caused by a timing jitter in the ADC sampling process, a known problem inherent to ADCs. Furthermore a correction scheme using a calibration (or pilot) tone to correct for this type of noise will be presented. It will also be demonstrated that this correction scheme suppresses this noise to a level below the requirements.
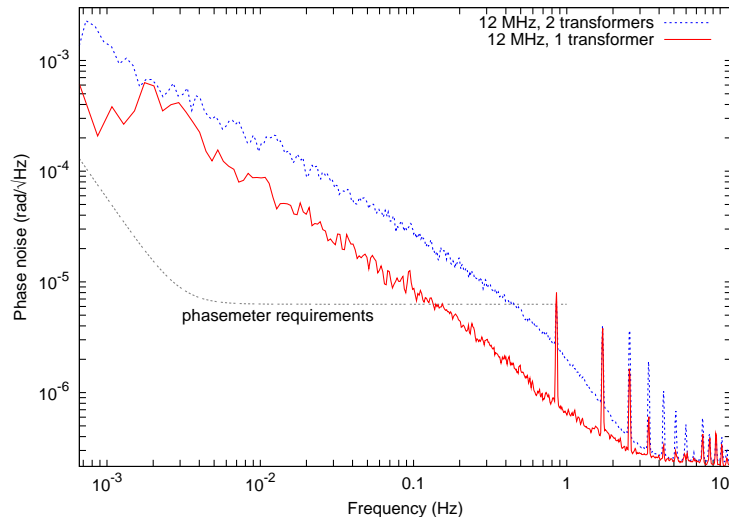
Figure 3.10: *Phase noise obtained from a measurement with only one transformer and two ADCs still shows $1/f$ shape and does not meet the requirements.*

3.3.1 Phase Noise due to Sampling Jitter

The origin of the $1/f$ phase noise introduced by the ADCs is timing jitter in the sampling process of the ADCs (this will be confirmed below). In Figure 3.11 the sampling points on an incoming sinusoidal wave (red) of a perfectly sampling ADC are represented by the vertical lines. They are equidistant in time with sampling period T_s.

A real ADC does not sample that perfectly. The sampling points jitter in time
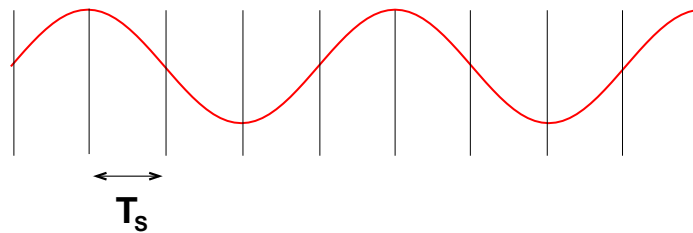
Figure 3.11: *Sampling points for a perfectly sampling ADC are equidistant in time with sampling period T_s.*

as shown in Figure 3.12. The periods between these sampling points jitter around the average period T_s. This has a significant impact on the phase measurement. In principle the phasemeter measures the phase steps between two adjacent sampling points and these phase steps vary in time due to the jitter (actually we measure the average over 2^{21} of those steps from the PIR (cf. section 2.2.4), but the effect does not cancel out by averaging and for a basic consideration it does not make any difference).

In Figure 3.13 it can be seen how a time deviation δt with respect to a perfectly

47
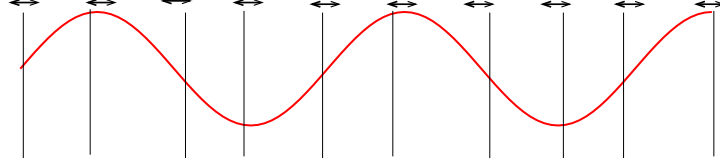
Figure 3.12: *For a real ADC the sampling points jitter in time.*

sampling ADC influences the detected phase even though the sampled signal is at constant frequency. It can easily be seen that this time shift δt corresponds to a difference in phase of

$$\delta\varphi = 2\pi f_{\text{in}} \cdot \delta t \tag{3.4}$$

where f_{in} is the (constant) frequency of the input signal. This means that a time
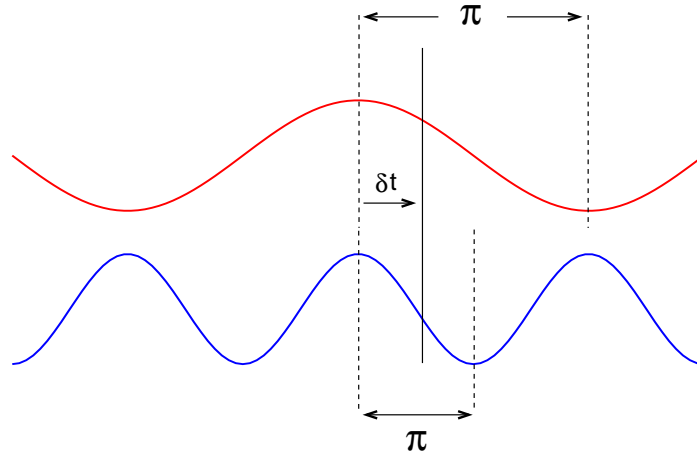
Figure 3.13: *A time deviation of δt between sampling points leads to an input frequency dependent deviation in the measured phase step although the signal frequencies are constant.*

jitter having a linear spectral density of $\tilde{t}_{1,\text{jit}}$ and $\tilde{t}_{2,\text{jit}}$ for channel 1 and channel 2, respectively, leads to a *differential* phase noise of

$$
\begin{aligned}
\tilde{\varphi}_{\text{jit}} &= 2\pi f_{\text{in}} \cdot \sqrt{\left(\tilde{t}_{1,\text{jit}}\right)^2 + \left(\tilde{t}_{2,\text{jit}}\right)^2} \\
&= 2\pi f_{\text{in}} \cdot \tilde{t}_{\text{jit}}
\end{aligned}
\tag{3.5}
$$

since $\tilde{t}_{1,\text{jit}}$ and $\tilde{t}_{2,\text{jit}}$ are not correlated and add quadratically. It should be emphasised that this time jitter is **not** caused by the jitter between the clocks driving the ADCs (this would lead of course to an additional time jitter noise contribution). It is a feature inherent to the ADCs that also appears in difference if two ADCs are driven by the very same clock.

3.3.2 ADC Jitter Measurements

To confirm that it is the time jitter explained above causing the ADC noise shown in Figure 3.10 some additional measurements had to be performed. From Equation (3.5) it can be seen that comparable ADC time jitter behaviour should lead to an *input frequency dependent* differential phase noise. To check this, additional phase noise measurements using the setup depicted in Figure 3.14 were performed for different input signals (2, 6 and 12 MHz). The differential phase noise obtained by this measurements can be seen in Figure 3.15.
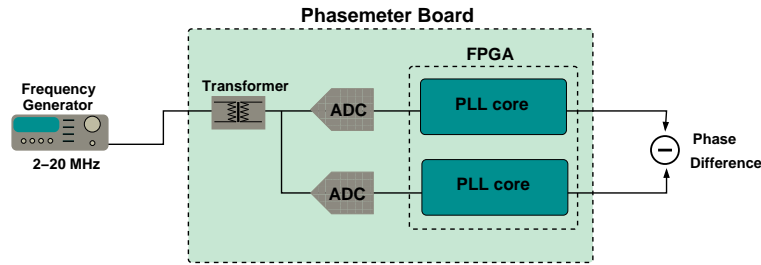
Figure 3.14: *Setup for measuring the differential phase noise introduced by the ADCs for different input frequencies*
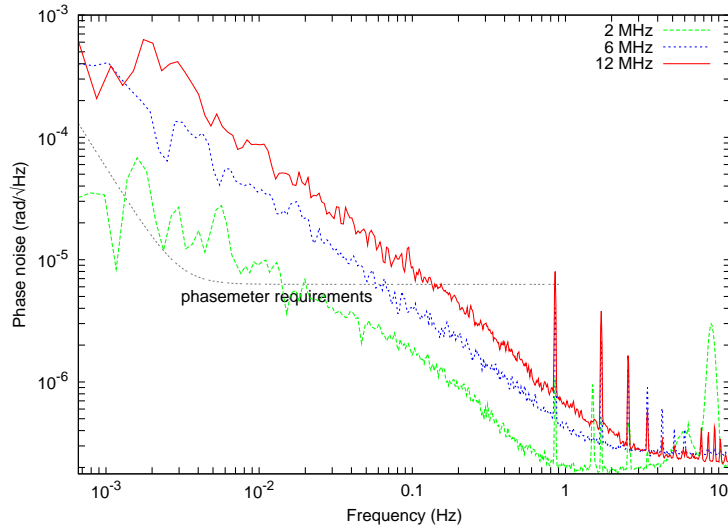
Figure 3.15: *Measured differential phase noise for different input frequencies clearly depends on the input frequency.*

One can clearly see the input frequency dependence of the phase noise. The phase noise increases for higher input frequencies. In the next step the values of the spectral densities of the phase difference shown in Figure 3.15 were converted into equivalent time jitter noise according to

$$\tilde{t}_{\mathrm{jit}} = \frac{\tilde{\varphi}_{\mathrm{jit}}}{2\pi f_{\mathrm{in}}} \tag{3.6}$$

This convertion of course only makes sense if the time jitter is the dominating noise source. The results of this conversion can be seen in Figure 3.16. It shows that below 500 mHz Fourier frequency all three signals seem to experience at least a comparable time jitter. The frequency region above 500 mHz is limited by digitising noise which does not have the same frequency dependence as stated in Equation (3.6), so the conversion can not yield useful information. Also below 500 mHz the three curves do not lie exactly on top of each other. The reasons for this are that the jitter is a statistical process that varies from measurement to measurement and that it is also influenced by changes in environmental conditions (in particular temperature). To exclude all these uncertainties the setup depicted in Figure 3.17 was chosen to
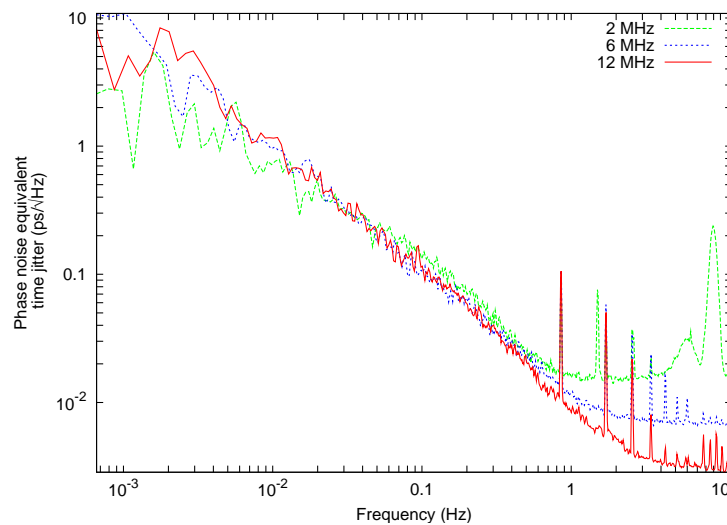
Figure 3.16: *Phase noise equivalent time jitter below 500 mHz is roughly identical for 2, 6, and 12 MHz input signals.*

perform two zero measurements *simultaneously*. A 20 MHz and a 2 MHz signal were added in front of the transformer. Afterwards the signals are both sampled by the same ADCs to experience the very same time jitter. They are tracked by different PLLs by choosing 2 and 20 MHz as initial offset value, respectively. (Actually this was the first test showing that the phasemeter is able to track two different frequencies being present in one and the same input channel.)

The results after converting the measured phase noise into equivalent time jitter noise can be seen in Figure 3.18. It can clearly be seen that for Fourier frequencies below 300 mHz the curves seem to lie exactly on top of each other. Since it is known that ADCs show this time jittering behaviour and since the measurements clearly match the assumed theory it can be regarded as proven that the dominant noise in the measurements performed with one transformer and two ADCs is the ADC time jitter.

The setup depicted in Figure 3.17 and the fact that two signal of different frequencies passing simultaneously the same ADC experience the same time jitter can be used to correct for this noise source. How this is done is described in the next section.
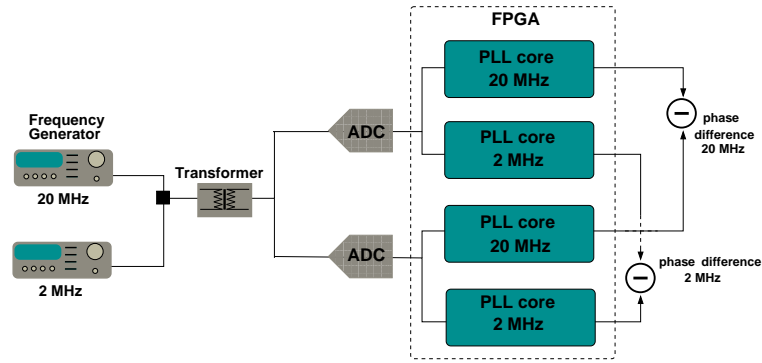
Figure 3.17: *Setup for simultaneously performing two zero measurements for investigating the relation between phase noise and time jitter*
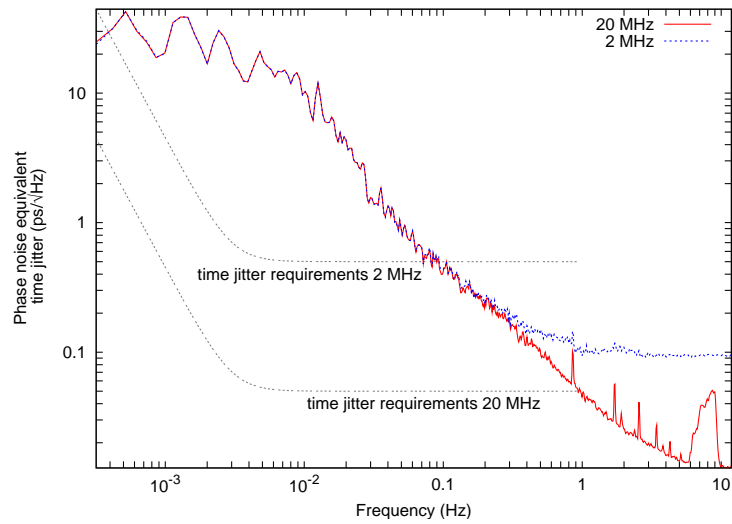
Figure 3.18: *Phase noise equivalent time jitter is identical for 2 and 20 MHz input signals below 300 mHz.*

3.3.3 ADC Time Jitter Correction Principle

The time jitter correction principle is based on three assumptions:

- Two signals of different frequency that are electrically added and simultaneously sampled by one and the same ADC experience the very same time jitter.

- The relation between this time jitter and the corresponding phase noise scales linearly with the signal frequency.

- The time jitter of the ADCs is the dominating noise source.

The first two points have been explained and confirmed in the previous sections. The third one is obviously true for Fourier frequencies below 300 mHz (see Figure 3.18), but this will become an issue in section 3.4.

One of these two signals is assumed to be the one of scientific interest (e.g., carrying information about a gravitational wave). The other one (usually set to a higher frequency to get highest possible correction accuracy) is the so-called *pilot* or *calibration tone*.

Two correction schemes will be presented below which differ in the time reference of the correction scheme.

The first scheme assumes a phase stable pilot tone as reference. 'Stable' means that the inherent phase noise equivalent time jitter of this tone is below the requirements to be fulfilled. If this pilot tone is coherently derived from a USO, this USO can be regarded as reference. This scheme is the choice for the implementation in LISA.

The second possible scheme is a relative jitter correction between two ADC input channels. In this case the time reference is the time period between two sampling points of one of the ADCs. (Actually it is the average during one readout cycle but this fact doesn't change the principle explained here.) This correction scheme has been used here to characterise the phasemeter performance including jitter correction.

3.3.3.1 Pilot Tone Reference

This correction scheme can be applied using only one ADC as depicted in Figure 3.19. If the pilot tone is sufficiently stable then for each readout cycle of the pilot tone the deviation in phase $\delta\varphi_{\text{pilot}}$ from the nominal phase increment length $\Delta\varphi_{\text{pilot,nom}}$ caused by a time deviation δt (the jitter) can be measured as

$$\delta\varphi_{\text{pilot}} = \Delta\varphi_{\text{pilot,det}} - \Delta\varphi_{\text{pilot,nom}} \tag{3.7}$$

where $\Delta\varphi_{\text{pilot,det}}$ is the detected phase step during one readout cycle. The nominal phase step is assumed to be constant at

$$\Delta\varphi_{\text{pilot,nom}} = 2\pi \cdot f_{\text{pilot}} \cdot T_{\text{readout}} \tag{3.8}$$

with T_{readout} being the readout period.

Due to the fact that the signal of interest has passed the same ADC and that there
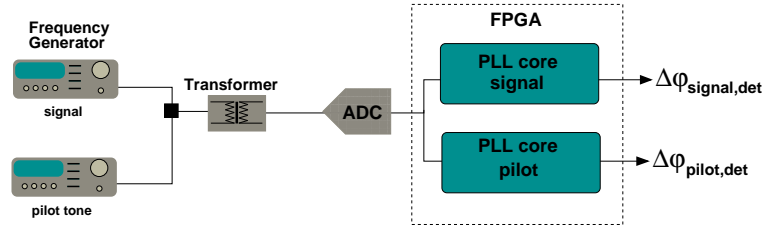
Figure 3.19: *Setup for the jitter correction with the pilot tone being the reference; the correction can be performed using only one ADC*

is a linear relation between time jitter induced phase noise and signal frequency the expected phase error due to time jitter for the signal of interest can be calculated as

$$\delta\varphi_{\text{signal}} = \frac{f_{\text{signal}}}{f_{\text{pilot}}} \cdot \delta\varphi_{\text{pilot}} \tag{3.9}$$

This value can then be subtracted from the measured value $\Delta\varphi_{\text{signal,det}}$ to obtain the corrected phase increment value for one readout cycle

$$\Delta\varphi_{\text{signal,cor}} = \Delta\varphi_{\text{signal,det}} - \delta\varphi_{\text{signal}} \tag{3.10}$$

This principle can successively be applied to the whole time series of the measured data to get, after summing up all these values, the jitter corrected phase for the signal of interest.

3.3.3.2 ADC Sampling Process Reference

Since during the work on this thesis no stable pilot tone was available to perform the first correction scheme (section 3.3.3.1), the second one using a relative correction was used to characterise the noise performance of the phasemeter including the jitter correction. The experimental setup is depicted in Figure 3.20. It is a simultaneous zero measurement including two ADCs just as already used in section 3.3.2 (see Figure 3.17 and 3.18). The principle of this correction scheme is basically the same as for the scheme using the pilot tone as time reference. The main difference is that the correction scheme is applied to the phase *differences between the two ADC channels.* In particular the (relative) time jitter is determined via the phase difference between the two channels tracking the pilot tone and not as deviation from a nominal value. In Figure 3.21 the sampling points of each ADC on the incoming signals are sketched. Due to the time jitter, the periods between the two sampling processes of the two ADCs differ. The difference is

$$\delta t = t_2 - t_1 \tag{3.11}$$

This difference is the same for both pilot and signal of interest. It leads to a difference in the measured phase difference (or, more precisely, phase increment difference) for the pilot tone of

$$\delta\varphi_{\text{pilot}} = 2\pi \cdot f_{\text{pilot}} \cdot \delta t \tag{3.12}$$
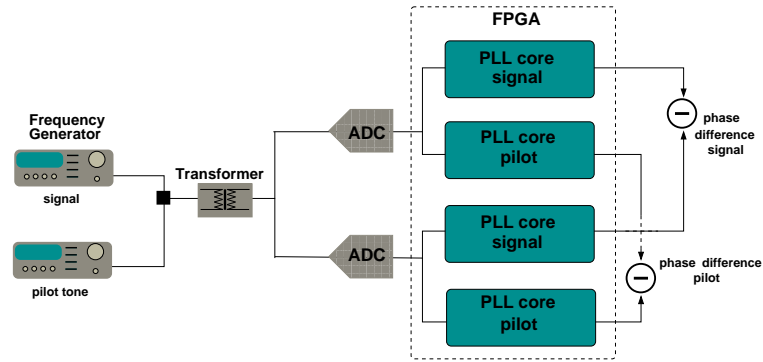
Figure 3.20: *Setup for jitter correction using the period between sampling points of one of the two ADCs as reference; setup can be used to characterise noise performance of the phasemeter.*
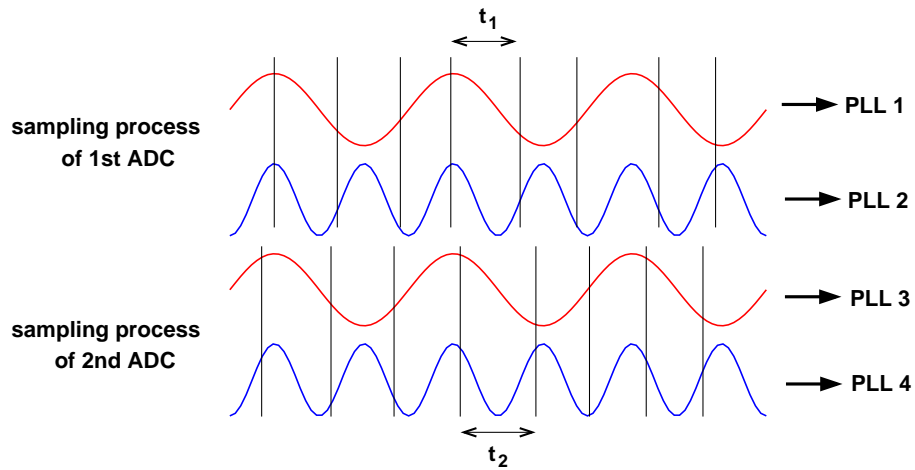
Figure 3.21: *The sampling points (black vertical lines) of the two ADCs jitter differently in time but the difference $t_2 - t_1$ is the same for both pilot tone and signal.*
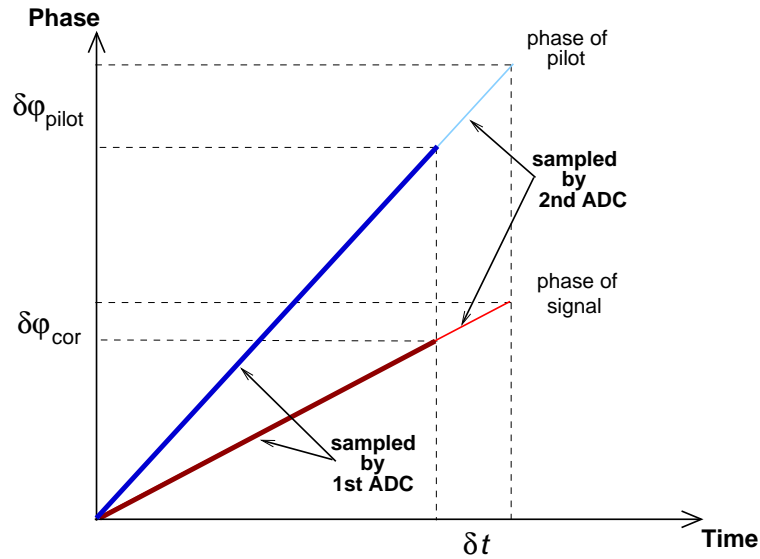
Figure 3.22: *Assuming both pilot tone and signal to be constant during one readout cycle the correction term for the signal $\delta\varphi_{\mathrm{corr}}$ can easily be obtained from the difference in phase difference $\delta\varphi_{\mathrm{pilot}}$.*

In Figure 3.22 the effect of this time difference in the sampling process on the measured phase during one readout cycle is sketched. It shows the phases that the two signals have processed during one readout cycle having passed the first ADC or the second ADC, respectively. For simplicity the origin is assumed to be the same for all curves. This assumption is justified because the correction is performed for one readout cycle where the zero time stamp is set by the FPGA clock. The correction is then performed with respect to the sampling process of *one* of the two ADCs. The correction term for the phase increment can easily be determined from this sketch as

$$\delta\varphi_{\mathrm{corr}} = \frac{f_{\mathrm{signal}}}{f_{\mathrm{pilot}}} \cdot \delta\varphi_{\mathrm{pilot}} \tag{3.13}$$

One can now either subtract this value from the measured phase increment value of the signal that passed the second ADC or add it to the one having passed the first ADC. One just has to be consistent over the whole time series.

Basically this correction scheme 'pretends' that e.g. the first ADC jitters in the same manner as the second one does.

3.3.4 Experimental Results

The jitter correction scheme explained above was used to correct a 2 MHz input signal using a 20 MHz signal as pilot tone. The setup used was the same already shown in Figure 3.17 and Figure 3.20 but it is for completeness shown in Figure 3.23. The 20 MHz signal serves as pilot tone to perform a jitter correction on the 2 MHz input signal just as explained in the previous subsection.

The results of the jitter correction of the 2 MHz signal are shown in Figure 3.24 and Figure 3.25.
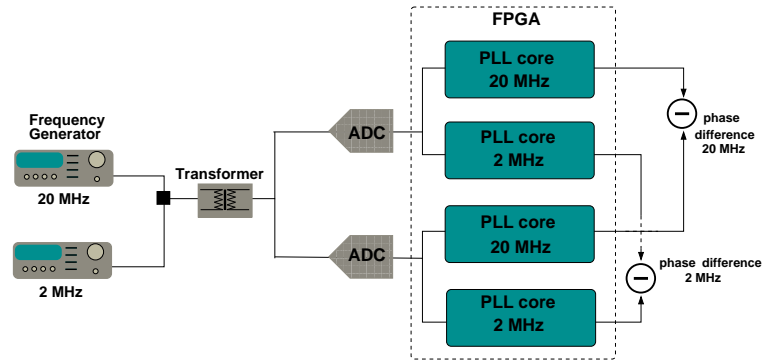
Figure 3.23: *With the setup already used in subsection 3.3.2 the jitter correction of the 2 MHz signal was performed using 20 MHz as pilot tone.*
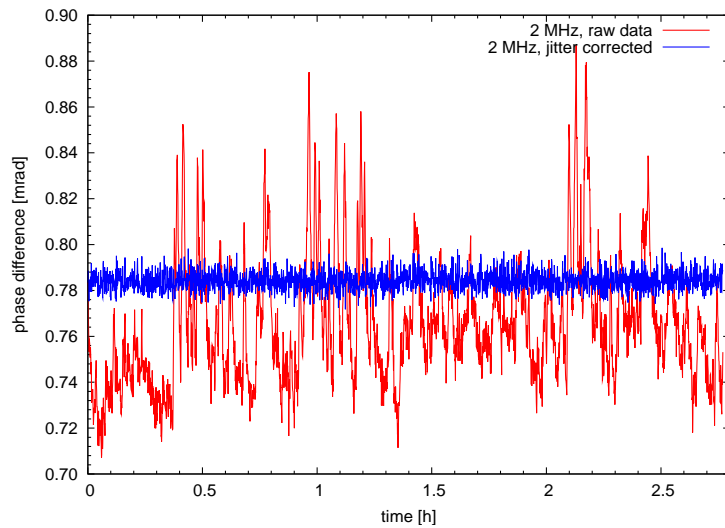
Figure 3.24: *The time jitter corrected time series (blue) of the 2 MHz input signal shows significant improvement with respect to the uncorrected one (red).*

Figure 3.24 shows the raw data (not corrected) time series of the phase difference for the 2 MHz input signal compared to the jitter corrected time series. The improvement can clearly be seen. The low frequency fluctuations with amplitudes present in the uncorrected data about 0.18 mrad peak-to-peak have completely disappeared. The jitter corrected timeseries is flat at a constant offset level with fluctuations in the order of microradians. The corresponding spectral densities are shown in Figure 3.25. The noise curve of the corrected 2 MHz timeseries is (below 1 Hz Fourier frequency) up to 2 orders of magnitude below the noise of the uncorrected curve. It clearly meets the desired requirements. Furthermore down to about 10 mHz the curve of the corrected data is flat at approximately $1\,\mu\mathrm{rad}/\sqrt{\mathrm{Hz}}$. This indicates (cf. section 3.2.4) that the sensitivity is limited by digitising noise.
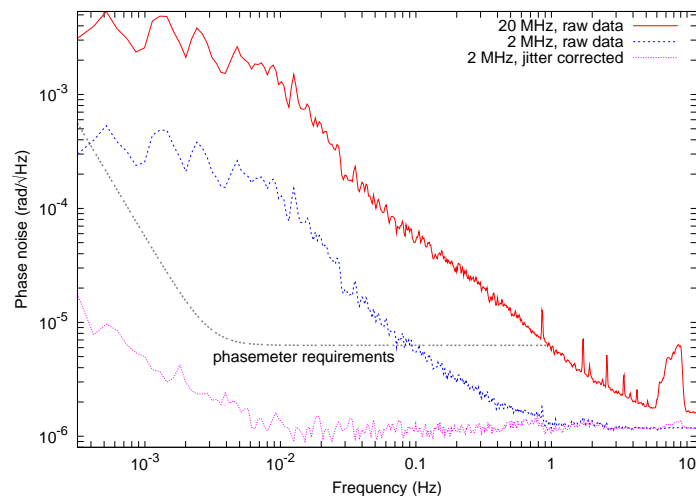
Figure 3.25: *Spectral density of the differential phase measurement for the 20 MHz and the 2 MHz input signals; correcting the 2 MHz signal using a 20 MHz pilot tone clearly meets the requirements.*
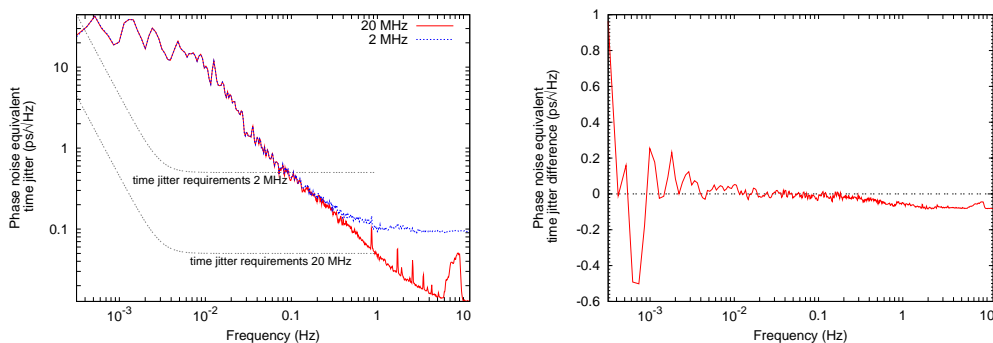
Figure 3.26: *The difference of the phase noise equivalent time jitter between the two input signals (right) underlies higher fluctuations the lower the Fourier frequency is; this downgrades the jitter correction.*

The phase noise of the jitter corrected curve starts to increase below 10 mHz.

The reason for this can be seen in Figure 3.26 showing again (cf. Figure 3.18) the phase noise equivalent time jitter of the 2 MHz and the 20 MHz signal (left graph) and the difference between these two curves (right graph). It shows that this difference is not perfectly at zero as one might think if one just looks at the left graph which has a logarithmically scaled y-axis. Figure 3.26 shows that the phase noise equivalent time jitters for 2 MHz and 20 MHz coincide less for lower Fourier frequencies. This indicates that there must be additional noise sources having a different input frequency dependence than the time jitter has. This noise does not dominate the time jitter but it makes the jitter correction less efficient since this correction scheme is based on the linear input frequency dependence between time jitter and phase noise. The experiment was also performed using a 12 MHz input
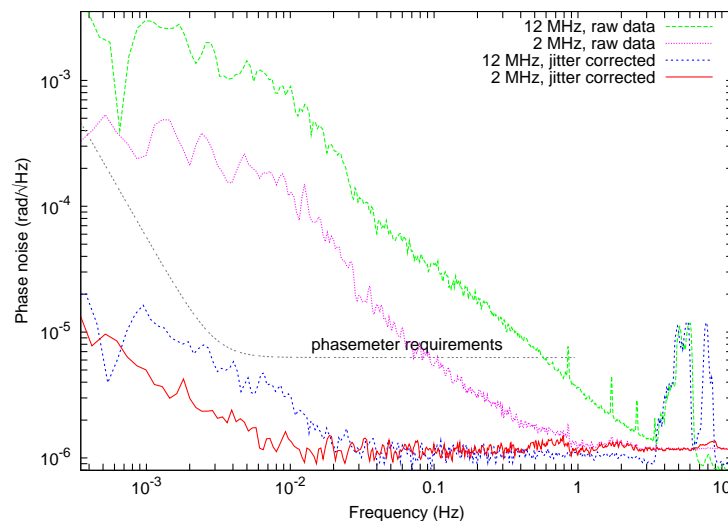
Figure 3.27: *Spectral densities for the corrected time series of a 12 MHz and a 2 MHz input signal using a 20 MHz pilot tone are below the requirements.*

signal to be jitter corrected by means of the 20 MHz pilot tone. The results of this measurement compared to the one carried out with a 2 MHz input signal are shown in Figure 3.27. Apart from the broad peaks above 3 Hz appearing in the spectral estimate of the 12 MHz input signal both jitter corrected curves show similar behaviour. The corrected noise curve of the 12 MHz signal starts to increase already below 30 mHz but it still meets the requirements.

One can regard these first measurements applying a jitter correction to the signal of interest as a very successful proof of principle. The correction scheme works very well and at least for a 2 MHz and a 12 MHz signal the raw data can be corrected to a level below the requirements using a 20 MHz signal as calibration tone.

To further improve the accuracy of this measurements and to correct for input signals up to 20 MHz (the maximum LISA heterodyne frequency) pilot tones with frequencies higher than 20 MHz were chosen. Experiments have shown that pilot tone frequencies of 48 MHz, 49 MHz, 49.5 MHz and 72 MHz yielded excellent results (this can be seen in the next section). Since the sampling frequency of the system is 50 MHz (corresponding to 25 MHz Nyquist frequency) these signals are aliased
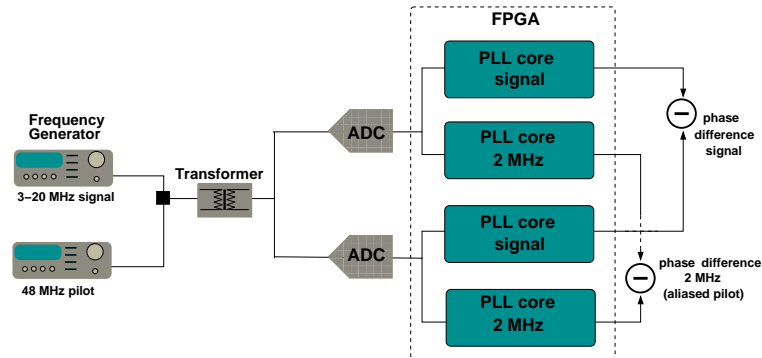
Figure 3.28: *Setup for performing a zero measurement with jitter correction using a 48 MHz calibration tone; the PLL has to track the aliased 2 MHz signal.*

down to 2 MHz, 1 MHz, 0.5 MHz and 22 MHz, respectively. The phase noise caused by time jitter is **not** scaled down when the signal is aliased. This means that the time jitter induced phase noise of e.g. a 48 MHz input signal appears unchanged (apart from its sign) in the detected 2 MHz signal. The advantage of these high
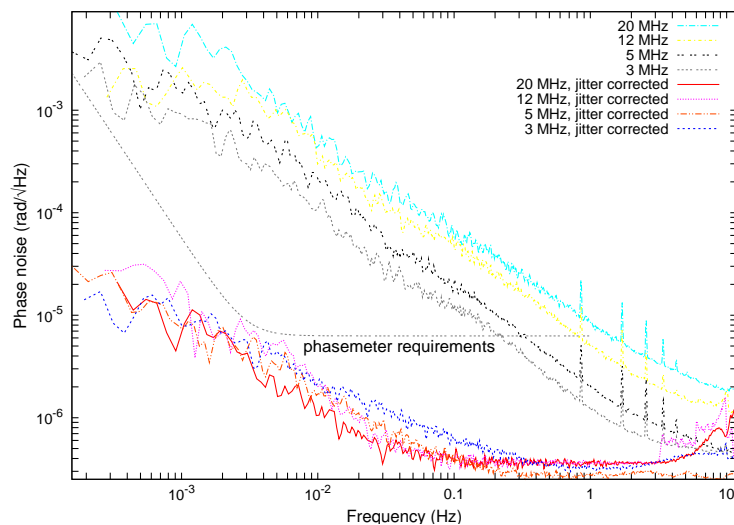
Figure 3.29: *For input frequencies between 3 and 20 MHz corrected by means of a 48 MHz calibration tone the corrected noise curves are at comparable levels below the requirements.*

frequency pilot tones is that there is a higher conversion factor between time jitter and phase noise. The relative error of the phase noise gets smaller the higher the pilot tone frequency is (unfortunately this is only valid for the frequencies mentioned above; for a pilot tone frequency of 98 MHz the performance gets worse).

The first pilot tone frequency above the Nyquist limit (25 MHz) was chosen to be 48 MHz being aliased to 2 MHz. Hence 3 MHz was the lowest signal frequency to be jitter corrected. The setup for this measurements is shown in Figure 3.28. It is basically the same setup as for the jitter correction measurements performed before.

The difference is the 48 MHz pilot tone aliased to 2 MHz. This is the frequency the corresponding PLLs have to track.

The results of this measurements using input frequencies between 3 and 20 MHz are shown in Figure 3.29. The graphical presentation contains the noise curves for the uncorrected and for the corrected time series. All of the jitter corrected noise estimates are below the requirements over the whole frequency range of interest.

The phasemeter sensitivity determined with these experiments already includes the PLLs and the ADCs as noise sources. This had to be further extended by the noise contribution of the analog front end electronics which is topic of the next section.

3.4 Analog Front End Noise

In the previous section it has been shown that the jitter corrected phase noise of the phasemeter using only one transformer as driving unit for two ADC channels is well below the requirements. Since the input signal is split directly in front of the ADCs, all these measurements do **not** yet include any noise contribution of the analog front end. These contributions, i.e. noise of transformers, are common for both ADC channels and should cancel by subtraction of the reconstructed phase values of the two channels in post-processing in these experiments. In the real application, however, there have to be separate front ends for each channel.

In this section the noise investigations will be extended to the ADC driving units (which used to be the manufacturer recommended transformers) meaning that instead of one ADC driving unit (a transformer) splitting *one* signal into *two* ADC channels each ADC will now be driven by a separate device. Since not common mode for both input channels the noise introduced will no longer cancel by subtraction but of course the sensitivity requirements have to be met also with this additional noise contribution.

There were three different possibilities under investigation:

- designs using transformers (section 3.4.1)

- a capacitive coupling scheme (section 3.4.2)

- a design using fully differential OpAmps (section 3.4.4)

In secton 3.4.3 the disadvantages of the transformer design and the capacitor design will be pointed out. It will be shown that the only design having the desired features for adding pilot tone and beat-note signal and for properly driving the ADCs is the OpAmp design. Furthermore it will be demonstrated that this design is capable of fulfilling the sensitivity requirements of the phasemeter over the whole frequency range of interest (0.1 mHz to 1 Hz) for beat-notes between 2 and 20 MHz.

3.4.1 Transformer Design

Due to the very good results using one transformer (MC ADT1-1WT+, recommended by ADC manufacturer, see section 3.3.4) the first choice for signal injection with separated ADC driving units was to use two transformers. Unfortunately it turned out that the recommended transformers were not capable of delivering satisfying results.

3.4.1.1 2-Transformer Design

To investigate the influence of the analog front end transformers on the phase noise performance of the phasemeter the setup shown in Figure 3.30 was used. It is a zero measurement using a 48 MHz signal as pilot tone for ADC jitter correction. The adding of the pilot tone to the signal takes place by means of the combiner before converting the single ended signals to differential ones. The main difference to the previous sensitivity measurements is that each ADC is now driven by its individual transformer.
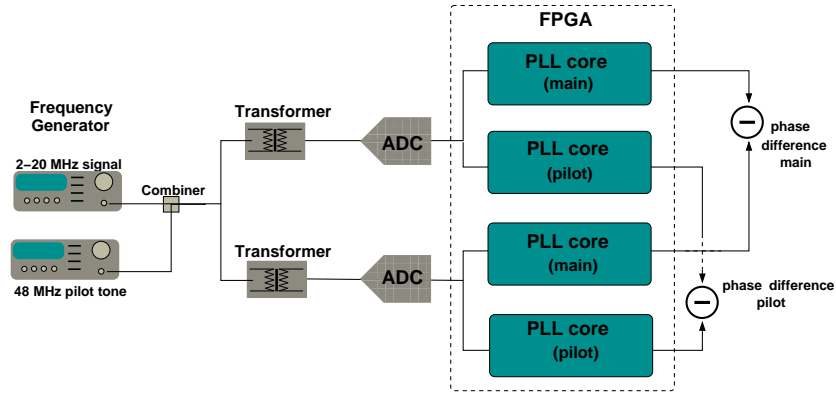
Figure 3.30: *Correction setup for investigating analog front end noise of transformers*

Using this setup the noise introduced by the transformers is not identical for both input channels and will not cancel by subtraction.
The result of this measurement compared to the one using only one transformer is shown in Figure 3.31. These graphs clearly show two major experimental results:

- First, there is an increase in noise for the non-corrected spectra (blue and magenta curve) between 6 mHz and 2 Hz using two transformers.

- Second, the jitter corrected curve for the 2-transformer measurement (red curve) lies essentially right on top of the one representing the noise of the non-corrected signal (blue curve).

Since the jitter correction shows nearly no effect on the signal of interest the phase noise of at least one of the signals (pilot tone or signal of interest) can not be dominated by ADC time jitter noise, otherwise the correction scheme would show a comparable effect as it does for the 1-transformer measurement (orange curve). This can also be seen in Figure 3.32, which shows the phase noise equivalent time jitter $\tilde{t}_{\mathrm{jit}}$ for both the 3 MHz signal and the 48 MHz pilot tone calculated from the phase noise $\tilde{\varphi}$ using the relation

$$\tilde{t}_{\mathrm{jit}} = \frac{\tilde{\varphi}}{2\pi f_{\mathrm{in}}} \tag{3.14}$$

where f_{in} is the corresponding input signal frequency. It can clearly be seen that
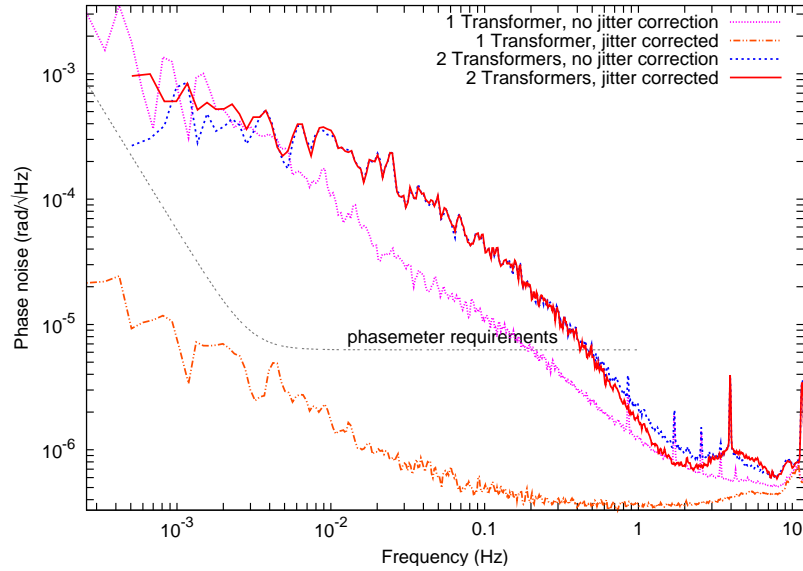
Figure 3.31: *Comparison between jitter corrected spectral density of a 3 MHz signal using one and two transformers*
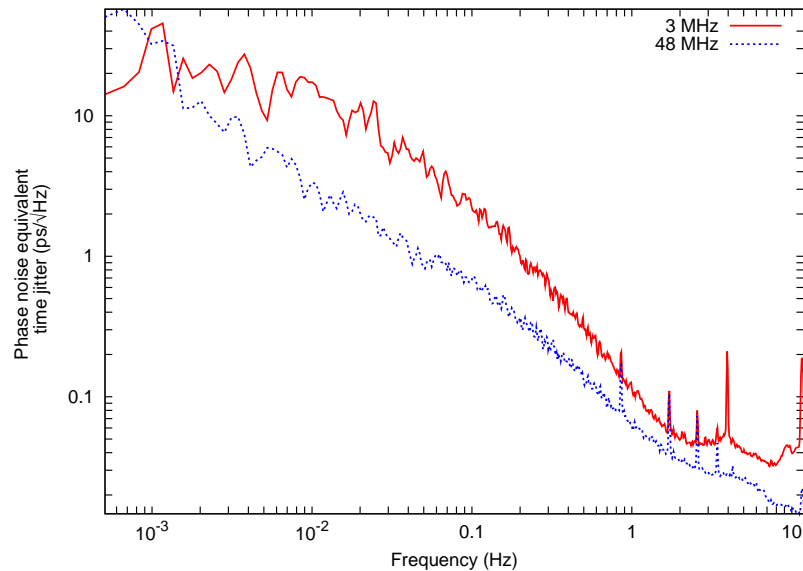
Figure 3.32: *Phase noise equivalent time jitter for 3 MHz and 48 MHz using two transformers*
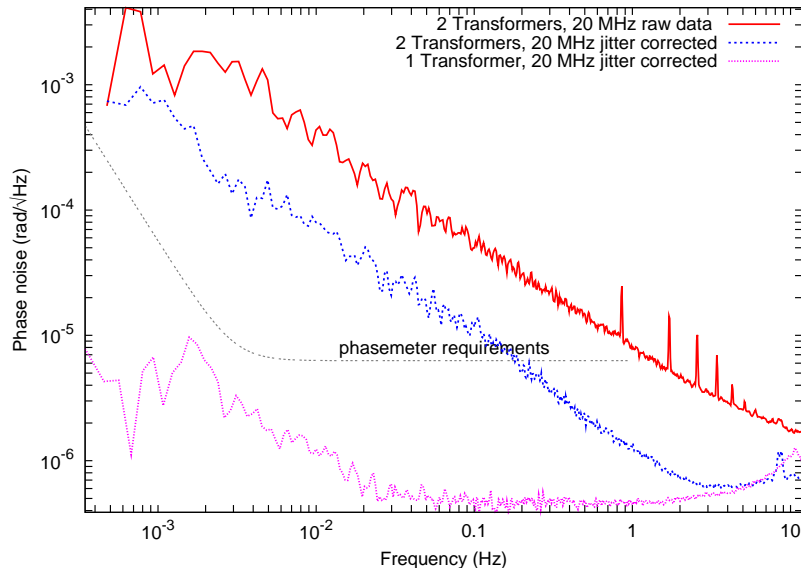
Figure 3.33: *Comparison between jitter corrected spectral density of a 20 MHz signal using one and two transformers*

the equivalent time jitter is higher for the 3 MHz signal. If the time jitter was the dominating noise source for both the pilot tone and the signal the two curves would lie on top of each other. This means that there is an additional noise introducing mechanism having a different frequency dependence than that of the ADC time jitter. In particular the 3 MHz signal experiences a phase equivalent time jitter which is up to a factor of 5 higher than the jitter of the 48 MHz pilot tone. Since the pilot tone correction scheme is based on both pilot and signal being dominated by the very same ADC time jitter the jitter correction does not show any significant effect. The measurement was carried out not only for 3 MHz but also for a 20 MHz input signal. The setup was the one sketched in Figure 3.30. The corresponding noise curves are shown in Figure 3.33. It can be seen that the correction works much better for 20 MHz input than for the 3 MHz input signal but the phase noise even with jitter correction at, e.g., 10 mHz Fourier frequency is still about one order of magnitude above the requirements and about 2 orders of magnitude above the jitter corrected spectral density including no relevant front end noise.

The reason for this high front end noise is probably variations in the phase behaviour of the transfer function of the transformers caused by thermal environmental fluctuations. These variations are different for the two transformers and result in a differential phase noise that dominates the time jitter noise in particular for the 3 MHz signal.

3.4.1.2 3-Transformer Design

In all implementations described so far the pilot tone was always added to the signal of interest before being converted into a differential signal for ADC input. This has the disadvantage that the pilot tone may experience phase noise in the analog front

end paths. The frequency dependence of this noise most probably differs from that of the ADC time jitter and might even dominate it. A proper jitter correction would
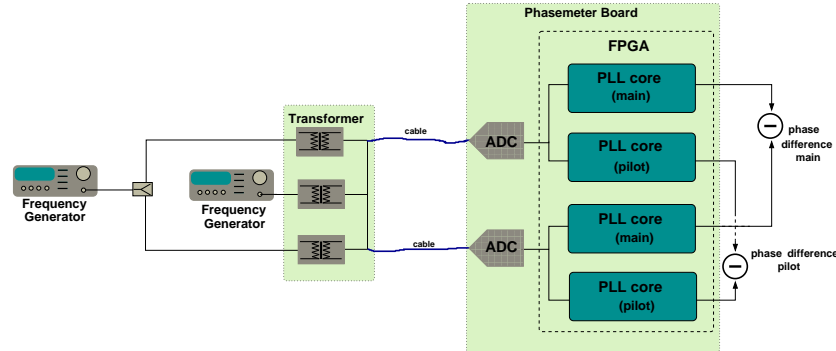
Figure 3.34: *Setup for phasemeter sensitivity measurement using three transformers*

not be possible anymore even if the signal of interest would be dominated by jitter noise. One possibility to avoid this drawback is to use the analog front end depicted in Figure 3.34. The transformers were placed on a separate PCB board and were connected by cables (Figure 3.34, blue) to the phasemeter board. The pilot tone is passing only one single transformer, so the phase noise introduced by this device is common mode for the pilot tone in both phasemeter channels and should not influence a relative jitter correction. Unfortunately (it can easily be seen from Figure 3.34) there is a short-circuit between the two ADC input signals meaning that this design is not suitable to measure two different input signals separately. This setup can only be used to characterise the sensitivity of the phasemeter without noise contribution of the transformers, but with the additional noise of the cables connecting the transformer board with the phasemeter board. These cables (e.g. their lengths) are affected by thermal fluctuations of the environment. In the previous experiments the transformers were placed directly on the phasemeter board with rigid PCB-track connections to the ADCs.

There were basically three different measurements performed using a 12 MHz input signal and a 72 MHz pilot, which turned out to be the most promising pilot tone frequency for this design. The measurement was performed without any thermal isolation of the whole setup, then with better isolation (setup was placed under plastic cover) and finally with better isolation *and* shortened cables connecting the transformers to the ADCs. The results can be seen in Figure 3.35. There is a clear improvement when there is a better thermal isolation of the whole setup. This might be due to the cables being less affected by temperature fluctuations but also to all other analog components involved in the experiment since they were also placed in a thermally more stable environment. Another improvement in the phase noise performance, which is even more significant, can be achieved by using shorter cables between transformers and ADCs. In Figure 3.36 the results for various input frequencies between 2 and 20 MHz can be seen. The pilot tone frequency was 72 MHz. The phase noise for all used beat-note frequencies meet the requirements, only at 19 and 20 MHz the curves slightly touch the 3 mHz knee of the requirements.

As already mentioned the drawback of this design is the short-circuit after the two
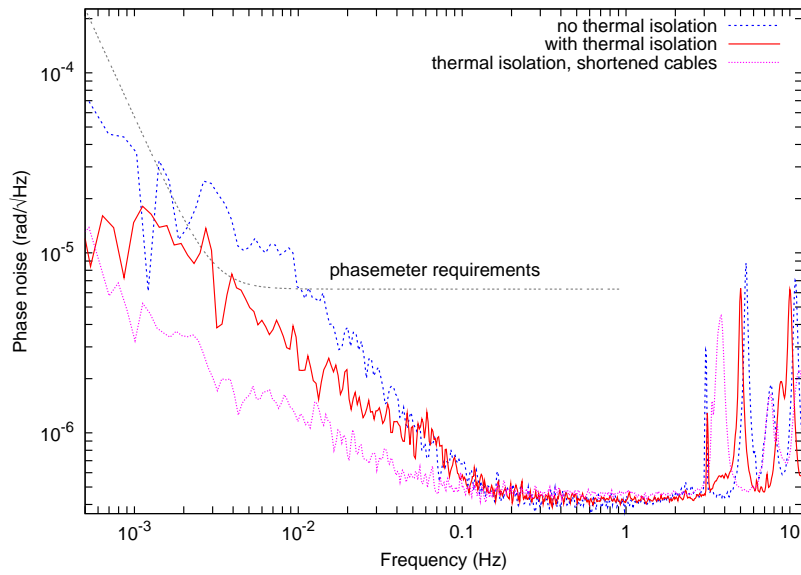
Figure 3.35: *Spectra showing influence of cables on the noise performance for a 12 MHz input signal*
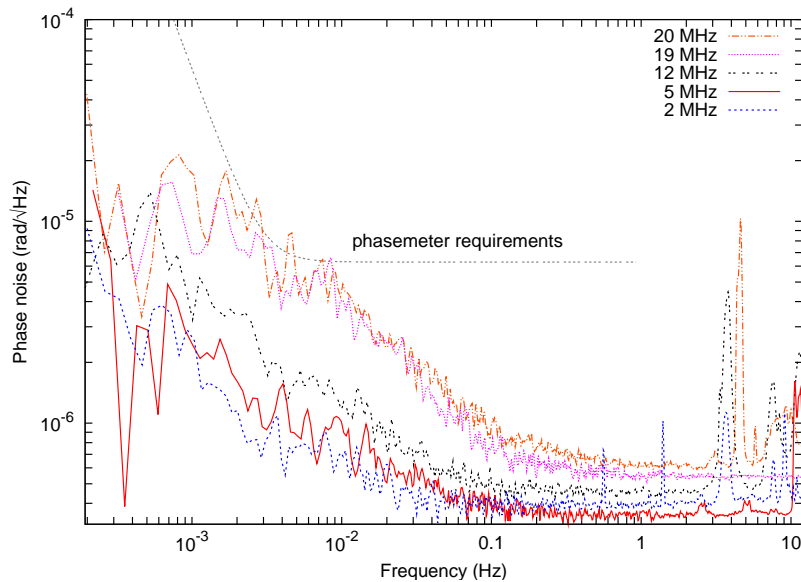
Figure 3.36: *Spectral density of beat-notes between 2 and 20 MHz using the front end design depicted in Figure 3.34*

beat-note converting transformers, meaning that this measurements basically characterises the noise contributions of the devices after the point of short-circuiting. Nevertheless the results obtained by using this three transformer design are important because:

- The method of short-circuiting the signal lines will also be used to characterise the analog front end noise in the framework of [17].

- In Figure 3.35 the importance of avoiding cable connections in the analog front end is obvious. This was a very important result for the work that followed.

- This ADC driving scheme was used to perform the first measurements using optically generated signals which delivered interesting results (see below).

3.4.1.3 Optical Measurements with 3-Transformer Design

The setup depicted in Figure 3.37 was used to perform a measurement using an optical beat-note signal. Compared to the previous measurements the beat-note signal was generated by analog offset phase-locking of two Nd:YAG NPRO lasers (Innolight Mephisto 500 spezial). The results of measurements performed with offset frequencies of 2, 12 and 20 MHz are shown in Figure 3.38. The jitter corrected noise floor is below the requirements in all three cases. As opposed to the electrically generated signal measurements there appear peaks at about 3 mHz (common to the spectral densities of all three beat-notes), at 6 mHz (in the 20 MHz spectral density) and at 10 mHz (in the 2 MHz spectral density). The origin of these peaks was not clear. Later it came out (cf. Section 3.4.4) that the peaks where most probably caused by reducing the bit-length of the NCO output amplitude from 12 to 10 bits.
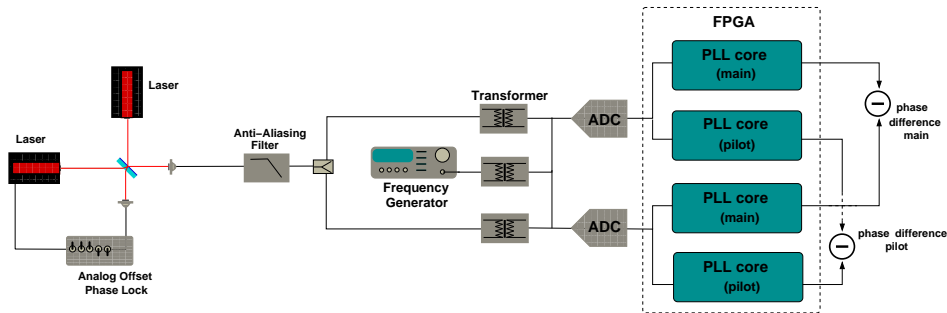
Figure 3.37: *Setup for phasemeter sensitivity measurement using an optically generated beat-note signal as input*

The setup sketched in Figure 3.37 was also used for measuring the phasemeter sensitivity using an input signal generated by the beat-note of two free running lasers (not phase-locked). The timeseries of the beat-note can be seen in Figure 3.39. Its frequency variations over a time of about two hours are in the MHz range. The corresponding spectral noise density of a zero measurement is depicted in 3.40. It is far above the requirements over the whole frequency range of interest. The reason for this is not clear yet, but there is a possible explanation to this behaviour. The high frequency fluctuation (see Figure 3.39) compared to a frequency stable
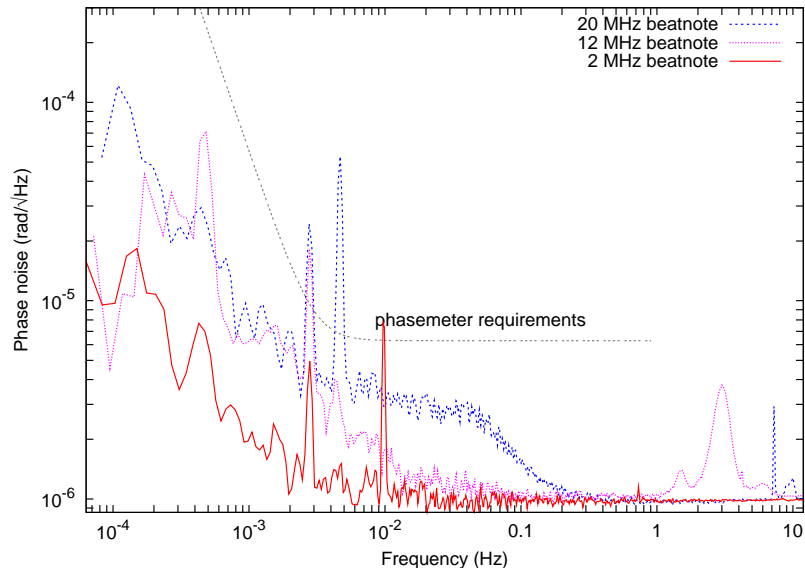
Figure 3.38: *Phasemeter sensitivity using signal generated by offset phase-locked Nd:YAG NPRO lasers*
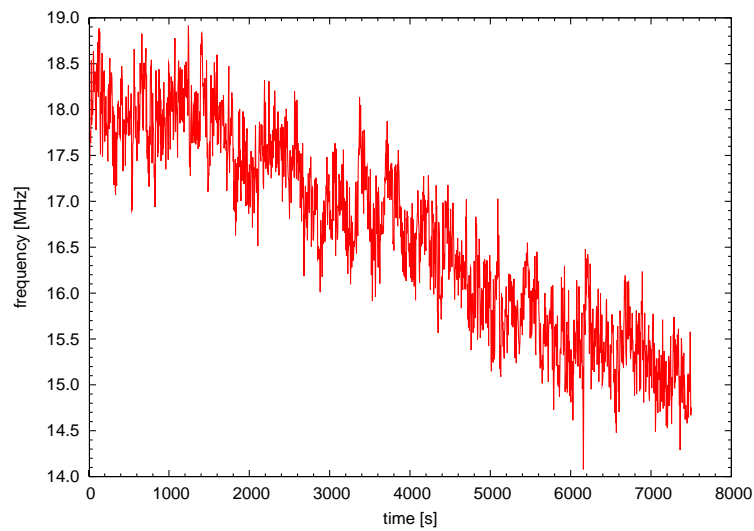
Figure 3.39: *Timeseries of the beat-note frequency of two free running Nd:YAG NPRO lasers*
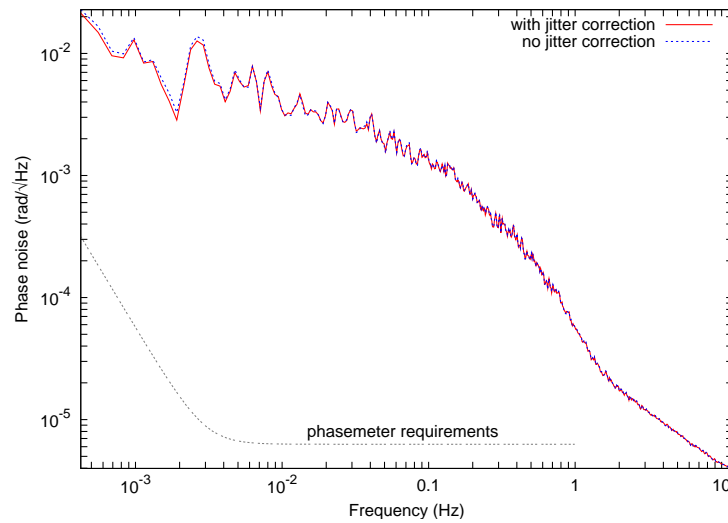
Figure 3.40: *Phasemeter sensitivity using signal generated by free running Nd:YAG NPRO lasers*

input signal delivered by e.g. a frequency generator have severe influence on the noise performance of the phasemeter in particular at frequencies in the vicinity of 17 MHz. This point will become more clear in section 4.1 and 4.2.

3.4.2 Capacitive Coupling

In this section an alternative approach for driving the ADCs and for adding the pilot tone to perform jitter correction is briefly presented.

For this attempt the transformers used in the 2-transformer design were replaced by a capacitive coupling into the ADCs as sketched in Figure 3.41. Film capacitors with 100 pF capacity were implemented. Capacitors are necessary to remove the DC part of the input signal. They are not that sensitive on electro-magnetic environmental disturbances as the coils used in the transformers are, since these

Figure 3.41: *Principle of capacitive coupling*

coils act like antennas. Since the input signals are single ended ones while the ADCs expect a differential input one of the two differential ADC inputs was connected to ground. This is not a desirable solution since the ADC input gets highly asymmetric which is according to the manufacturer not recommended. The setup for the measurements using this capacitively coupled ADC input is sketched in Figure 3.42.

The results of the measurements with 3, 12 and 20 MHz beat-notes are shown in Figure 3.43. The spectral density for the 3 MHz signal meets already the requirements except for the frequency range from approximately 1 to 7 mHz, nevertheless the noise for the 12 and the 20 MHz input signal only meets the requirements above tens of mHz. A comparison between capacitive coupling and two transformer design for the zero measurement using a 20 MHz input signal is depicted in Figure 3.44.
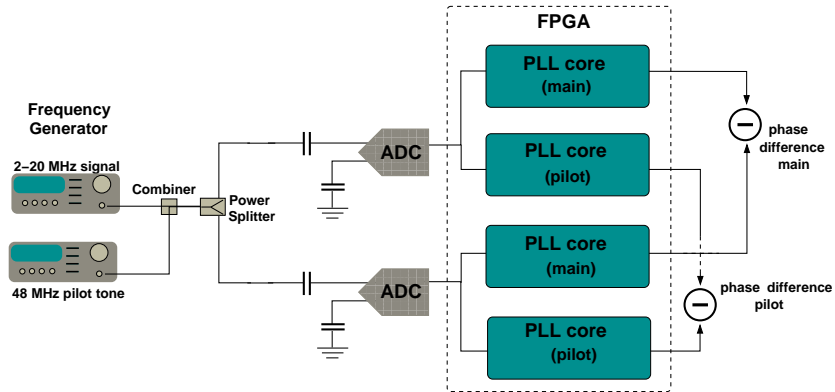
Figure 3.42: *Setup for a zero measurement using capacitive single ended driving of ADCs*
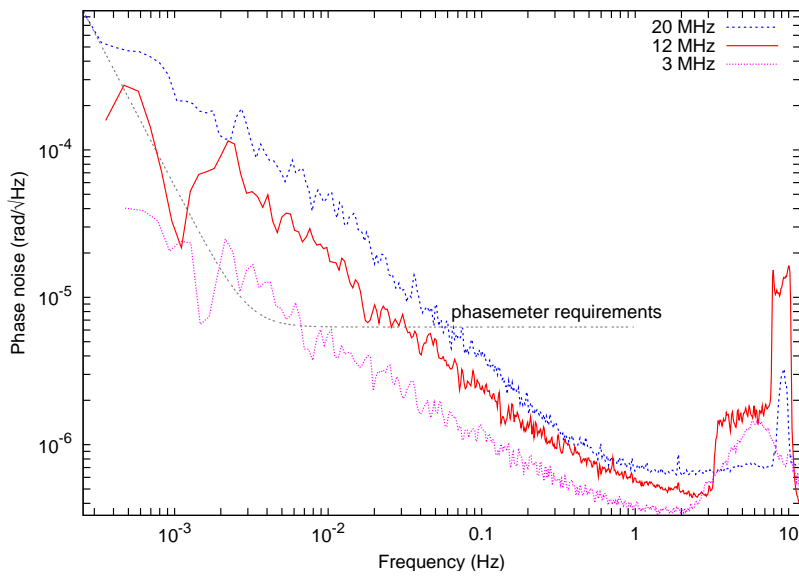
Figure 3.43: *Jitter corrected spectral densities of the capacitive single ended driven ADC measurement*
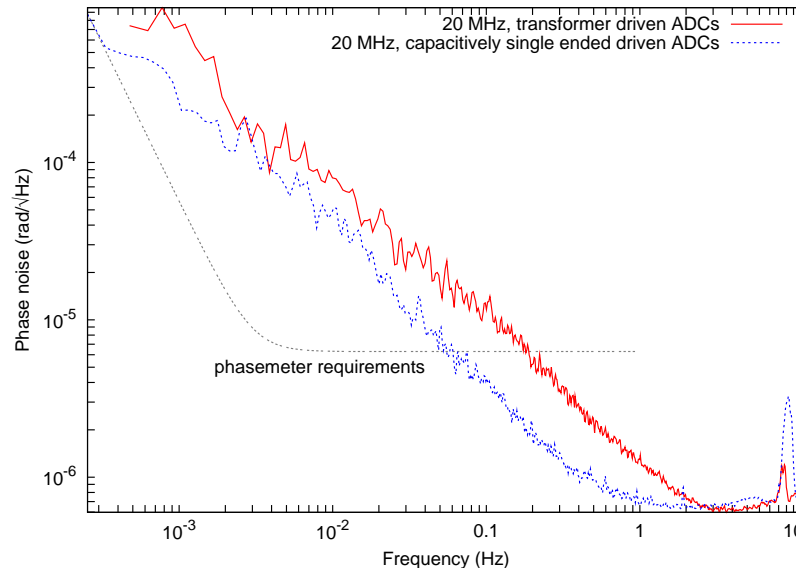
Figure 3.44: *Comparison of jitter corrected spectral densities for a 20 MHz input signal*

Although much to high below 50 mHz the phase noise has significantly improved using no transformers but capacitive signal injection.

Apart from the fact that the ADCs are driven asymmetrically the most probable reason for this analog front end noise is (just as for the transformers) the temperature dependence of the electronic properties of the capacitors causing this differential phase noise.

3.4.3 Fundamental Disadvantages of Transformer and Capacitor Designs

Apart from the dissatisfying phase noise behaviour the designs (with transformers and capacitors, respectively) presented in the previous sections have additional fundamental disadvantages.

In particular the transformer designs were unsuitable for the following reasons:

- For the design using two transformers (Figure 3.30) the jitter correction shows no effect for low frequency input signals, e.g., 3 MHz.

- Transformers are affected by electro-magnetic fields and by thermal fluctuations of the environment. This can not be completely eliminated under laboratory conditions.

- Adding of the pilot tone to the beat-note signal must be done by means of a power splitter (Figure 3.45) if two different beat-note signals from e.g. photodiodes are under investigation, otherwise there would be a short-circuit between the signal lines. This power splitter would be an additional source of noise. (Later it came out that there exist SMD power splitters with acceptable phase noise behaviour).
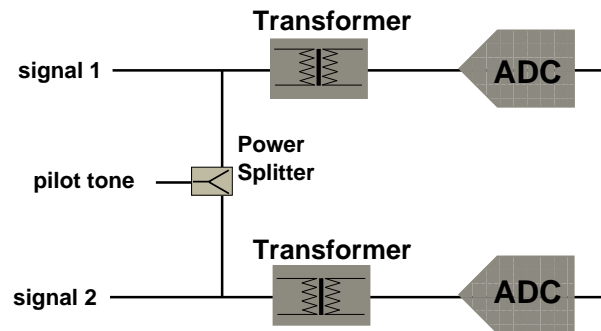
Figure 3.45: *Necessity of using power splitter for pilot tone injection*

- As already mentioned the design using three transformers (Figure 3.34) does not include the transformers as potential noise source due to the short-circuit of the signal lines. It is not applicable for any extension of front end noise investigations.

The design using capacitive coupling also has various fundamental disadvantages:

- The ADCs are driven asymmetrically.

- As for the transformer designs the pilot tone has to be split by a power splitter to decouple the signal lines.

- It is not possible to achieve impedance matching for the input signals between 2 and 20 MHz. This would be a serious problem if the input signals are not identical in frequency.

For all these various disadvantages it was desireable to find a design which fulfils all these practical requirements. One possibility is described in the next section.

3.4.4 Operational Amplifier Design

In the previous sections it has been shown that the attempts using transformers or a capacitive coupling scheme as ADC driving units do not lead to satisfying results. For none of the tested beat-note frequencies the requirements were met due to analog front end noise. Additionally there are the various disadvantages mentioned in section 3.4.3. The approach presented in this section uses Operational Amplifiers (OpAmps). The basic setup is depicted in Figure 3.48. The transformers were replaced by fully differential OpAmps (AD8132, 350 MHz -3 dB bandwidth). These amplifiers were placed on PCB daughter boards (Figure 3.46) that could be attached to the phasemeter board by using the pin connectors also shown in Figure 3.46 to avoid the cable connections between Balun and ADC. Furthermore the OpAmps were used for both adding beat-note signal and pilot tone **and** converting the single ended signals into differential ones as sketched in Figure 3.47. Each single ended input is amplified as for a usual OpAmp. The second output is complementary to the first one. This gives a differential signal obtained from a single ended input. So the cable connection between adding point and Balun is eliminated.
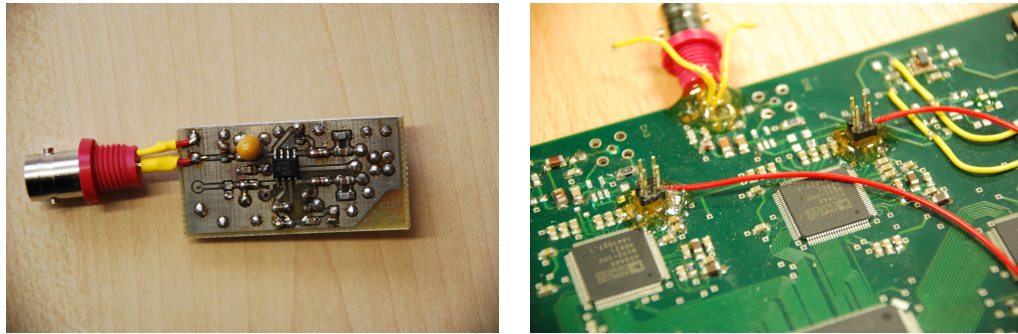
Figure 3.46: *Photos of the daughter board (left, one OpAmp) and the pin connectors on phasemeter board (right)*
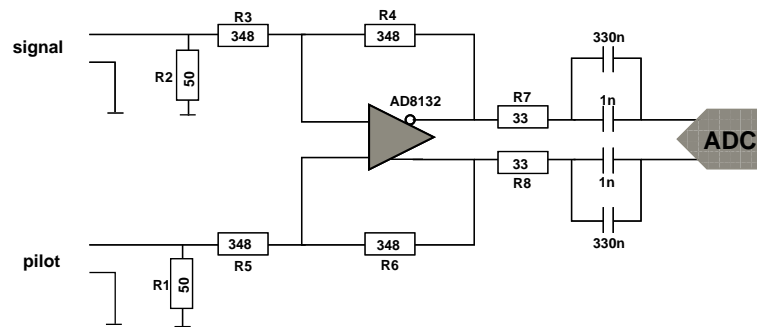
Figure 3.47: *The differential OpAmp converts each single ended input into a differential output. The capacitors remove the DC part of the OpAmp output signal.*

This scheme has the following advantages compared to the methods described before:

- Pilot tones for each input channel are decoupled by means of the OpAmps.

- ADCs are driven symmetrically.

- Impedance matching is possible.

- Fast OpAmps usually show better phase stability than transformers or capacitors do.

For all these reasons the OpAmp design was the one that was followed although the initial results using this front end scheme (see below) were comparable to those of the other ones.

3.4.4.1 Measurements with separated Daughter Boards

The setup of the first measurements using the scheme described above is shown in Figure 3.48. This setup still contains different cable paths for different analog front end channels (after splitting the signal by means of the power splitter and after splitting the pilot tone). These are of course remaining sources of noise. Initially the pilot tone frequency was chosen to be 72 MHz since this turned out to be also

an appropriate choice.   The results of the first measurement using this injection
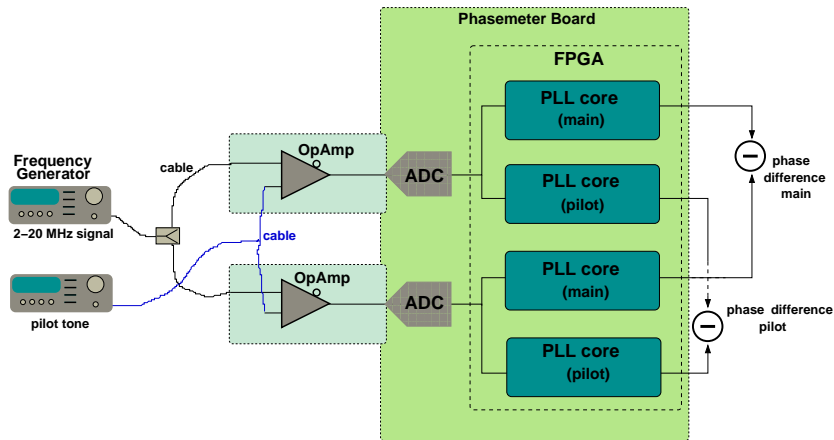
Figure 3.48: *Setup of the first measurement using fully differential OpAmps located on daughter boards*
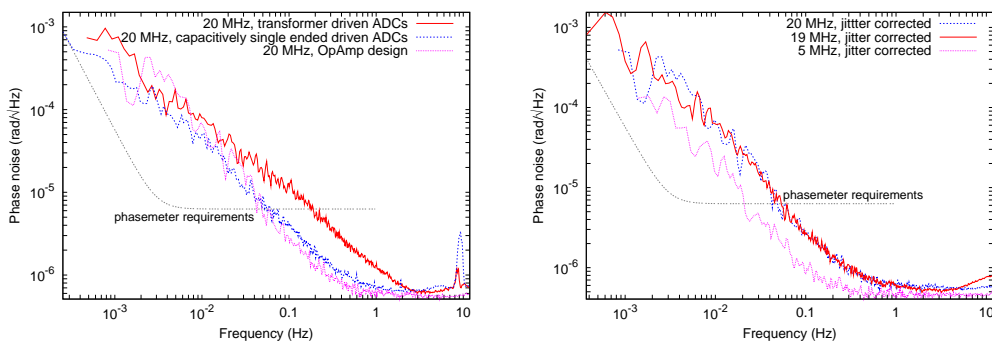
Figure 3.49: *Comparison between phase noise (jitter corrected) for a 20 MHz input signal using 2 transformers, capacitive coupling and 2 operational amplifiers, respectively (left), and comparison between 20 MHz, 19 MHz and 5 MHz measurements using OpAmp design*

scheme for a 20 MHz beat-note is shown in Figure 3.49 compared to the results using one of the other schemes (left) and compared to the results of 19 MHz and a 5 MHz signal measurement using OpAmps (right).   The results using OpAmp design in non-stable thermal conditions are not more promising compared to the previous measurements (in particular the capacitive coupled ADC driving scheme) but for the various reasons explained in the previous section the OpAmp design was the one followed up. Furthermore the measurement of the noise for a 5 MHz beat-note measurement already was quite promising in particular because the jitter correction for lower frequency beat-notes was not possible at all using the transformer design (cf. Figure 3.31). To reduce the noise introduced by the power splitter and by the signal cables (see Figure 3.48) the beat-note signal was split according to Figure 3.50. The power splitter is removed and all cables are kept as short as possible. The improvement for a 19 MHz beat-note measurement can be seen in Figure 3.51 (blue and red curve). Since the cables were still affected by temperature fluctuation (all
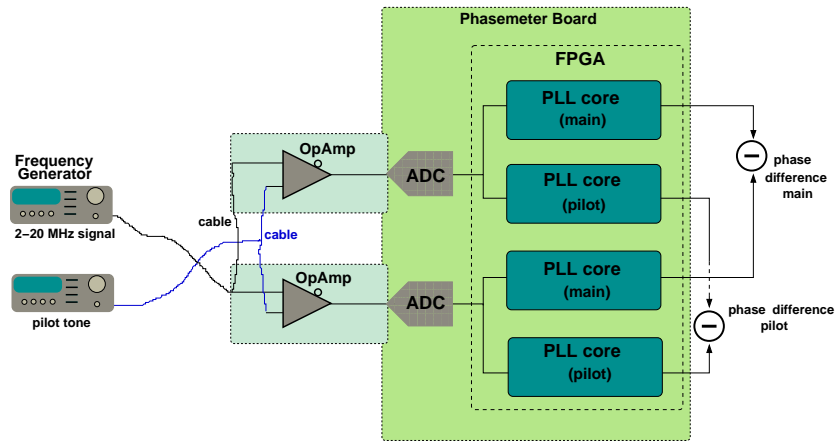
Figure 3.50: *Setup of OpAmp design using separated daughter boards without power splitter and with short cable connections*
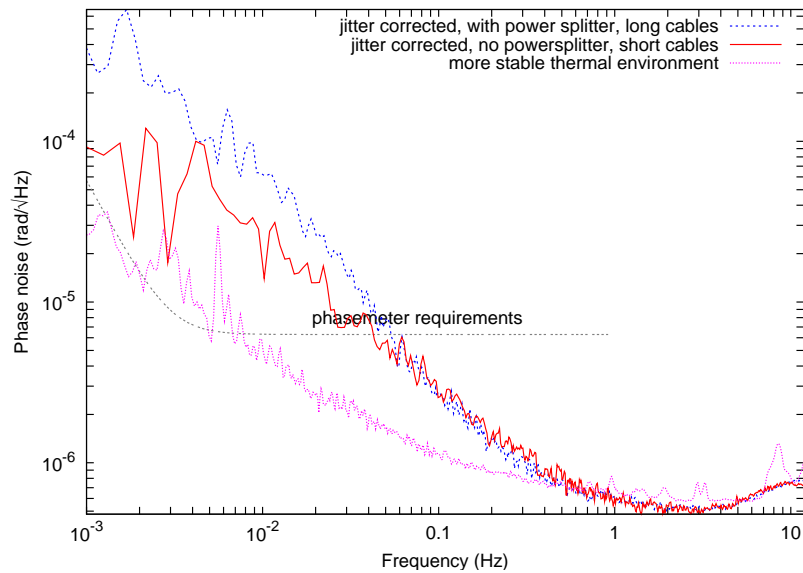
Figure 3.51: *Effect of cables length and environmental temperature stability on a jitter corrected 19 MHz beat-note measurements, pilot tone was 72 MHz*

OpAmp measurements so far were performed under unstable thermal conditions) the measurements were repeated under thermally more stable conditions, i.e., the setup was under a plastic cover in the laboratory. The improvement can also be seen in Figure 3.51 (magenta curve). Figure 3.52 shows the comparison between two sensitivity measurements using 72 MHz pilot and 48 MHz pilot tone frequency. In both cases the beat-note frequency was 19 MHz. It clearly shows a decrease in phase noise when a 48 MHz signal is used for time jitter correction. This measurement has been repeated for other beat-note frequencies which have shown the same result. For the OpAmp design 48 MHz is a better pilot tone choice than 72 MHz is.
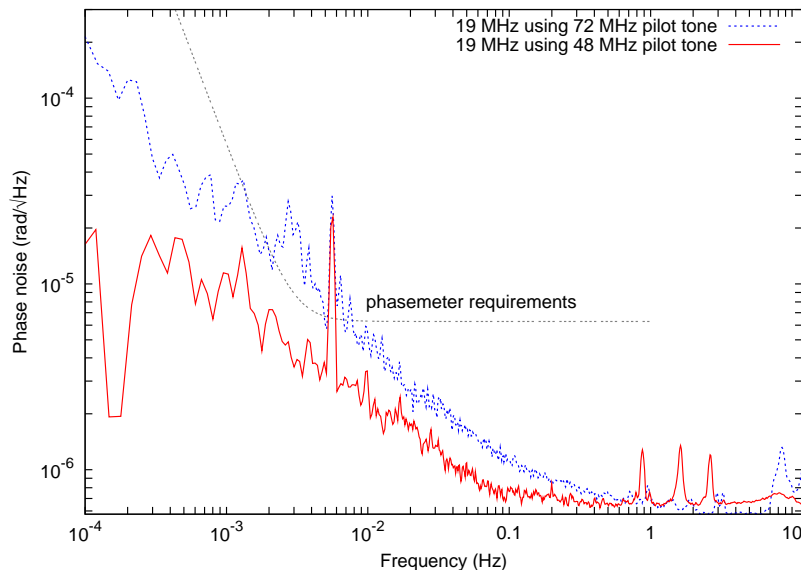
Figure 3.52: *Difference between 19 MHz beat-note measurements being jitter corrected using 72 MHz and 48 MHz pilot tone frequency, respectively*

3.4.4.2 Measurements with one single Daughter Board

3.4.4.2.1 2-OpAmp Measurements   Obviously the analog front end noise can significantly be reduced by avoiding the use of cables (unshielded single conductor stranded wire or even shielded cables with two conductors) which are affected by temperature fluctuations. This has been done by placing all analog front end components sketched in Figure 3.50 and 3.48 on one single PCB front end board using no cable connections but rigid electrical lines on a PCB daughter board. This daughter board, attachable to the phasemeter board, is shown in Figure 3.53 (left) together with the spectral densities (right, 19 MHz input) showing the improvement in sensitivity achieved by avoiding cable connections.

Figure 3.54 shows the comparison for some frequencies between 2 and 20 MHz. The noise floor is well below the requirements. As already mentioned before the peaks appearing in the mHz-range are caused by using 10 bit NCO output instead of 12 bit. This will become obvious in the next paragraph. The peaks appearing in the Hz-range are not yet completely understood. An attempt to explain them is
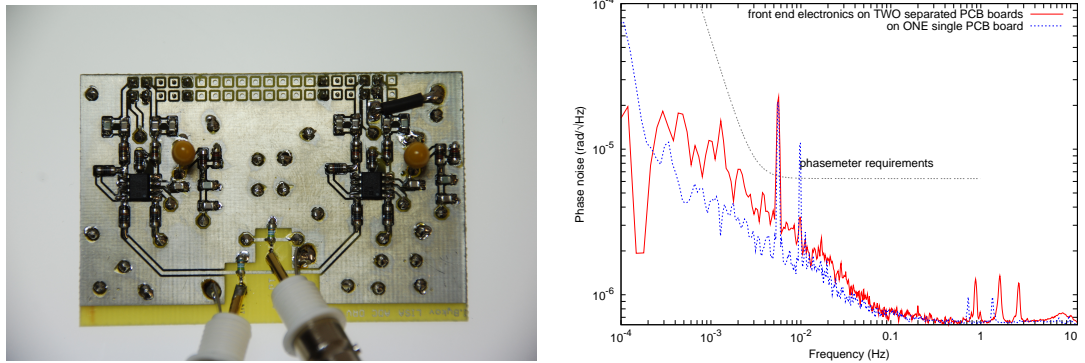
Figure 3.53: *Photograph of a 2 OpAmp single daughter board (left) an the improvement in analog front end noise due to using rigid PCB tracks instead of cables (right) for a 19 MHz jitter corrected input signal*

given in 3.5.2.2.
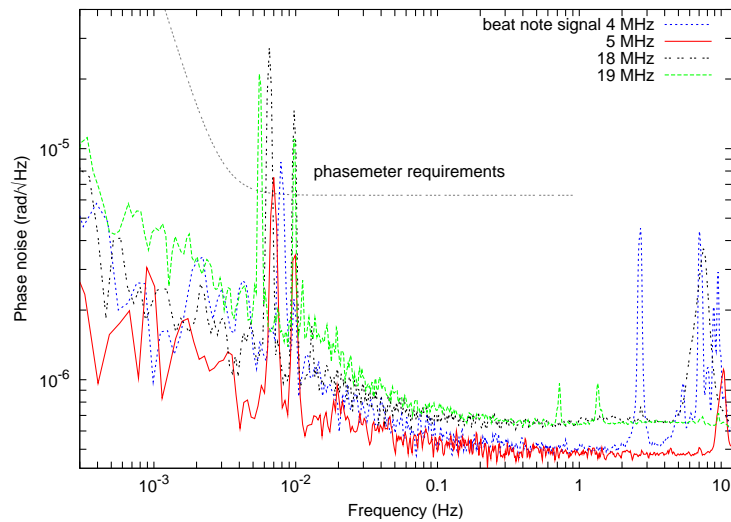
Figure 3.54: *Spectral densities for beat-notes using 2 OpAmps show particular peaks in the mHz and in the Hz-range, noise floor is below requirements, pilot tone frequency was 48 MHz*

3.4.4.2.2 1-OpAmp Measurements From the
previous measurements using two operational am-
plifiers it is not yet clear what the source of the
peaks (Figure 3.54) is. They could be caused by the
analog front end, i.e the OpAmps, by the digitising
process, the PLL itself or they might also be intro-
duced in data post-processing.

To exclude the analog front end as candidate for
this strange behaviour the daughter board shown in
Figure 3.55 containing only one OpAmp was used
as front end. The setup depicted in Figure 3.56 was
chosen to perform a measurement with 18 MHz in-
put frequency. The noise introduced by the OpAmp
is common mode in both ADC channels and should
cancel in subtraction (so this measurement charac-
trises only the phasemeter sensitivity without front
end). As can be seen in Figure 3.57 the peaks re-
main, so they are not caused by the OpAmps.
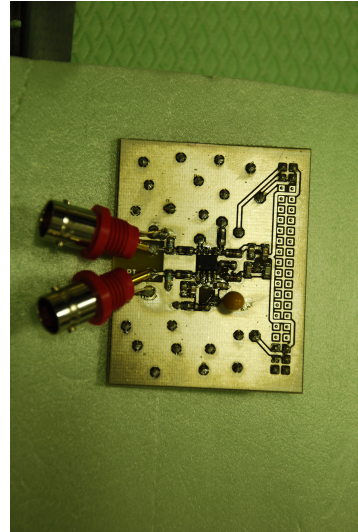
Figure 3.55: *Analog front
end board containing only one
OpAmp*
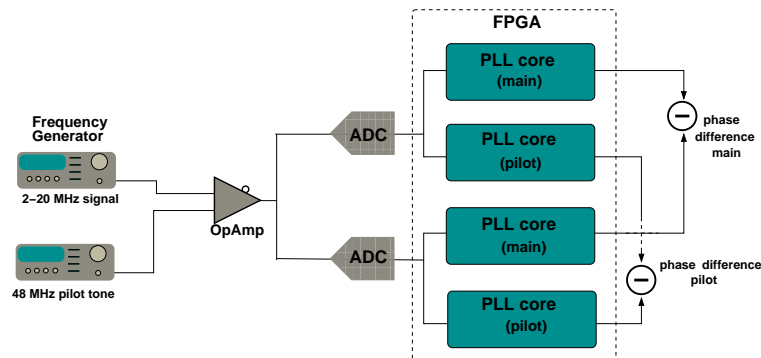
Figure 3.56: *Setup for measuring the phasemeter phase performance using only one
OpAmp to exclude analog front end as noise source*

Another source causing this peaks could be the use of a 10 bit instead of a 12 bit
NCO output in the PLL design which might also be responsible for the peaks emerg-
ing in the spectra of the measurements with optically generated signals (cf. section
3.4.1.3). Figure 3.57 shows the comparison between the two measurements using 12
and 10 bit NCOs. There appear no peaks in the spectral density using a 12 bit NCO
design. Furthermore there is a significant improvement in phase noise for Fourier
frequencies higher than 1 mHz. The digitising white noise limit decreases using an
NCO output bit-length of 12 bits.

For all measurements that follow the 12 bit NCO output was chosen.
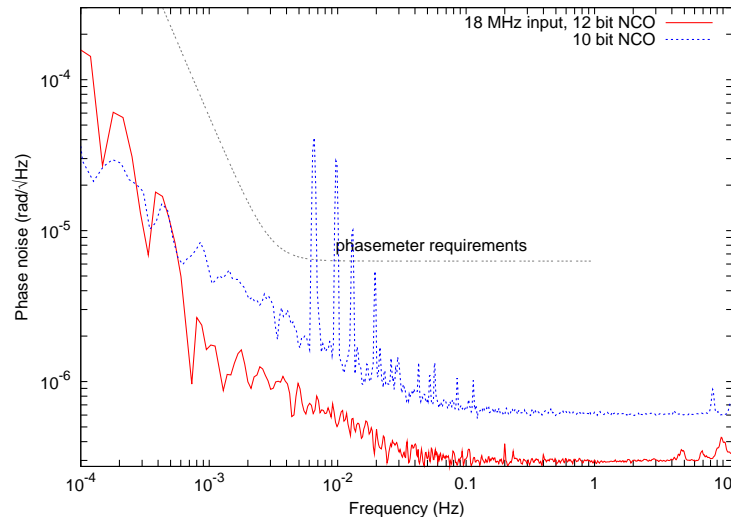
Figure 3.57: *Spectra of 18 MHz zero measurement showing clear dependence of peaks and overall differential phase noise on bit-length of NCO amplitude*

3.5 Phasemeter Sensitivity Summary

In this section the final results for the measured phasemeter sensitivity using electrical unmodulated input signals for one and two analog front end OpAmps are presented. It will be shown that the required sensitivity is met for beat-note signals between 2 and 20 MHz. It should be emphasised that the signals used to determine the sensitivity were all obtained from a signal generator (Tektronix AFG3102) with constant frequency and amplitude i.e. without any modulation. This way of investigating the noise performance has the disadvantage that noise common mode for a fixed frequency input in two different channels can not be detected since it is cancelled by subtraction. But the successful implementation of the zero measurements presented is the precondition for further, more sophisticated investigations to characterise the phasemeter noise performance, in particular the so-called 3-signal-test, which is not a topic of this thesis.

3.5.1 1-OpAmp Measurements

As already mentioned this measurement basically characterises the phase noise performance of the digital part of the phasemeter including the remaining noise after ADC time jitter correction. The chosen setup was the one already depicted in Figure 3.56. A photograph of the analog front end daughter board is shown in Figure 3.58. The main difference to the 1-OpAmp measurements presented in the previous section is the choice of pilot tone frequency. Since a 48 MHz pilot tone is aliased down to 2 MHz the correction of a 2 MHz beat-note signal is not possible. It has turned out that 49.5 MHz pilot tone frequency is an appropriate choice for jitter correcting also the low frequency signals (2 and 3 MHz). The spectral noise densities of this measurement are shown in Figure 3.59.

The most important result is that for all input signals taken within the LISA
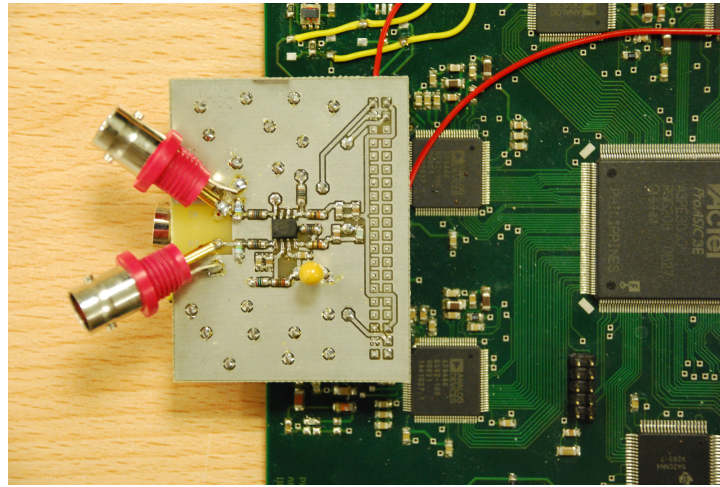
Figure 3.58: *Photograph of the PCB daughter board (one OpAmp) attached to the phasemeter board*
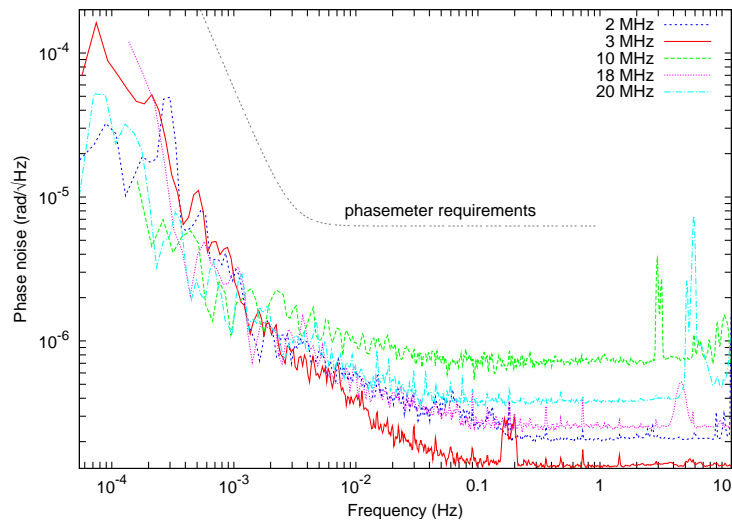
Figure 3.59: *Differential phase noise obtained from a one OpAmp zero measurement with beat-note signals between 2 and 20 MHz. A pilot tone frequency of 49.5 MHz was used.*

beat-note band (2 to 20 MHz) the phasemeter sensitivity is well below the requirements. The sensitivity measured with this OpAmp design is even better than the one measured with the transformer design (cf. section 3.3.4). In particular at the critical Fourier frequency around 3 mHz (the requirement knee) there is a margin of approximately half an order of magnitude. But there is one peculiarity: the flat digitising noise at the higher LISA Fourier frequencies is at different levels for different beat-note frequencies. For a 10 MHz beat-note it is at $0.7\,\mu\mathrm{rad}/\sqrt{\mathrm{Hz}}$ and only at about $0.1\,\mu\mathrm{rad}/\sqrt{\mathrm{Hz}}$ for the 3 MHz signal. The reason for this behaviour is not

clear yet, but there are two possible explanations:

- It is the digitising process in the ADC combined with the digital feedback signal from the NCO that causes this behaviour since the digitising noise is *not* independent of the frequency for $f_{signal} \approx f_{sampling}$ ([40]). But then the question arises why this effect is not present when the transformer is used as ADC driving unit. It is possible that the noise floor for this transformer measurements was not yet low enough to make this effect observable.

- Signals with frequencies that are integer multiples or integer factors of 10 MHz (2, 2.5, 5, 10, 20 MHz) might be affected by a 10 MHz parasitic signal present in the laboratory.

3.5.2 2-OpAmp Measurements

3.5.2.1 Summary of Sensitivity Measurements

The measurement of the previous section was extended to include the noise introduced by the OpAmps. The setup is depicted in Figure 3.60, a photograph of the daughter board containing both OpAmps is shown in Figure 3.61. The differential phase noise curves obtained by carrying out zero measurements for various beat-note frequencies are shown in Figure 3.62 and Figure 3.63 for a 49.5 MHz and a 49 MHz pilot tone, respectively. The amplitude ratio A_{signal}/A_{pilot} was 4, the differential sum amplitude at one ADC input about 2 V_{pp}.

The measurements using a 49.5 MHz pilot tone frequency yielded phase noise estimates well below the requirements for 2 and 3 MHz. The 2 MHz curve shows tiny peaks in the frequency range of interest. The noise floor for the 18 and 10 MHz measurement is quite high and scratches the requirement in the vicinity of 3 mHz. The 20 MHz curve shows out-of-band peaks in the Hz-range, but the results are still acceptable. Using a 49 MHz pilot tone (Figure 3.63) has negative influence on
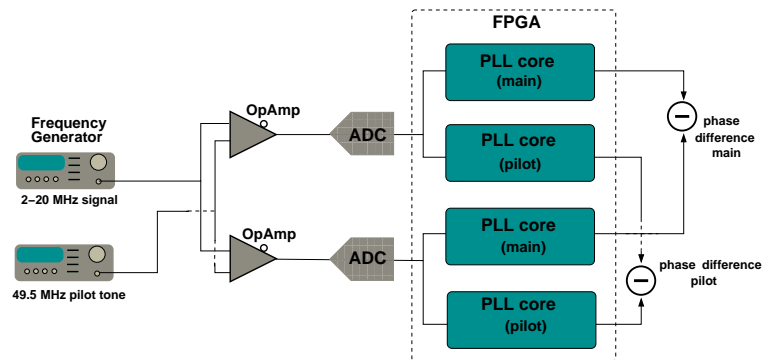
Figure 3.60: *Correction setup with two operational amplifiers*

the 2 MHz signal; the peaks are more pronounced than for the measurement with 49.5 MHz pilot tone but they are still below the requirement. For the higher beat-note frequencies the phase noise performance gets better. All spectra are now well below the requirements. The strange peaks appearing in the Hz-range for 10 and 20 MHz will be briefly discussed in the following section.
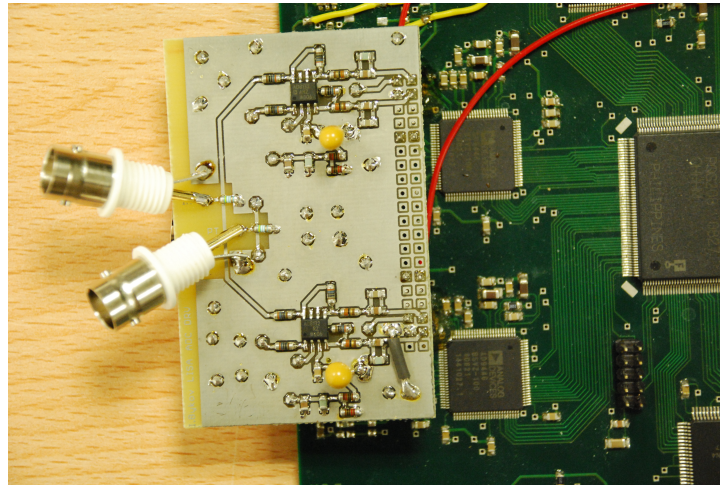
Figure 3.61: *Daughter board contains two operational amplifiers.*
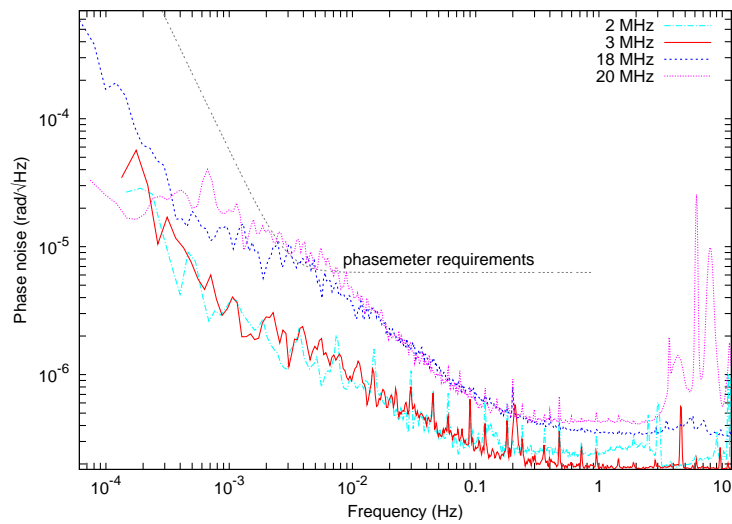
Figure 3.62: *Spectra for two OpAmps slightly exceed the requirements for 18 and 20 MHz when using a 49.5 MHz pilot tone.*
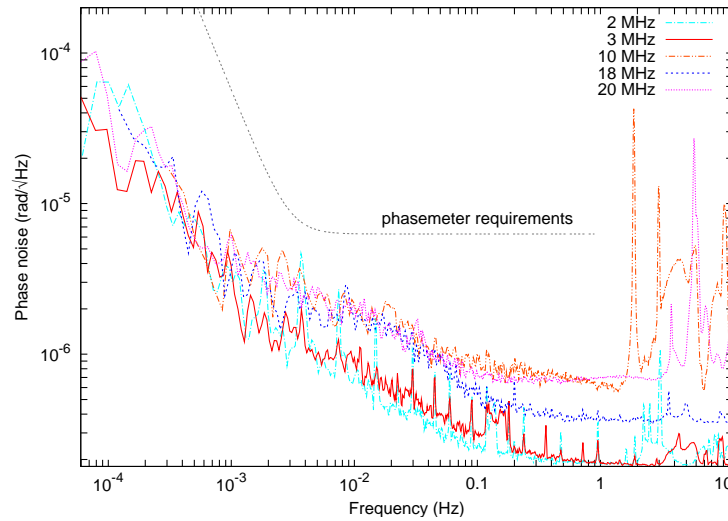
Figure 3.63: *Spectra of various input frequencies using a 49 MHz pilot tone for jitter correction and two OpAmp analog front end*

3.5.2.2 Origin of Sensitivity Peaks

From the graphical presentations shown above it is clear that the peaks appearing in the LISA measurement band for the 2 MHz signal are related to the pilot tone frequency. The cause of the peaks appearing in the noise of the 10 and 20 MHz signal measurements above 1 Hz Fourier frequency is obviously different from that. Since the 20 MHz spectral density for both pilot tone frequencies (49 and 49,5 MHz) appear with comparable significance the main reason for this behaviour is not the pilot tone. This gets more clear from the graphical presentation in Figure 3.64. This measurement was performed with the setup sketched in Figure 3.60 but without pilot tone injection. From Figure 3.64 it is obvious that the pilot tone present in the input channels can not be the cause of this peaks since they are present (red curve) at the same level as in Figure 3.62. Figure 3.64 also shows that for input frequency 1 kHz above 10 MHz these peaks have disappeared at least to the level of the non-corrected phase noise (jitter correction is not possible since no pilot tone is measured). Comparable measurements (setup Figure 3.60) were performed with a 5 MHz and a 2.5 MHz beat-note signal using a 49 MHz pilot tone for jitter correction. The results are shown in Figure 3.65 and show the same effect. For a frequency 200 Hz above 5 MHz or 500 Hz above 2.5 MHz the peaks have nearly disappeared. The interesting point is that this significant peaks do not show up in office measurements and in measurement performed with input signals having an odd frequency value (except 2.5 and 5 MHz). The assumption is that this is also (cf. end of section 3.5.1) caused by parasitic signals present in the laboratory.
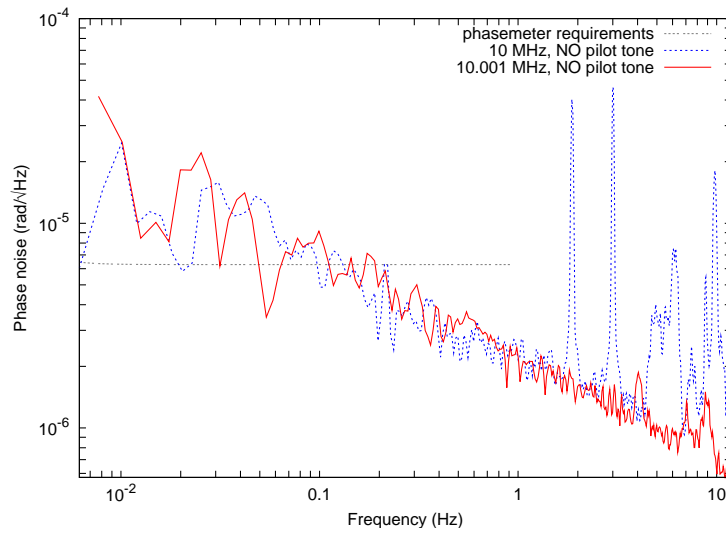
Figure 3.64: *Dependence of peaks above 1 Hz in the vicinity of a 10 MHz beat-note signal in the absence of a pilot tone*
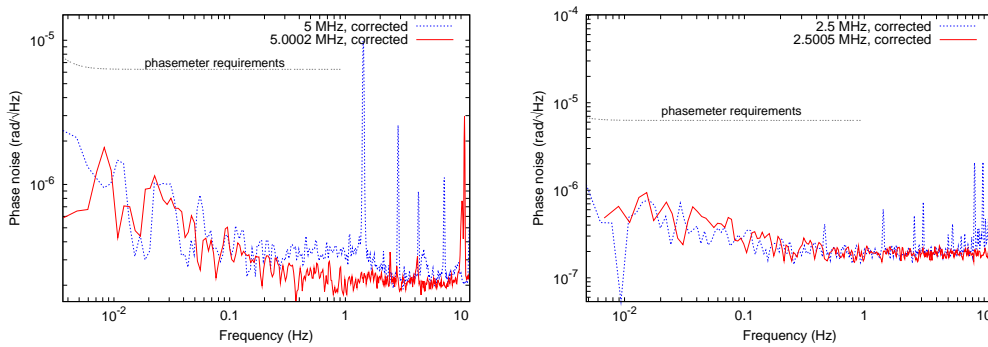
Figure 3.65: *For beat-note frequencies a few hundred Hz above 5 MHz (left) and 2.5 MHz (right) input signal peaks vanish also in the presence of a 49 MHz pilot tone*

3.5.2.3 Sensitivity Dependence on Input Amplitudes

As already mentioned above the optimal amplitude ratio $A_\mathrm{signal}/A_\mathrm{pilot}$ is in the range from 3 to 4. The effect of inverting this ratio can clearly be seen in Figure 3.66. The measurement was taken using an analog front end with two OpAmps. The
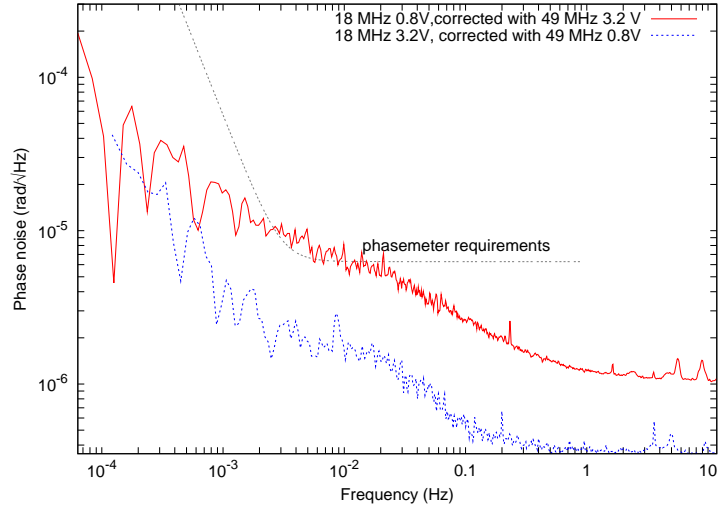
Figure 3.66: *Inverting the amplitude ratio of signal and pilot tone significantly changes the sensitivity of the phasemeter*
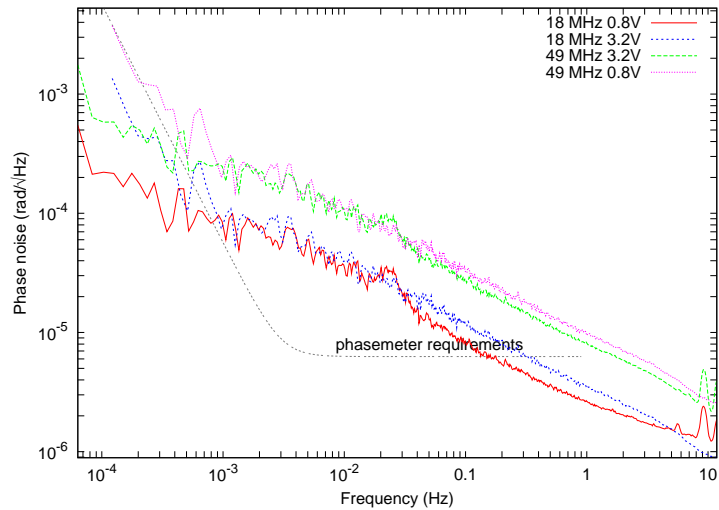
Figure 3.67: *Comparison of the 18 MHz and 49 MHz raw data for different input levels*

amplitude of 3.2 V and 0.8 V are the displayed values of the frequency generator. If the pilot tone is at a high input amplitude level compared to the beat-note signal the phase noise above 1 mHz Fourier frequency increases by a factor of 5. The reason for this is not an increase in the overall phase noise in the raw data of the signal or

the pilot tone as can be seen in Figure 3.67 showing the non-corrected noise curves for the different input amplitudes. The raw data curves corresponding to the poorly corrected result (red curve in Figure 3.66, red and green curve in Figure 3.67) are even below the ones corresponding to the very good result (blue curve in Figure 3.66). The jitter correction for a high pilot and low signal amplitude combination obviously does not work as good as for low pilot and high signal amplitude combination.

3.5.3 Phasemeter Sensitivity Limits

As already seen in subsection 3.2.4 the digitising noise most probably caused by the finite bit length of the NCO output amplitude is a fundamental limit of the phasemeter's sensitivity in particular for the higher frequencies of the LISA band. Another limiting noise source is the finite length of the PIR (and the PA which usually has the same fractional part precision). To investigate the dependence of the phasemeter performance on the PIR precision a zero measurement with $7\,\mathrm{MHz}$ input signal and $48\,\mathrm{MHz}$ pilot tone was carried out. The frequency values obtained from the PIR (converted into decimal code for post-processing) where truncated to different precisions from $10^{-11}\,\mathrm{Hz}$ to $10^{-6}\,\mathrm{Hz}$. Afterwards the phase difference between the two signal channels was reconstructed from this truncated values. The sensitivity results can be seen in Figure 3.68. It can be seen that the PIR precision limits the sensitivity at low frequencies with a $1/f$ envelope while for high Fourier frequencies it is limited by the white digitising noise.
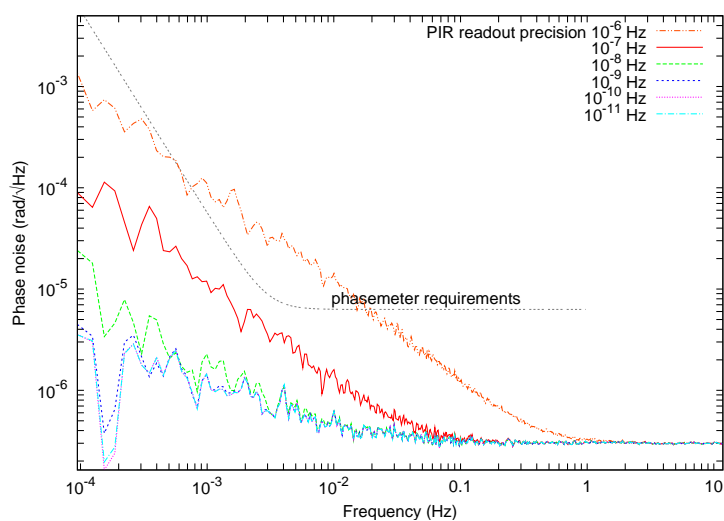
Figure 3.68: *The fundamental digital limits of the phasemeter's sensitivity are digitising noise (flat) and the precision of the PIR driving the NCO (1/f noise)*

3.5.4 Phasemeter Lock-In-Range

In this section the lock-in-ranges for one and two input signals and the phasemeter's capability of separately tracking two nearby input signals will be presented.
The lock-in-range is the maximum deviation of the initial offset frequency (see Figure

3.69) from the input signal frequency for the phasemeter to get locked on the signal. This lock-in process takes at most 200 ms. Experiments have shown that the chosen initial offset frequency must not deviate from the frequency of the input signal by more than 150 kHz. This was tested for 3, 7 and 18 MHz. For higher frequency deviations the system does not get into lock.
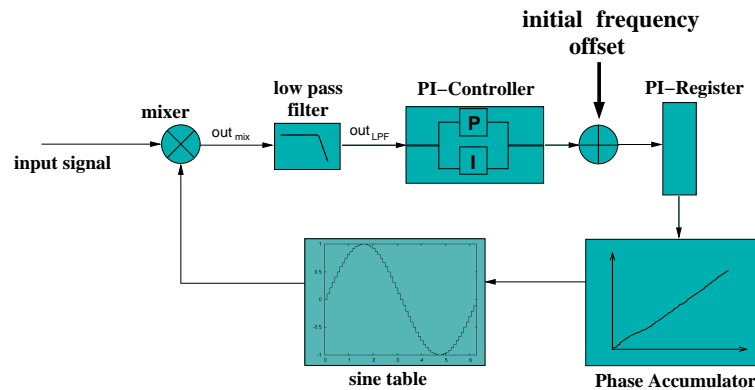
Figure 3.69: *Initial frequency offset has to be chosen close to the input signal frequency to get the PLL track the signal*

3.5.4.1 Lock-in-Range for two distinct Signals

To determine the lock-in-range if 2 different signals are present in the input of the PLLs the setup depicted in Figure 3.70 was used. Signal 2 was set to 7 MHz and signal 1 to 8 MHz. The offset frequencies of PLL core (signal 1) and PLL core (signal 2) (see Figure 3.70) were set exactly to the correct frequency values. The frequency
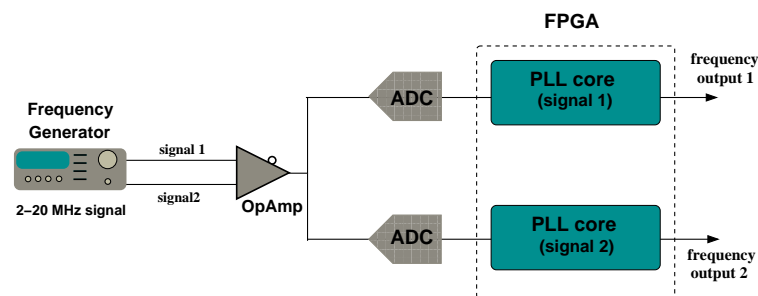
Figure 3.70: *Setup for testing for which initial offset frequency values the PLL locks on one of two input signals separated in frequency by 70 kHz*

of signal 1 was decreased (so was the frequency offset in the corresponding PLL) and the system was restarted. It turned out that for a frequency difference smaller than 70 kHz (signal 1 at 7.07 MHz and signal 2 at 7.00 MHz) the PLLs could not get into lock even if the offset frequencies had precisely the correct value.

By setting the offset frequency higher than 7.07 MHz (lower than 7.00 MHz) a lock on the desired frequency was only possible up to a frequency mismatch between signal and offset frequency of 120 kHz. These results are summarised in Figure 3.71.
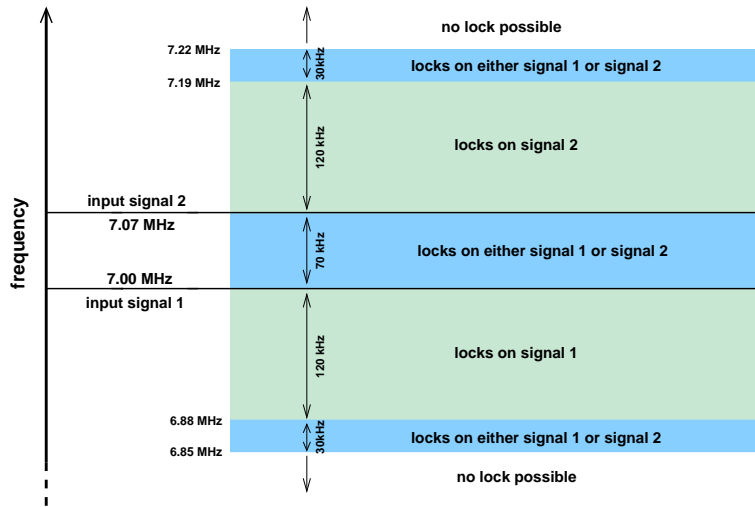
Figure 3.71: *Two nearby (70 kHz distance) signals present in the input of one and the same PLL can only be locked by the PLL for initial offset frequency values in the light green (light blue) shaded area. The frequencies of the input signals were fixed.*

3.5.4.2 Signal Resolution of two locked Signals

The setup depicted in Figure 3.72 was used to determine the minimum frequency distance of two tracked signals before they become indistinguishable for the phasemeter. For this purpose the input signals were set to 8 MHz and 7 MHz, respectively, and locked on by the phasemeter. By decreasing manually the frequency of the signal initially set to 8 MHz it was tested at which frequency distance no precise lock was possible anymore. This measurement was performed also with 18 MHz and 17 MHz input signals. The results of this measurement can be seen in Figure 3.73. As soon
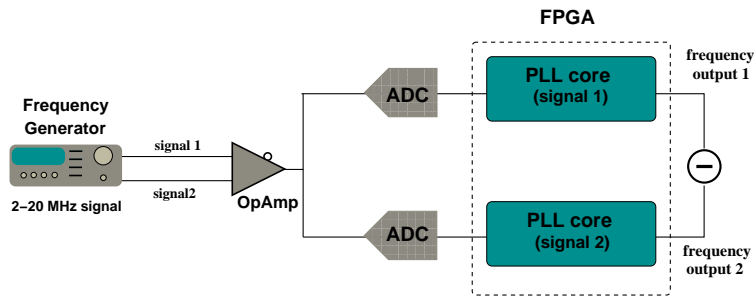
Figure 3.72: *Setup for testing how close signal 1 can approach signal 2 in frequency before the PLL can not resolve the signals*

as the difference between the two input signal has decreased to about 40 kHz the unique lock on each signal is lost, but the phasemeter remains noisy somewhere between the two input frequencies. By further decreasing the frequency difference in 5 kHz steps the tracked frequency difference becomes (at a certain point, 20 kHz for the 17 MHz measurement) exactly zero, so both phasemeter outputs have exactly the same frequency. From Figure 3.74, which shows the frequencies of the tracked

individual signals, one can see that this frequency is not identical to one of the input frequencies (17.00 and 17.02 MHz) but 17.01 MHz.
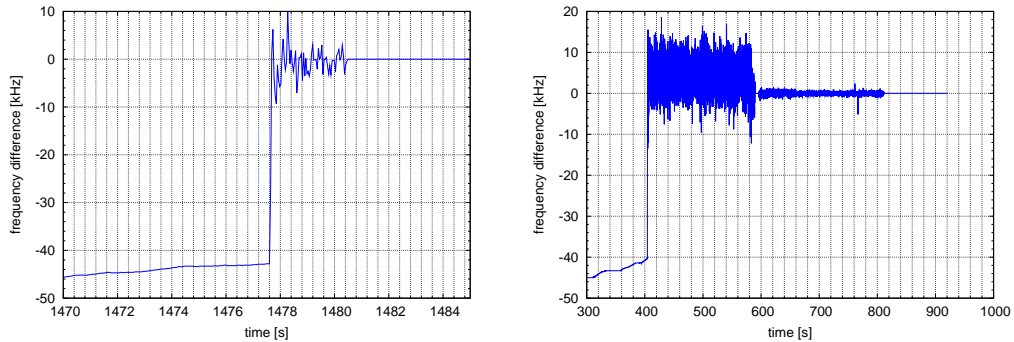
Figure 3.73: *Timeseries of the tracked frequency difference for the inputs close to 7 MHz (left) and close to 17 MHz (right); at about 40 kHz frequency difference the two signals are not locked distinguishable.*
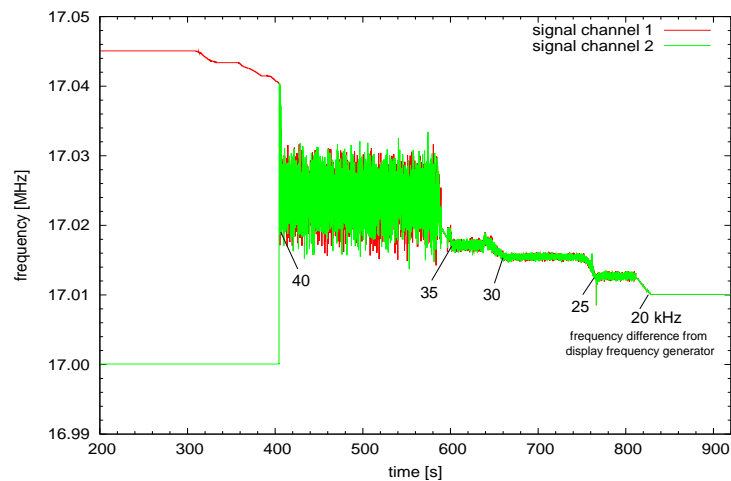
Figure 3.74: *Timeseries of the two phasemeter frequency outputs: at 20 kHz frequency difference (according to frequency generator display) the phasemeter locks on a frequency right in the middle of the two input frequencies.*

4 Modulated Input Signals

In the previous chapter the sensitivity of the phasemeter was determined by using clear, unmodulated input signals. An exception was presented in section 3.4.1.3, where the input was generated by an optical beat-note between two laser outputs. For a measurement using two free running lasers the differential phase noise increased up to 3 orders of magnitude with respect to a measurement using phase locked-lasers. The reason might be that the input signal was neither constant in frequency nor constant in amplitude.

In this chapter the influence of a frequency modulation (section 4.1) and an amplitude modulation (section 4.2) of the input signals on the differential phase noise of the phasemeter will be presented. Furthermore it will be shown (section 4.3) that for $7\,\mathrm{MHz}$ nominal input frequency the phasemeter is capable of detecting an externally imprinted phase modulation having an amplitude in the range of $10^{-7}\,\mathrm{rad}$.

4.1 Input Frequency Modulation

4.1.1 Initial Measurements

For the first measurement to investigate the behaviour of the phasemeter with respect to frequency modulated input signals the setup depicted in Figure 4.1 was used. It is basically the same setup already used to investigate the ADC time jitter noise. A frequency modulation was applied to the $7\,\mathrm{MHz}$ input signal with a modulation frequency of $f_\mathrm{m} = 2\,\mathrm{mHz}$ (period $T_\mathrm{m} = 500\,\mathrm{s}$) and a modulation depth of $D_\mathrm{m} = 500\,\mathrm{Hz}$. Figure 4.1 shows a graph of the frequency output of the frequency generator (actually these are measured data from one of the phasemeter channels, but the input is of course assumed to be identical). One can see that the carrier frequency is not exactly at $7\,\mathrm{MHz}$ but approximately $30\,\mathrm{Hz}$ above due to clock offsets between frequency generator and phasemeter. Since the modulation is common mode in both phasemeter channels after being split by the single OpAmp it should not be observable in the differential phase measurement of these two channels. The spectral density of this zero measurement is shown in Figure 4.2. It can clearly be seen that obviously this common mode frequency modulation of $2\,\mathrm{mHz}$ modulation frequency shows up in a peak at exactly that frequency in the phase noise after ADC jitter correction. This is a suprising result, but it turns out that it can be explained by assuming the input signals experiencing different time delays after splitting. It will be justified that it is actually not a delay of the input signals but a differential delay in the sampling process of the ADCs. The effect is the same as if the signals were time delayed before entering the ADC. This will be explained in detail in the following section.
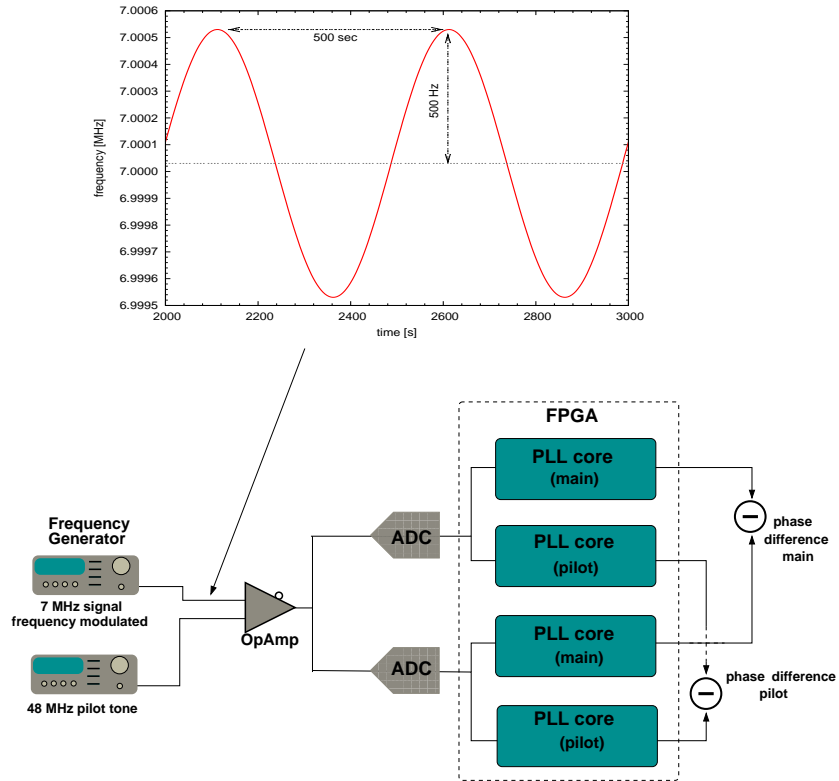
Figure 4.1: *Setup to investigate the effect of a frequency modulated input signal on the noise performance; modulation depth (500 Hz) and modulation period (500 s) are drawn in the graph of the timeseries of the measured signal.*
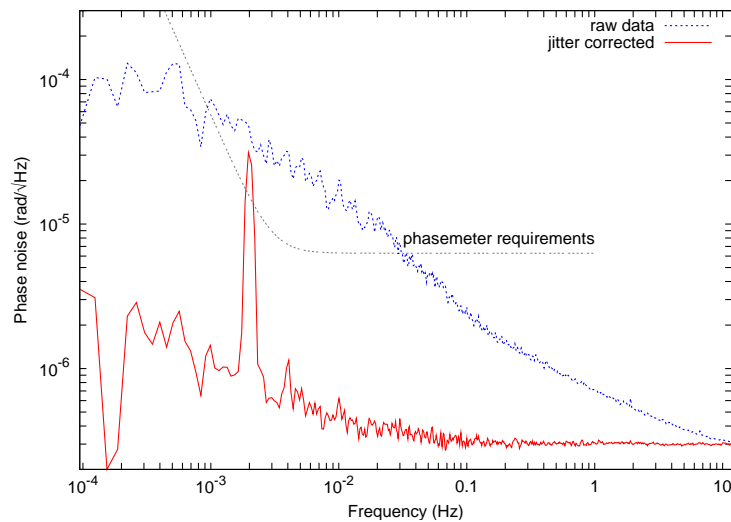
Figure 4.2: *Though it should cancel out by subtraction, a common mode peak at 2 mHz clearly emerges after ADC time jitter correction.*

4.1.2 Delay Correction

4.1.2.1 Origin of Common Mode Peak

One possibility to explain the appearance of the common mode peak in Figure 4.2 is to assume a differential time delay Δt between the two signals tracked by the PLLs. In Figure 4.3 the frequency of two time delayed, frequency modulated signals is shown. The black curve is the frequency difference of these two signals which oscillates around zero with the very same modulation frequency (this will be shown below in a mathematically precise way). This scheme can be used to analyse the peak emerging at $2\,\text{mHz}$ in Figure 4.2.

The PIR (frequency) output of the two phasemeter channels assuming this timeshift
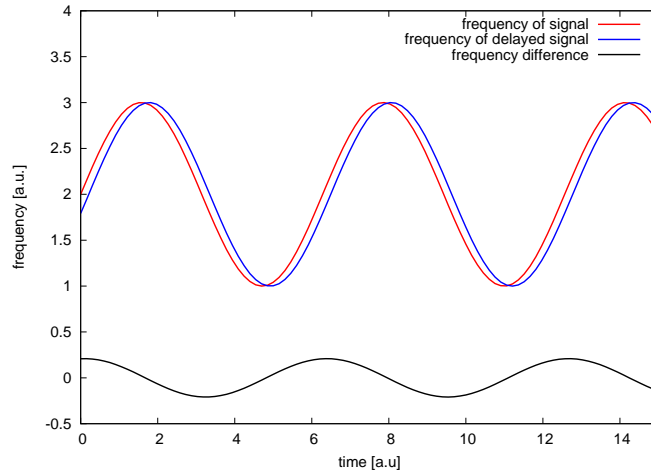
Figure 4.3: *Principle of the difference of two time delayed frequency modulated signals resulting in an frequency difference oscillating around zero*

Δt and no additional noise is given by

$$f_1 \;\; = \;\; f_\text{c} + D_\text{m} \cdot \sin(\omega_\text{m} t) \tag{4.1}$$

$$f_2 \;\; = \;\; f_\text{c} + D_\text{m} \cdot \sin(\omega_\text{m}(t + \Delta t)) \tag{4.2}$$

where f_c is the carrier frequency ($7\,\text{MHz}$), $\omega_\text{m}{=}2\pi f_\text{m}$ the modulation frequency ($f_\text{m}{=}2\,\text{mHz}$) and D_m the modulation depth ($500\,\text{Hz}$).
Subtracting f_2 from f_1 gives

$$\Delta f = D_\text{m} \cdot [\sin(\omega_\text{m} t) - \sin(\omega_\text{m}(t + \Delta t))] \tag{4.3}$$

evaluating the expression ([11]) yields

$$\Delta f = \underbrace{2 \cdot D_\text{m} \cdot \sin\left(\frac{\omega_\text{m}\Delta t}{2}\right)}_{\text{amplitude}} \cdot \underbrace{\cos\left(\omega_\text{m} t + \frac{\omega_\text{m}\Delta t}{2}\right)}_{\text{oscillation with } \omega_\text{m}}. \tag{4.4}$$

This is a sinusoidal oscillation with frequency ω_m and peak amplitude with respect to frequency

$$A_\text{freq} = 2 \cdot D_\text{m} \cdot \sin\left(\frac{\omega_\text{m}\Delta t}{2}\right). \tag{4.5}$$

Converting this into rms phase amplitude gives

$$A_{\varphi,\mathrm{rms}} = \frac{\sqrt{2} \cdot D_\mathrm{m}}{\omega_\mathrm{m}} \cdot \sin\left(\frac{\omega_\mathrm{m}\Delta t}{2}\right). \tag{4.6}$$

This peak appears in the spectral density shown in Figure 4.2 (actually it has to be divided by the effective noise bandwidth at $2\,\mathrm{mHz}$ Fourier frequency ([39])). Approximation of the sine by its argument ($\omega_\mathrm{m}\Delta t \ll 1$ is assumed) yields an expression for determining Δt:

$$\Delta t \approx \frac{\sqrt{2}}{D_\mathrm{m}} \cdot A_{\varphi,\mathrm{rms}}. \tag{4.7}$$

It should be possible to determine $A_{\varphi,\mathrm{rms}}$ by calculating the *spectrum* corresponding to the spectral density shown in Figure 4.2.

At this point it should be emphasised that for a signal with nearly constant frequency a time delay is indistinguishable from a constant phase shift. It will be shown in the remainder of this section that it is obviously a time delay that is the root cause for the $2\,\mathrm{mHz}$ peak by applying an input signal of varying frequency.

4.1.2.2 Delay correction principle

If the delay Δt between the two channels is known (it will be determined below), the frequency values can be delay corrected by linear interpolation as sketched in Figure 4.4. It is again a correction of the time series of the PIR (frequency) readout
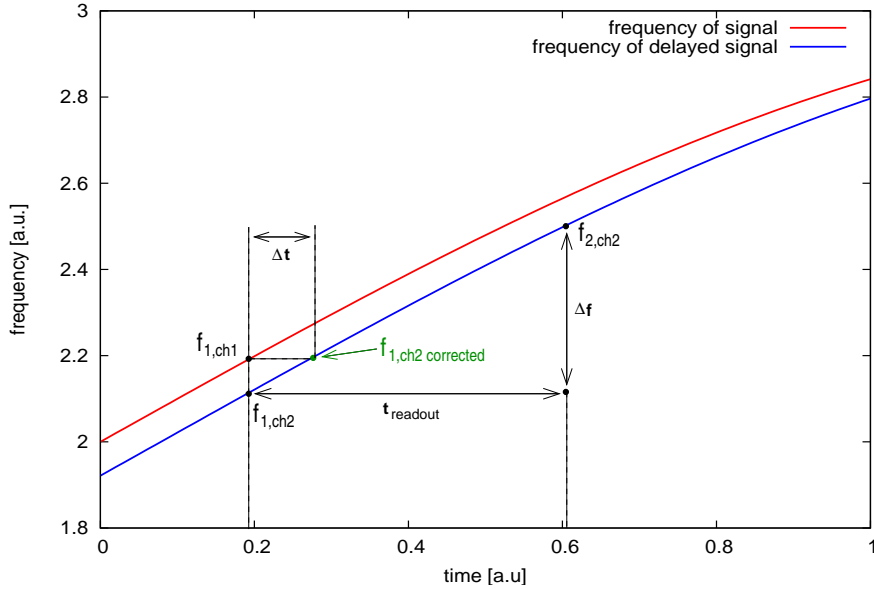
Figure 4.4: *Principle of linear interpolation: two adjacent frequency output values of the channel to be time delay corrected are used to obtain the corrected frequency value $f_{1,\mathrm{ch2\,corrected}}$. The input signals are assumed to be identical (they originate from one split signal) but for some reason time delayed. The correction scheme also works for signals that are not identical.*

and it is performed after time jitter correction. The time delay Δt is *not related to*

any ADC time jitter; it is assumed to be a constant time delay between the input signals. From Figure 4.4 it is easy to see how the time delay corrected frequency value $f_{1,\,\text{ch2 corrected}}$ is obtained:

$$f_{1,\,\text{ch2 corrected}} = f_{1,\,\text{ch2}} + \frac{\Delta f}{t_{\text{readout}}} \cdot \Delta t \tag{4.8}$$

where $\Delta f = f_{2,\,\text{ch2}} - f_{1,\,\text{ch2}}$ is the difference between two successive frequency values in the ouput sequence of channel 2, $t_{readout}$ is the readout period ($\approx 40\,\text{ms}$), $f_{1,\,\text{ch2}}$ the initial frequency value and Δt the constant time delay. This correction scheme can be successively applied to the whole time series.

It is assumed (and will be confirmed below) that a linear interpolation is sufficient for a proper correction since the change in frequency due to the low modulation frequency of $2\,\text{mHz}$ is small enough (the theoretical maximal frequency change during one readout cycle is about $0.25\,\text{Hz}$). For higher modulation frequencies (what is somehow already implied in Figure 4.4, since the frequency curves are only to a certain extend straight and parallel) this *linear* interpolation might better be replaced by more sophisticated methods.

4.1.2.3 Delay corrected Spectra

The first step to perform the time delay correction explained above is to determine the time delay Δt. It was already derived that Δt can be obtained by using the expression given in Equation (4.7).
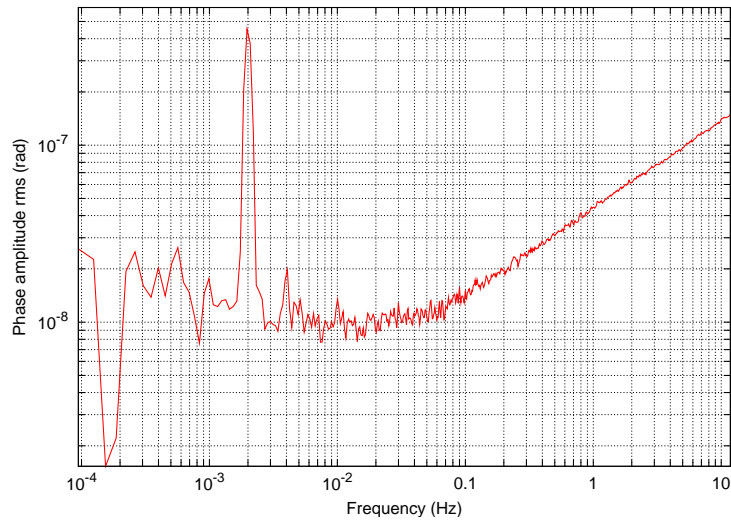
Figure 4.5: *Spectrum of the differential phase measurement yields a phase amplitude of approximately $4.5 \cdot 10^{-7}$ rad*

In Figure 4.5 the spectrum corresponding to the spectral density (Figure 4.2) is shown. The rms phase amplitude of the $2\,\text{mHz}$ peak has a height of approximately $4.5 \cdot 10^{-7}\,\text{rad}$. According to Equation (4.7) with $D_{\text{m}} = 500 \cdot 2\pi\,\text{rad/s}$ the corresponding time delay is approximately $0.2\,\text{ns}$, which was used to obtain the time delay
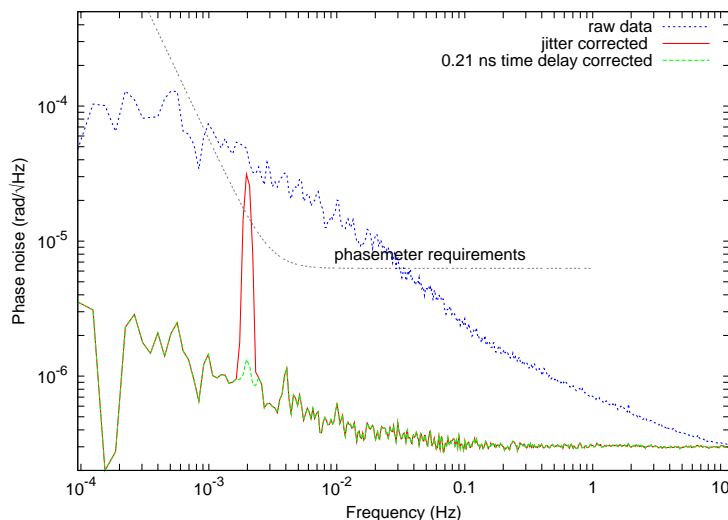
Figure 4.6: *The 2 mHz common mode peak (red solid line) has completely vanished (green dashed curve) after delay correcting the corresponding time series*

corrected timeseries. Afterwards a spectral density was calculated. Using the trial and error method a value of 0.21 ns was found to yield the best correction results. The corresponding noise curves can be seen in Figure 4.6. The 2 mHz peak has completely disappeared (green, dashed curve), while the noise floor remains unaffected by the time delay correction.

4.1.2.4 ADC Clock Time Delay

If the delay between the two channels equivalent to $\Delta t = 0.21$ ns is really a time delay (not a phase delay) common for all input frequencies, there should be a linear relation between frequency f and phase difference $\Delta\varphi$:

$$\Delta\varphi = 2\pi f \cdot \Delta t \qquad (4.9)$$

The setup depicted in Figure 4.7 was chosen to investigate this frequency dependence. The phase difference between two input channels can be measured also by using the PA (phase) output of the PLLs. This principle was used here as can be seen in Figure 4.7. The contents of the PA registers were directly subtracted on the FPGA chip to get as output the phase difference $\Delta\varphi$ of the two phasemeter channels. Simultaneously the frequency was read out from the PI register. A frequency modulation of the input signal was chosen such that the input frequency changes sinusoidally between 3 and 19 MHz (11 MHz nominal frequency, 8 MHz modulation depth) with a modulation frequency of 2 mHz.

The result of this measurement can be seen in the left graph of Figure 4.8. On this scale there is a linear dependence between frequency and phase difference. This was expected according to Equation 4.9. Since the frequency f of the signal is known, this phase difference can be converted into an equivalent differential time delay:

$$\Delta t = \frac{\Delta\varphi}{2\pi f} \qquad (4.10)$$
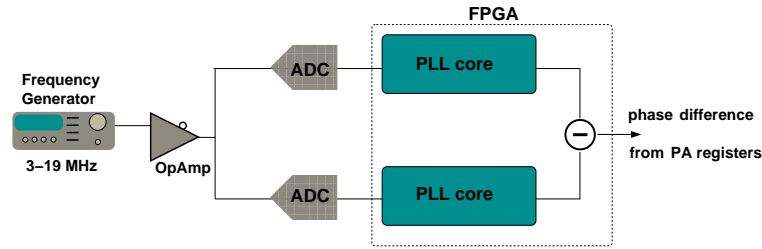
Figure 4.7: *Phase difference of two input signal was obtained by subtracting the binary values of the PA registers onboard the FPGA*

The result of this conversion can be seen in the right graph of Figure 4.8. From this graph 3 observations can be made:

- The phase equivalent time delay is for all frequencies between 3 and 19 MHz in the order of 0.21 ns.

- There is a tiny (equivalent to picoseconds) but clear frequency dependend structure on it.

- The shape of this structure does not change over time, but its attitude does.
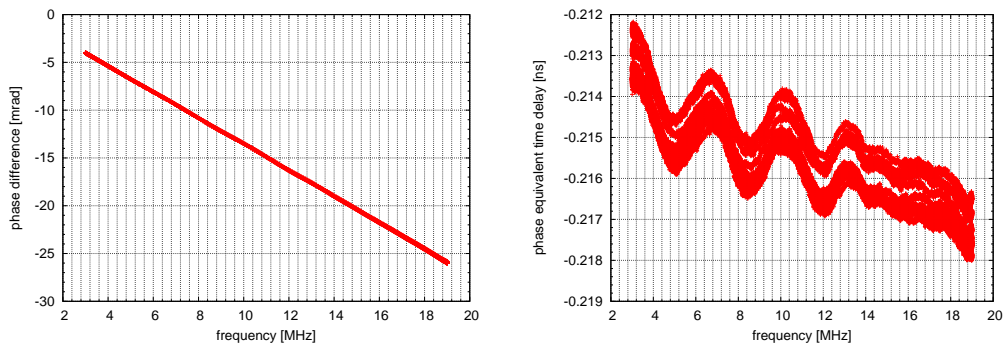
Figure 4.8: *Conversion from phase difference (left) into time delay (right) yields a value about 0.21 ns independent of input frequency*

This behaviour can be explained as a combination of constant time delay and some additional phase shift due to the analog front end. There is obviously a time delay of 0.21 ns between the two input signals when they enter the PLLs. For copper lines (e.g., on a PCB board) 0.21 ns signal travelling time corresponds to approximately 4 cm in electrical pathlength (assuming 2/3 of the vacuum speed of light for the signal velocity). This length can be found on the phasemeter board as the difference between the electrical lines of the clock driving the sampling process of the two ADCs (see Figure 4.9). This most probably causes the time delay. This delay is of course independent of the input signal meaning that the frequency dependent tiny structure in Figure 4.8 (right graph) is probably caused by the difference in electrical signal paths after being split behind the OpAmps. Assuming the 0.21 ns delay common for
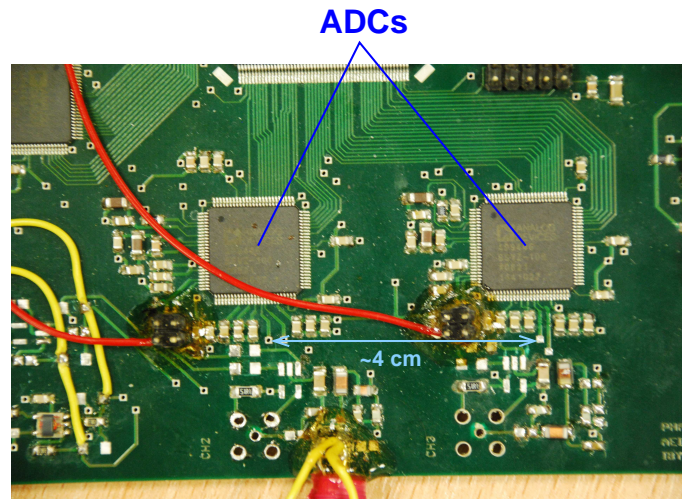
Figure 4.9: *The difference between the clock lines on the phasemeter board is responsible for the 0.21 ns time delay between the two channels.*
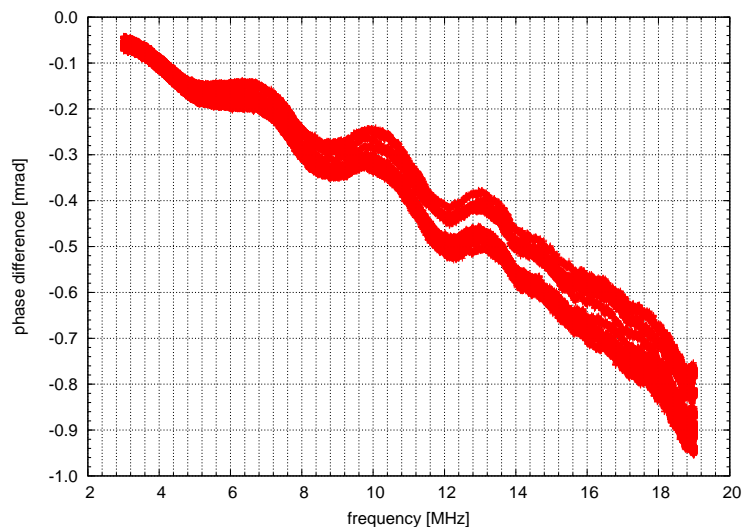
Figure 4.10: *After subtracting the phase shift caused by time delay the phase difference due to electric connection between OpAmp and ADCs remains.*

all input frequencies and subtracting the corresponding phase difference according to

$$\Delta\varphi = 2\pi\Delta t \cdot f \tag{4.11}$$

from the values obtained from the left graph of Figure 4.8 gives the graph shown in Figure 4.10. This might be the phase difference introduced by the analog front end, i.e., by the connection between OpAmp and ADCs.

4.1.3 Analog Front End Phase Delay

The previous measurement of the phase delay was performed on an input signal that was split right before the ADCs. The setup used to determine the influence of the
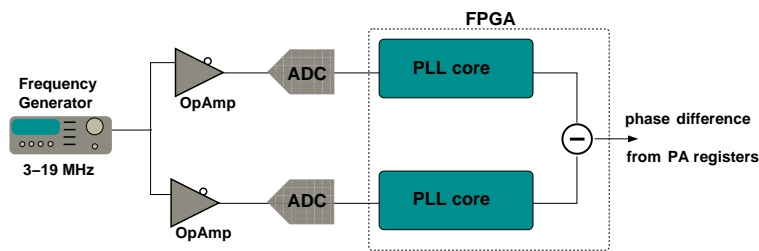
Figure 4.11: *Setup to investigate phase delay including the OpAmps as additional potential delay source, the readout scheme is the same as in Figure 4.7.*
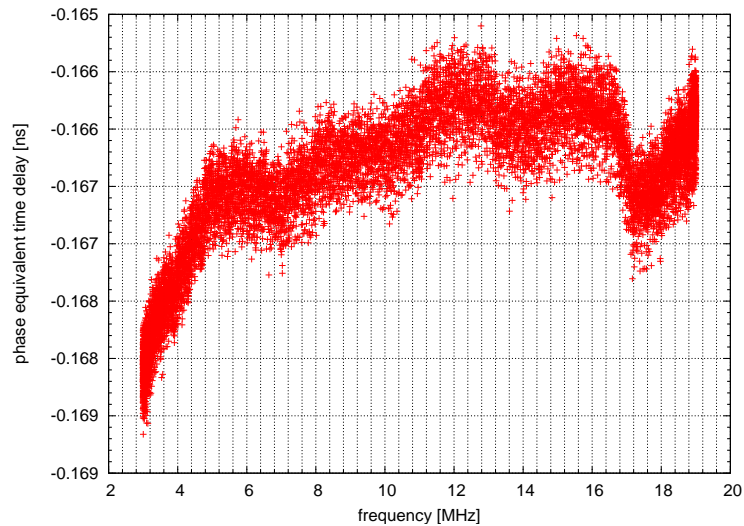
Figure 4.12: *The phase noise equivalent time delay for 2 OpAmps shows a completely different behaviour than the one for a measurement using only one OpAmp. The variation of the delay is for both cases (cf. Figure 4.8) in the order of a few picoseconds.*

analog front end (i.e., the OpAmps) on the differential phase delay is depicted in Figure 4.11. It is basically the same setup as for the measurement depicted in Figure 4.7 but with two OpAmps comprising the analog front end. Again the input signal

from the generator was chosen such that it sweeps sinusoidally in frequency between 3 and 19 MHz with a modulation frequency of 2 mHz. The phase difference between the input channels was taken directly onboard the FPGA and read out via EPP. Converting the phase difference of the two input channels into equivalent time delay yielded the results depicted in Figure 4.12. It can be seen that the average delay is not at 0.21 ns as for the measurement using one OpAmp but at 0.16 ns. Furthermore the shape of the of the tiny structure (picosecond-range) is also different from that shown in the right graph of Figure 4.8. The difference in average delay can be explained by the front end (the OpAmps) introducing a differential time or phase delay having opposite sign with respect to that introduced by the ADC clock lines and hence partly compensating for it.

4.2 Input Amplitude Modulation

In this section it will be shown that an amplitude modulation has even more drastic influence on the differential phase noise of the phasemeter than the frequency modulation has. The reason for this is not yet understood.

4.2.1 Initial experimental Results

To investigate the effects of an amplitude modulated input signal on the differential phase noise the setup depicted in Figure 4.13 was used. It is basically the same setup as used for the frequency modulated input signals. The difference is that the input signal was constant in frequency (7 MHz) and modulated in amplitude (modulation frequency was 2 mHz and modulation depth 10 % of the nominal amplitude). The amplitude of the two input signals could be determined by recording the I-readout of the PLLs. A graphical presentation of the measured input amplitude can also be seen in Figure 4.13. Simultaneously the PIR readout was used to reconstruct the differential phase of the two signals. The result of the differential phase measurement are shown in Figure 4.14 (time series of phase difference) and Figure 4.15 (differential phase noise). Both show the drastic influence of the amplitude modulation on the phase noise. The peak at the modulation frequency of 2 mHz is observable even in the spectral density of the raw data. In contrast to the phase noise of frequency modulated input signals there appear peaks at each harmonic of 2 mHz up to nearly 100 mHz Fourier frequency. The first 6 of them are even above the requirements. It was tried to remove these peaks by performing a time delay correction with several different delays Δt without any success. None of the peaks could be attenuated.

Figure 4.16 shows the time series of the amplitude difference between the two channels (left graph) and the corresponding linear spectral density (right graph). The time series shows fluctuations in the amplitude difference in the range of 0.6 mV. The differential amplitude noise (right graph) shows a common mode peak at 2 mHz, but also two tiny peaks at 4 and 6 mHz are visible. This impact of an amplitude modulated input signal on the differential phase noise is not yet understood and has to be investigated. A possible explanation for the peaks appearing in the phase noise shown in Figure 4.15 could be that the amplitude difference of the two input channels affects the gain of the PLL. The open loop gain $G(s)$ depends linearly on the input amplitude meaning that $G(s)$ changes in the same manner as the amplitude does.
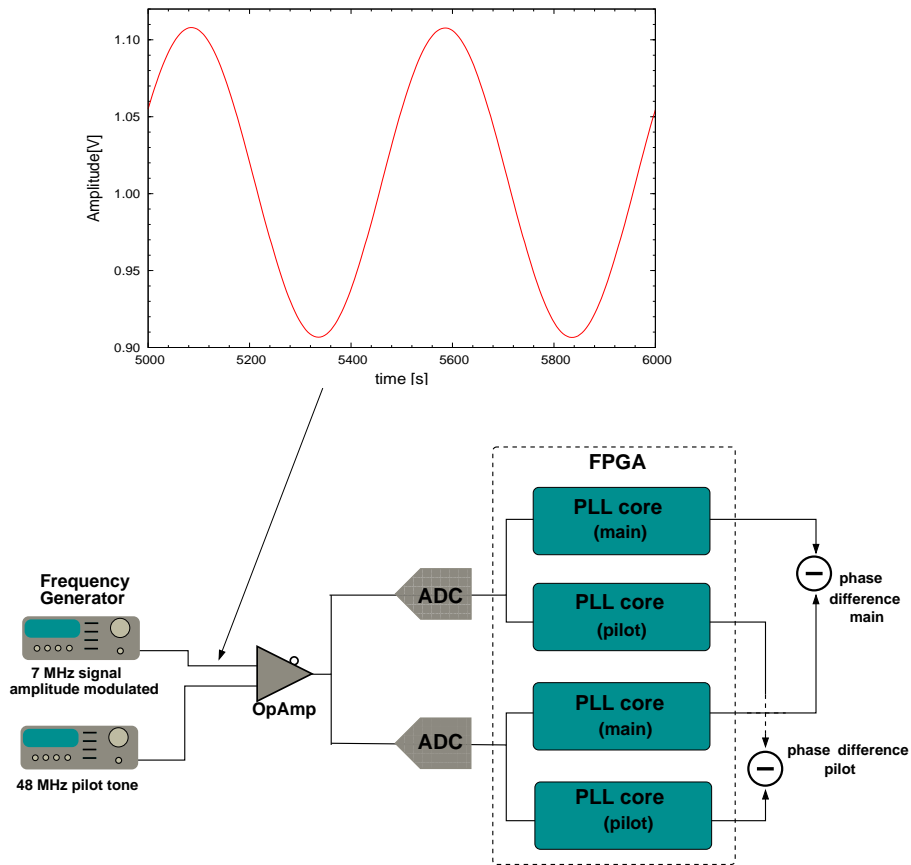
Figure 4.13: *Setup for investigating the influence of a common mode amplitude modulation on the phasemeter sensitivity*
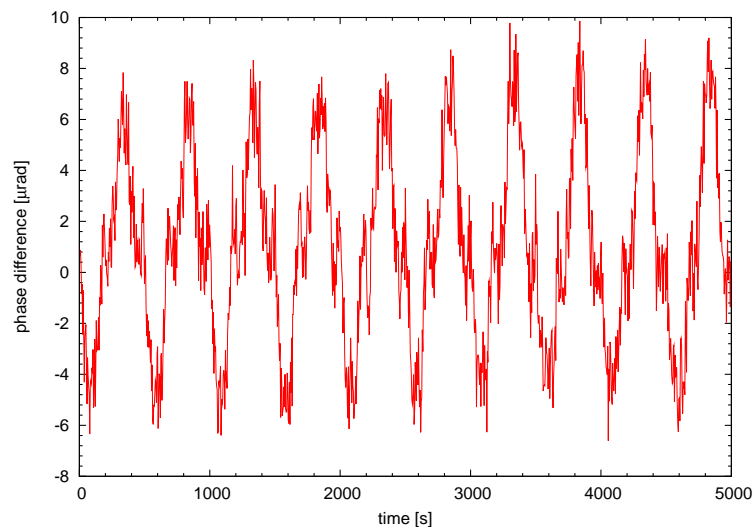
Figure 4.14: *Phase difference of the two amplitude modulated signals shows triangular-like oscillation.*
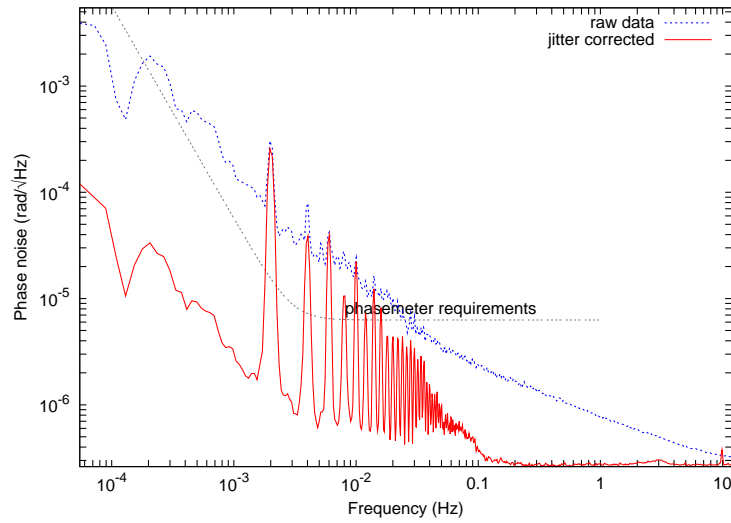
Figure 4.15: *Spectral density for amplitude modulated input signals shows peaks at 2 mHz and its harmonics.*

Since the detected phase is related to the real (incoming) phase like

$$\frac{\varphi_{\text{det}}(s)}{\varphi_{\text{in}}(s)} = \frac{G(s)}{1 + G(s)} \tag{4.12}$$

amplitude noise couples nonlinear into the phase measurement. Another reason might be nonlinear behaviour of the OpAmps.
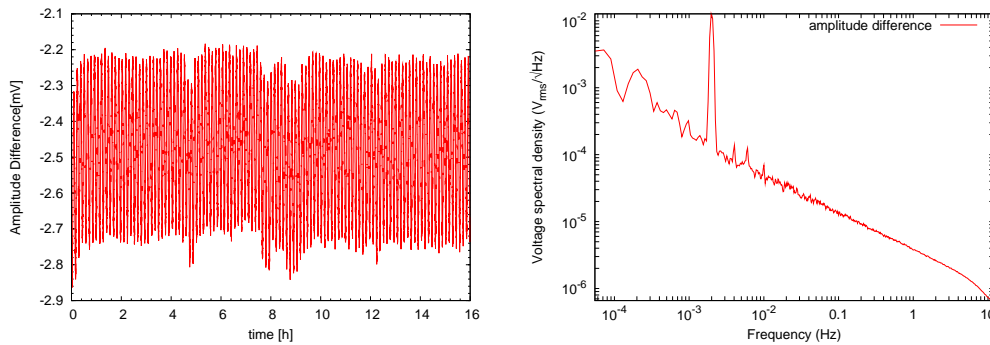
Figure 4.16: *Differential amplitude noise has main peak at 2 mHz but also tiny peaks at 4 and 6 mHz.*

4.2.2 Frequency Drift coupled Amplitude Modulation

4.2.2.1 Frequency dependence of Input Amplitude

From the previous subsection it is obvious that a modulation of the input amplitude has severe impact on the phase noise of the phasemeter. This might not be caused by the modulation itself but by the *difference* between the amplitude variations of the two input signals. To investigate if this difference in input amplitude shows any
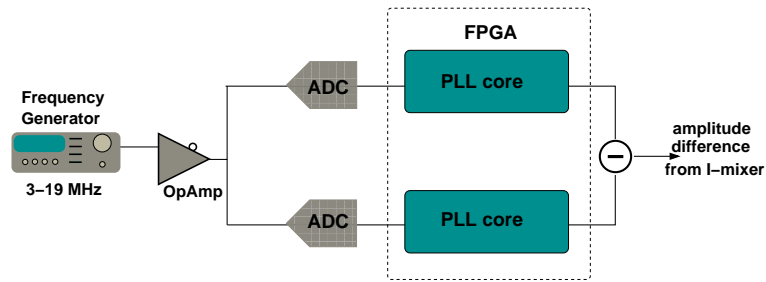
Figure 4.17: *Setup for measuring the frequency dependence of input amplitude differences: the I-mixer and the PIR readout deliver the needed data. This setup was extended to also perform a measurement with two OpAmps, the measuring principle remains the same.*

dependence on the frequency of the input signal the setup depicted in Figure 4.17 was chosen. The frequency of the input signal was sinusoidally modulated (modulation frequency 2 mHz, modulation depth 8 MHz, nominal frequency 11 MHz). The output amplitude of the generator was kept constant at $2\,V_{pp}$. From the I-mixer readout the amplitudes detected at the input of the PLLs were measured. Simultaneously the PIRs were read out to determine the current frequency. The results of this measurements are shown in Figure 4.18 for a measurement using one OpAmp (left graph) and two OpAmps (right graph). It can clearly be seen that there is a dependence of the input amplitude difference on the frequency of the input signal. The variations of the amplitude differences are in both cases (one OpAmp and two OpAmps) in the range of a few mV. The dynamic range of these variations is more significant for signals with frequency higher than approximately 10 MHz.
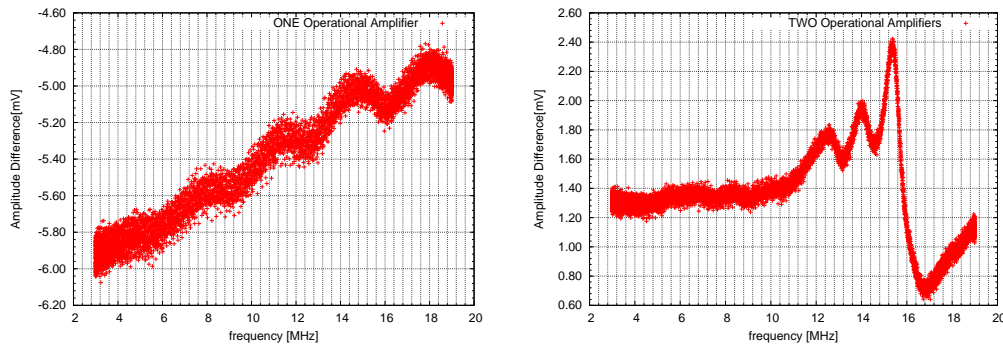
Figure 4.18: *Both measurements (one and two OpAmp analog front end) clearly show a dependence of the differential amplitude on the frequency of the input signal.*

4.2.2.2 Frequency modulated 17 MHz Input

Since the effect of an amplitude modulated input signal has significant influence on the differential phase noise of the phasemeter (see Figure 4.15) similar effects might occur if an amplitude modulation is induced by a varying frequency of the input signal. To test if the phase noise of a frequency modulated input signal with higher frequency (> 10 MHz) is as excellent as for the measurement using a frequency mod-

ulated 7 MHz signal (see, e.g., Figure 4.6) a measurement was performed using a 17 MHz input. The setup is depicted in Figure 4.19. The modulation frequency was 2 mHz and the modulation depth was 500 Hz. The I-mixer output was recorded to get the information about the input signals' amplitude. Simultaneously the frequency was obtained from the PIRs.

The spectral estimate for the phase difference is shown in Figure 4.20. After jitter correction there appears the 2 mHz common mode peak just as for the measurement using a 7 MHz input signal. Additionally there appear peaks at the harmonics of the modulation frequency (2 mHz) just as for the amplitude modulated input (cf. Figure 4.15) but with peak heights below the requirements. The common mode peak can be removed by applying a time delay correction of 0.18 ns (which is a surprising result since one would expect a time delay of 0.21 ns according to subsection 4.1.2) but the harmonic peaks remain unaffected by this correction scheme.

In Figure 4.21 the spectral estimates for the amplitudes (the I-mixer output) are
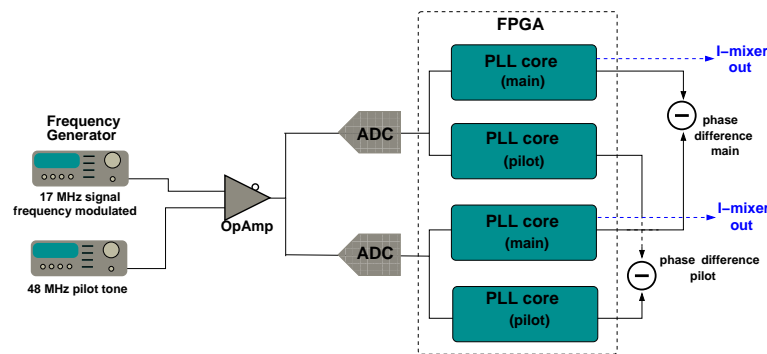
Figure 4.19: *Setup for investigating the phase noise for a frequency modulated 17 MHz input signal using one OpAmp*

shown. The spectral density of the amplitude of one single channel shows a noise behaviour similar to that of the jitter corrected phase difference. In the differential amplitude noise there appear no peaks anymore. It might be that they perfectly cancel out by subtraction but it might also be possible that there are still peaks in difference which are covered by ADC time jitter noise (that also corrupts the amplitude measurement). The peaks appearing in the spectrum of one single channel could also be caused by frequency dependent amplitude fluctuations of the generator output. This would have in principle the same effect as the amplitude modulation explained in section 4.2 but the generators amplitude output does not differ by 100 mV within 1 kHz frequency deviation for an output of 1 V. It is unlikely that the amplitude differences shown in Figure 4.18 are responsible for the excess noise (Figure 4.20) since a deviation of 500 Hz (modulation frequency) would cause a differential amplitude deviation 3 orders of magnitude below the differential fluctuations between the amplitude modulated input signals shown in the left graph of Figure 4.16. As a conclusion one can say that it is possible that a frequency modulation of the input signal with frequency 17 MHz is somehow related to an amplitude modulation causing peaks in the phase noise. Whether these amplitude fluctuations are caused by the generator or by the electronics of the phasemeter needs to be investigated.
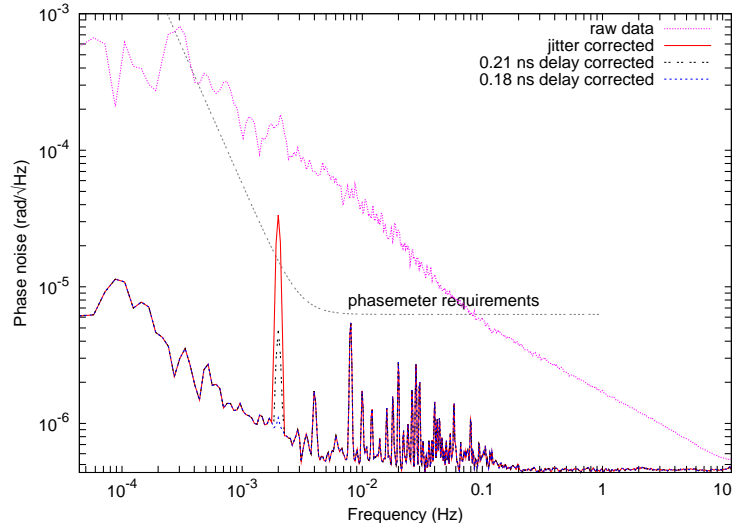
Figure 4.20: *The common mode peak at the modulation frequency can be removed by time delaying while the other peaks remain unaffected.*
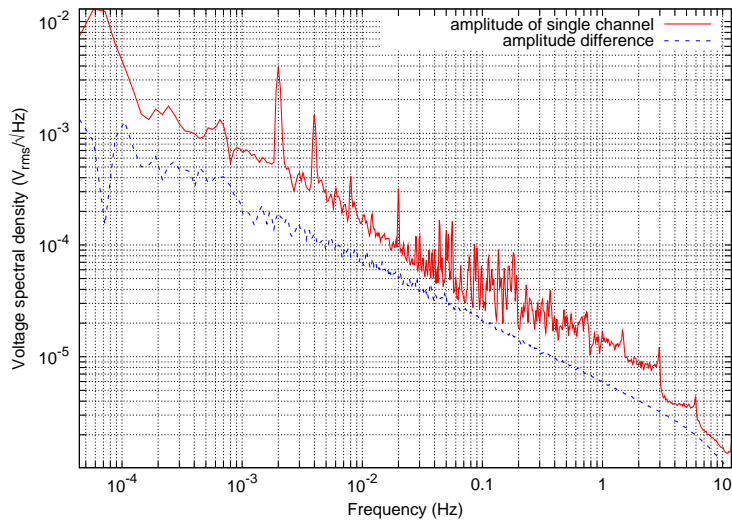
Figure 4.21: *The amplitude noise of one single channel shows behaviour comparable to that of the differential phase noise (Figure 4.20) while the differential amplitude noise is rather smooth.*

4.3 LISA-like Modulation

In this section it will be confirmed that the phasemeter is capable of detecting a phase modulation signal imprinted externally on the RF signal of *one* of two input channels to mimic a gravitational wave signal (subsection 4.3.2). Furthermore it will be shown that in principle such a detection is possible in the presence of a common mode frequency modulation taking the expected Doppler drift into account (subsection 4.3.3). In both cases the information about this asymmetric phase modulation will not be corrupted by any correction scheme applied.

4.3.1 Principle of Measurement
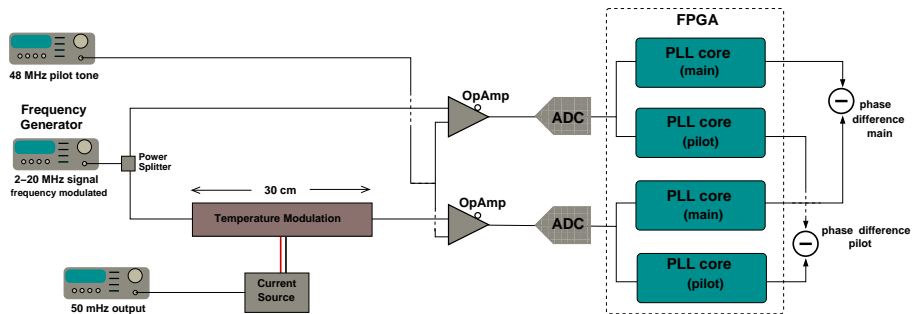
Figure 4.22: *The setup for LISA-like signal detection uses periodically heating of one coaxial cable to mimic a gravitational wave signal in one 'arm' of the detector.*
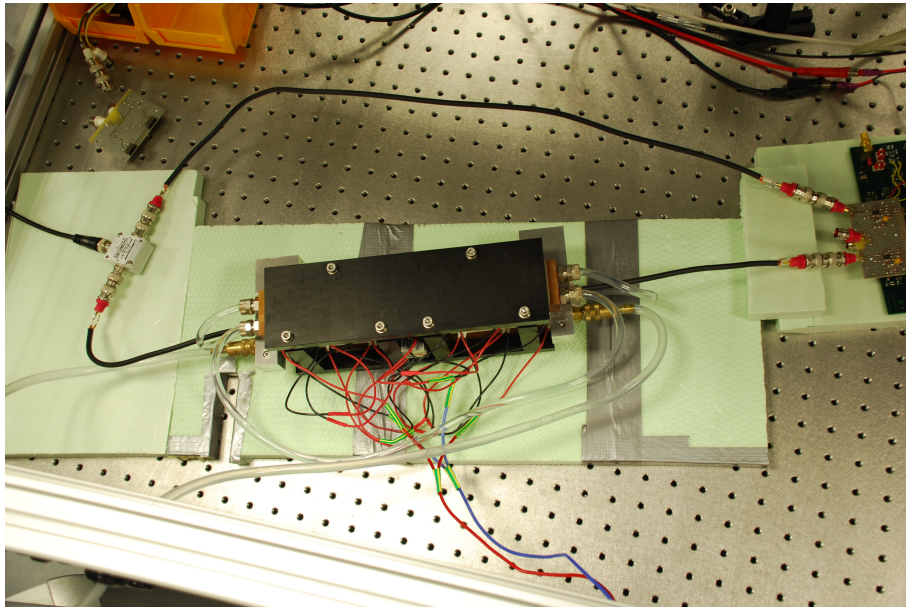
Figure 4.23: *Photograph of the LISA signal detection setup; the pilot tone is not yet connected to the phasemeter.*

For each of the measurements mentioned above the setup sketched in Figure 4.22 was used. Figure 4.23 shows a photograph of this setup. It is basically a differential measurement between two input channels using two OpAmps as analog front end. Compared to the measurements presented in this thesis so far there are two main differences. The first difference is that after splitting the signal of interest there are two cables of approximately 70 cm length each the two signals have to pass before being injected into the phasemeter's analog front end. These coaxial cables have been proven to have an excellent phase stability meaning that the usual environmental temperature fluctuations present in the laboratory do not induce significant phase changes on the signals passing the cables. This would corrupt the whole measurement. The second difference to measurements performed before is the possibility of imprinting a phase modulation on one of the split signals by using the temperature modulation block (see Figure 4.22 and Figure 4.23) to periodically heat the cables. It consists of Peltier elements driven by a current source delivering a (sinusoidal) current in the range of several Ampere. The frequency of this modulation is adjustable by means of the frequency generator. A 48 MHz signal is used as pilot tone for ADC jitter correction.

4.3.2 Asymmetric Phase Modulation

The first measurement was intended to show that a phase modulation of known frequency imprinted on the signal of one input channel by means of the temperature modulation can be detected in a differential phase measurement between the two input channels. The frequency output of the generator was kept constant at 7 MHz (the frequency modulation sketched in Figure 4.22 was **not yet** applied). Two measurements with 5 mHz and 50 mHz temperature modulation frequency were carried out. The results of these measurements can be seen in Figure 4.24. The peaks
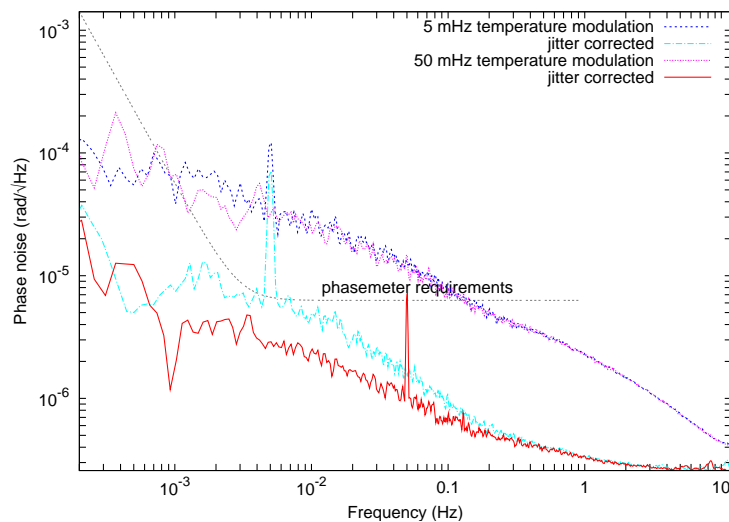
Figure 4.24: *The two different temperature modulations show up as peaks in the differential phase noise as expected.*

due to the modulation clearly appear at the corresponding frequencies (5 mHz and 50 mHz) in the differential phase noise. For the 50 mHz modulation the peak does not appear before the jitter correction is applied. The noise floor of the measurement with 5 mHz modulation frequency is for Fourier frequencies below 200 mHz worse than the one of the measurement using a 50 mHz modulation but it still meets the requirements. The decrease in the peak height of the 5 mHz modulation signal after jitter correction is most probably caused by the corresponding decrease in the background noise floor.

4.3.3 Phase Modulation in Presence of Frequency Drift

For measuring the asymmetric phase modulation in the presence of a LISA-like frequency drift the setup depicted in Figure 4.22 was used. The frequency of the input signal $f_{\mathrm{in}} = 7$ MHz was frequency modulated with a modulation depth (D) of 500 Hz and a modulation frequency (f_{mod}) of 2 mHz. For a frequency modulated signal having a frequency of

$$f(t) = f_{\mathrm{in}} + D \cdot \sin(2\pi \cdot f_{\mathrm{m}} \cdot t) \qquad (4.13)$$

the frequency change with respect to time is

$$\dot{f}(t) = 2\pi \cdot f_{\mathrm{m}} \cdot D \cdot \cos(2\pi \cdot f_{\mathrm{m}} \cdot t) \qquad (4.14)$$

having a maximum slope of 2π Hz/s for the values given above. This is a faster change than the maximum Doppler drift of 4 Hz/s expected during the LISA mission.

The temperature modulation was set to 50 mHz.

The results of this measurements can be seen in Figure 4.25. After jitter correc-
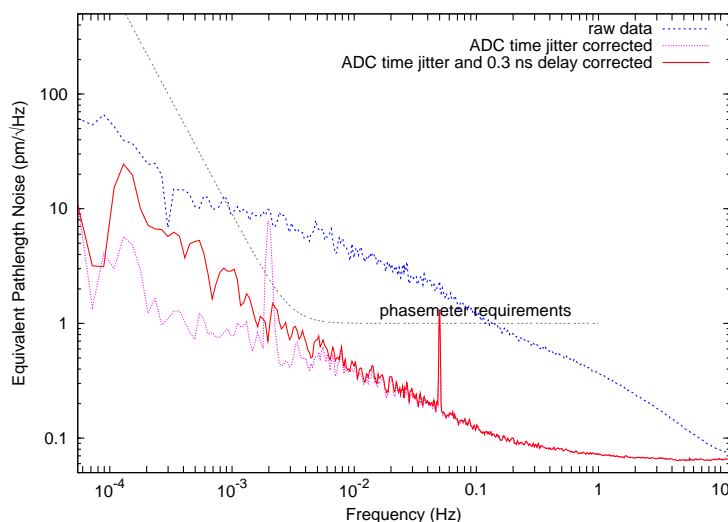
Figure 4.25: *The phase modulation peak emerging after ADC jitter correction remains unaffected by the removal of the common mode frequency modulation peak; the increase in the noise floor is caused by truncation errors of the stored data.*
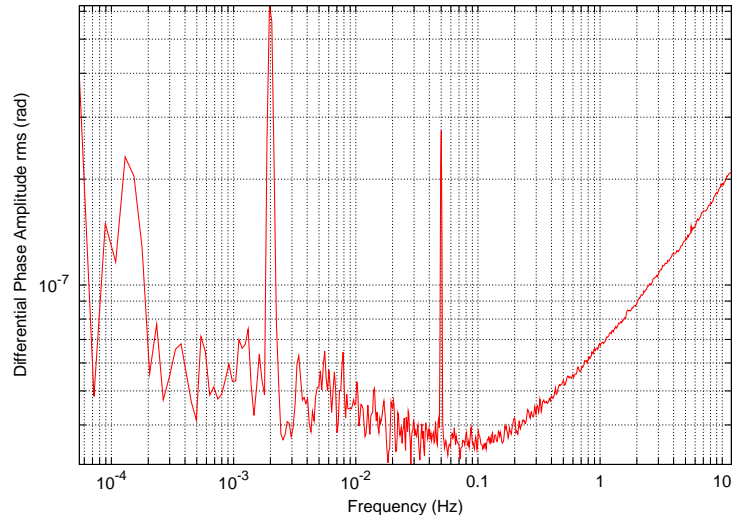
Figure 4.26: *The spectrum of the phase difference of the two input signals yields a value below $3 \cdot 10^{-7}$ rad rms phase amplitude of the phase modulation signal.*

tion both the phase modulation peak and the common mode frequency modulation peak emerge in the spectral density. The common mode peak can be removed by applying a usual time delay correction of 0.3 ns. The phase modulation peak is not affected by this correction. Unfortunately, there is an increase in phase noise below 6 mHz Fourier frequency after applying this correction scheme. This was caused by an insufficient accuracy in the stored data used for the time delay correction.

From Figure 4.26 showing the *spectrum* corresponding to the spectral density shown in Figure 4.25 it can be seen that the phase modulation has an rms amplitude below $3 \cdot 10^{-7}$ rad.

The measurements presented in this section clearly show that *in principle* the phasemeter is capable to detect a tiny phase modulation ($3 \cdot 10^{-7}$ rad rms) imprinted on a LISA-like frequency drifting input signal.

5 Nd:YAG NPRO Frequency Noise

In this section a technique for measuring the frequency noise between 100 kHz and 20 MHz Fourier frequency of a free running Nd:YAG NPRO laser ([41],[42],[43]) (Innolight Mephisto NE spezial) and the corresponding experimental results are presented. This type of laser is baselined to serve as the a master laser onboard LISA. The results of the measurements presented are amongst others important for the development of a digital signal simulator within the framework of [17]. This simulator should be able to generate the signals expected as input for the LISA interferometry including all types of noise. To the authors best knowledge only frequency noise measurements up to 100 kHz Fourier frequency have been performed for this type of laser to date ([44],[45]).

5.1 Balanced Detection Principle

The technique used to measure the high frequency noise of the lasers is based on a so-called *balanced detection scheme*. A schematic of the whole measurement is
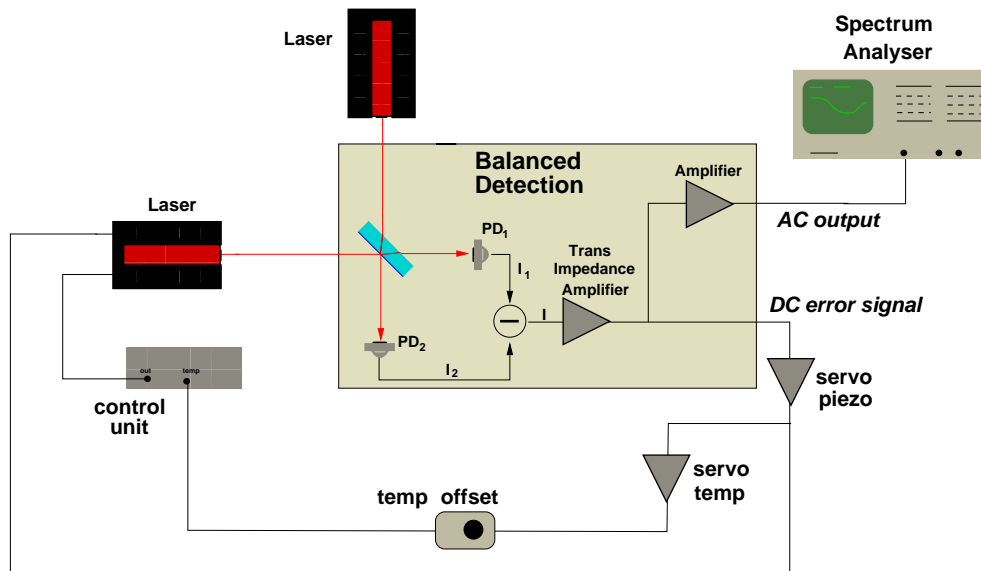
Figure 5.1: *Balanced Detection Principle: the frequency of the noise to be measured is not suppressed by the control loop that keeps the beat-note frequency at zero. The setup is adjusted such that the DC parts of the two photocurrents I_1 and I_2 cancel by subtraction to avoid a coupling of amplitude noise into phase noise. The resulting current I is said to be balanced.*

depicted in Figure 5.1. The principle of the measurement is to keep the beat-note

frequency between the two lasers at zero (DC-lock) by means of a control loop having a unity gain frequency of approximately $10\,\mathrm{kHz}$ and evaluating the remaining phase noise above $100\,\mathrm{kHz}$ Fourier frequency which is not suppressed by the control loop. (This can easily be converted into frequency noise.)

The photodetectors PD_1 and PD_2 detecting the beat-note signal of the interference deliver photocurrents of

$$I_1 \quad \propto \quad \frac{1}{2}E_1{}^2 + \frac{1}{2}E_2{}^2 + E_1 E_2 \sin(\Delta\omega t + \Delta\varphi) \tag{5.1}$$

$$I_2 \quad \propto \quad \frac{1}{2}E_1{}^2 + \frac{1}{2}E_2{}^2 - E_1 E_2 \sin(\Delta\omega t + \Delta\varphi) \tag{5.2}$$

where E_1 and E_2 are the light field amplitudes and $\Delta\omega = \omega_1 - \omega_2$ is the beat-note frequency between the two lasers. The phase difference $\Delta\varphi$ contains the information about the noise. Subtraction of these currents gives an input current $I = I_1 - I_2$ of the transimpedance amplifier of

$$I \quad \propto \quad 2\,E_1 E_2 \sin(\Delta\omega t + \Delta\varphi) \tag{5.3}$$

$$= \quad 2\,E_1 E_2 \sin(\Delta\varphi) \tag{5.4}$$

since the loop keeps $\Delta\omega$ at zero. The DC parts of the interference signals are assumed to be identical. This principle of eliminating the DC parts of the currents is called *balanced detection*. This balancing is necessary for the amplitude noise not to couple into the phase noise measurement. For small $\Delta\varphi$ the resulting changes in the photocurrent I depends to first order on $\Delta\varphi$:

$$I \propto 2\,E_1 E_2 \Delta\varphi. \tag{5.5}$$

This yields a voltage output of the transimpedance amplifier of $U_{\mathrm{ti}} = \alpha \cdot \Delta\varphi$ where α is the proportionality factor at DC. The remaining high frequency noise is amplified in the AC-readout path and analysed by means of the spectrum analyser (R&S FSL 18).

5.2 Experimental Results

The raw data obtained by the measurement principle explained above are shown in Figure 5.2. The curves present the measured data in dBm of the AC output of one actual measurement and the dark noise of the detector without light on the photodiodes (also at AC output). After converting the measured voltage into frequency noise, taking into account the dark noise of the detector, the transfer function of the AC path, the spectrum analyser's bandwidth of the stored data and the scaling factor to DC, the noise curves shown in Figure 5.3 were obtained. They present the results for measurements performed with and without noise eater, an active feedback loop for suppressing the relaxation noise ([46]). Above $200\,\mathrm{kHz}$ Fourier frequency the curves do not show the $1/f$ frequency noise behaviour typical for NPROs at lower frequencies. It looks more like some structure upon some lowest limit being at approximately $0.2\,\mathrm{Hz}/\sqrt{\mathrm{Hz}}$ for Fourier frequencies above $200\,\mathrm{kHz}$. The effect of the noise eater can clearly be seen as the broad peak with maximum height
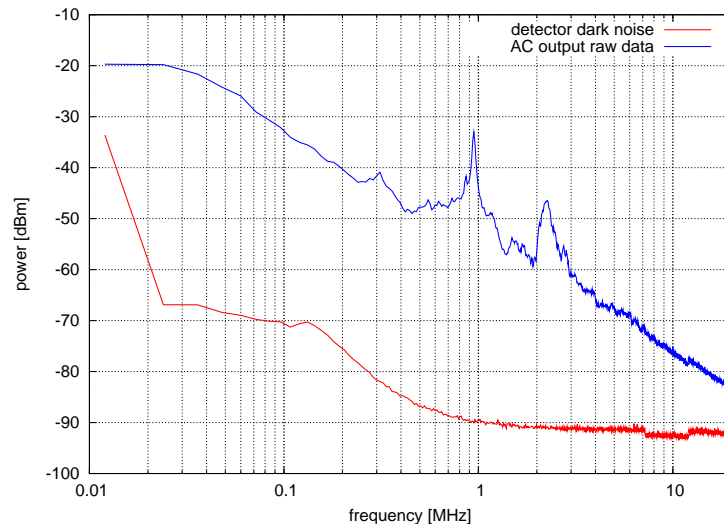
Figure 5.2: *The raw data of the AC readout are given in dBm (which is basically a voltage value) and have to be converted into the corresponding rms phase amplitude. Also the dark noise of the detector was taken into account.*
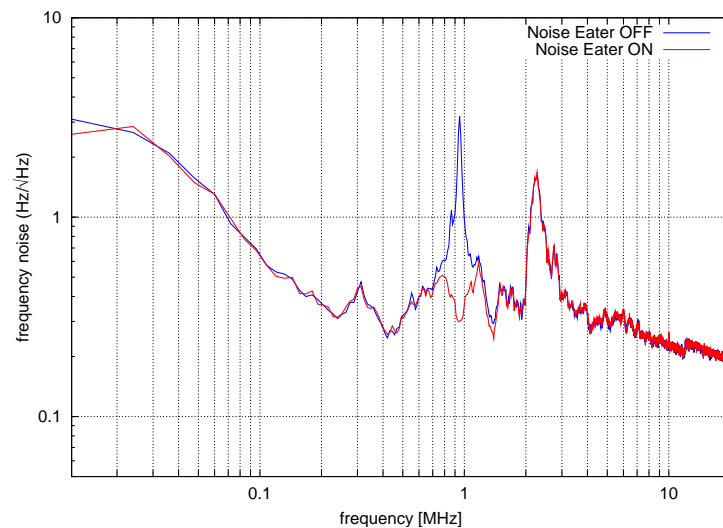
Figure 5.3: *The measured frequency noise of a free running NPRO above 100 kHz does not show a smooth behaviour. The impact of the relaxation oscillation suppression by means of the noise eater is obvious. The peak at 2.2 MHz remains unaffected.*

111

at about 900 kHz is removed. The peak at about 2.2 MHz remains unaffected by the noise eater function. Its origin is not clear yet, as it is not clear for the noise structure between 200 kHz and 2 MHz. Further investigations need to be performed to clarify this.

Figure 5.4 shows the result of this balanced detection measurement (blue curve) and the results presented in [44] (red curve). Both curves show a limiting behaviour that matches *in shape* the assumption of the frequency noise of a free running NPRO according to [17] (black solid curve). Unfortunately, both curves are by a factor up to 5 higher than expected. Obviously, this assumption is too optimistic. The increase in frequency noise of the blue curve below 200 kHz do not match the values of the red curve that shows the typical $1/f$ behaviour. The reason for this is not clear.
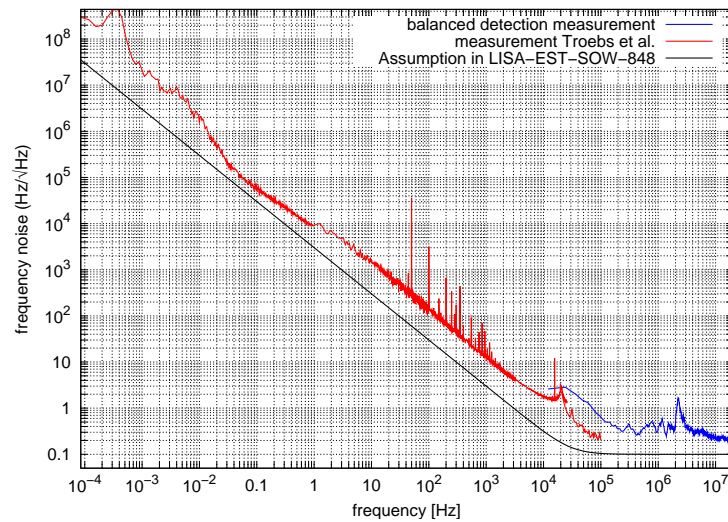
Figure 5.4: *The frequency noise of a free running Nd:YAG NPRO presented in [44] and in this thesis are above the assumptions of ESA.*

6 Summary and Outlook

In this thesis a digital phasemeter suitable to measure the phase of the LISA heterodyne signals with frequencies between 2 and 20 MHz with microradian precision is investigated. This phasemeter is based on a DPLL (Digital Phase Locked Loop) implemented on an FPGA (Field Programmable Gate Array) chip located on a PCB (Printed Circuit Board).

The first functionality tests showed that the system is capable of tracking an electrically generated RF input signal while delivering its correct frequency value. It was further demonstrated that a phase modulation (0.5 rad amplitude) of an input signal can be detected with the correct amplitude.

The next steps were to investigate and to improve the sensitivity of the system. The required phase sensitivity has to be below $6\,\mu\mathrm{rad}/\sqrt{\mathrm{Hz}}$ corresponding to $1\,\mathrm{pm}/\sqrt{\mathrm{Hz}}$. For this purpose differential phase measurements with split input signals (zero measurements) were performed.

For measurements excluding the noise contributions of the analog front end by splitting the input signal *behind* the transformers the ADC (Analog-to-Digital Converter) time jitter was identified as the limiting noise source for Fourier frequencies below a few Hz. At higher Fourier frequencies digitising noise was dominating. To correct for the time jitter noise in post-processing a pilot tone was simultaneously injected into the input channels to measure the differential time jitter between the two channels under investigation. This information was used to perform a jitter correction of the signals of interest in post-processing. It was shown that by implementing this correction scheme the requirements were met for the whole frequency range of interest. This type of measurements was carried out also with input signals generated by optical beat-notes of two phase-locked Nd:YAG NPRO lasers. The resulting phase noise was below the requirements.

The corresponding measurement performed with beat-notes of two free running lasers showed excess phase noise above the requirements.

The next step was to extend the noise investigations by including the analog front end electronics, i.e., the ADC driving units, as potential noise sources. After several measurements both the recommended transformers and a capacitive coupling scheme were excluded from further investigations due to severe disadvantages. Either these schemes did show unsatisfying noise behaviour or they turned out to be unsuitable to properly drive the ADCs. It was shown that a front end design using differential operational amplifiers implemented on a PCB daughter board had sufficiently low noise contribution. The differential phase noise of the system including this analog front end met the requirements over the whole frequency range of interest (10^{-4} to 1 Hz) for beat-note frequencies between 2 and 20 MHz.

A further step was to determine the sensitivity of the phasemeter with respect to modulated input signals.

A frequency modulation on a 7 MHz input signal showed up in a 'common mode

peak' at the modulation frequency in the noise spectrum. It could be successfully removed by applying a time-delay correction on the time series of the measured frequency of one channel.

Measurements with amplitude modulated input signals at a fixed signal frequency showed a surprising result. Peaks appeared in the noise spectrum at the modulation frequency and its harmonics partly exceeding the requirements. This peaks could not be removed by any correction scheme. The reason for this behaviour might be variations in the open loop gain of the system, that linearly depends on the input amplitude, or nonlinear behaviour of other components.

A noise measurement using a frequency modulated 17 MHz input signal showed a behaviour comparable to the noise obtained for the pure amplitude modulation. Here the peak at the modulation frequency could be removed by time-delay correcting the respective timeseries of the phasemeter output. The remaining peaks might be caused by a change in the input amplitude induced by the frequency modulation.

One of the measurement using modulated input signals had the purpose to show that the system is capable of detecting an asymmetric phase modulation on a LISA-like drifting input signal. This experiment was implemented and carried out successfully. The detected phase modulation had an amplitude of $3 \cdot 10^{-7}$ rad rms.

Finally an experiment was performed to determine the frequency noise of a free running Nd:YAG NPRO laser between 1 and 20 MHz Fourier frequency by means of a balanced detector. The measured frequency noise showed a broad peak with maximum height at about 2 MHz Fourier frequency. It might be caused by resonances (e.g., laser piezo), coupling of amplitude noise into the phase measurement (if the detector input was not exactly balanced) or uncertainties in the determination of the detector's transfer function. The lowest limit of the obtained noise curve could be the Schawlow-Townes limit of the lasers which is flat in frequency.

The excessive phase noise of the measurements with input obtained from the beatnote of two free running lasers could not be explained in the framework of this thesis. According to the results obtained by performing measurements with amplitude and frequency modulated input signals this noise might be caused by the frequency noise of the free running lasers being present in the input of the phasemeter. Another reason might be the asymmetry of the signal lines after the transformers resulting in a delay between the input signals at each ADC. The measurements should be repeated using the operational amplifier front end design since it has been proven to deliver best performance results. The investigations with respect to these measurements are currently ongoing at the AEI and improvements were already achieved.

The sensitivity measurements performed with unmodulated input signals presented in this thesis can be regarded as excellent basis for further investigation. In particular the implementation of a hexagon interferometer to perform a 3-signal measurement to test the linearity of the phasemeter is currently ongoing at our institute.

Bibliography

[1] Saulson, Peter R.: *Fundamentals of Interferometric Gravitational Wave Detectors*, World Scientific, 1994

[2] Blair, D.G.: *The detection of gravitational waves*, Cambridge Univ. Press, Reprinted, 1993

[3] Creighton, J.D.E. and Anderson, W.G.: *Gravitational-wave physics and astronomy: an introduction to theory, experiment and data analysis*, Wiley-VCH,2011

[4] Schutz, B.F.: *A First Course in General Relativity*, Cambridge Univ. Press, 2nd ed., 2009

[5] Schutz, B.F.: *Gravity from the ground up*, Cambridge Univ. Press, 3.print., 2005

[6] Schutz, B.F. and Ricci, F.: *Gravitational Waves, Sources and Detectors*, arXiv:1005.4735v1, 2010

[7] Misner, C.W., Thorne, K.S., Wheeler, J.A.: *Gravitation*, San Francisco: Freeman, 1973

[8] Ryder, L.H.: *Introduction to General Relativity*, Cambridge Univ. Press, 2009

[9] Schröder, U.E.: *Gravitation*, Verlag Harri Deutsch, 2007

[10] Pitkin, Reid, Rowan, Hough: *Gravitational Wave Detection by Interferometry (Ground and Space)*, Living Rev. Relativity, 2011

[11] Bronstein, Semendjajew: *Taschenbuch der Mathematik*, Teubner

[12] Pedroni, V.A.: *Circuit Design with VHDL*, MIT Press, 2004

[13] DiStefano, J.J.: *Schaum's Outline of theory and problems of feedback control systems*, 2nd ed., McGraw-Hill, 1990

[14] Lyons, R.G.: *Understanding digital signal processing*, 2nd ed., Prentice Hall PRT, 2004

[15] ESA Science & Technology: *NGO Revealing a hidden Universe: opening a new chapter of discovery*, assessment study report,
`http://sci.esa.int/science-e/www/object/index.cfm?fobjectid=49839`,
2011

[16] ESA Science & Technology: *LISA Unveiling a hidden Universe*, assessment study report,
`http://sci.esa.int/science-e/www/object/index.cfm?fobjectid=48364`,
2011

[17] ESA: *LISA Metrology System LISA-EST-SOW-848*, 2010

[18] Jennrich, O.: *LISA technology and instrumentation*
Class. Quantum Grav. 26 , 2009

[19] EADS-Astrium: *Requirement Breakdown, LISA-ASD-TN-5001*, 2007

[20] T. Prince, K. Danzmann, : *LISA Science Requirement Document, LISA-ScRD-004*, 2007

[21] ESA: *LISA: A Cornerstone Mission for the Observation of Gravitational Waves*, 2000

[22] Larson, S.L. et al.: *Sensitivity curves for spaceborne gravitational wave interferometers, Physical Review D, Vol 62*, 2000

[23] Tinto, M. et al.: *Implementation of time-delay interferometry for LISA*, Physical Review D 67, 2003

[24] Esteban, J.J. et al.: *Ranging and phase measurement for LISA*, Journal of Physics: Conference Series 228, 2010

[25] Esteban, J.J.: *Laser ranging and data communication for the laser interferometer space antenna*, Ph.D. Thesis, University of Hannover, 2012

[26] Morrison, E. et al.: *Experimental demonstration of an automatic alignment system for optical interferometers*, Applied Optics Vol. 33 No. 22, 1994

[27] Morrison, E. et al.: *Automatic alignment of optical interferometers*, Applied Optics Vol. 33 No. 22, 1994

[28] Pollack, S.E. et al.: *Demonstration of the zero-crossing phasemeter with a LISA test-bed interferometer*, Class. Quantum Grav 23, 2006

[29] Heinzel, G. et al.: *The LTP interferometer and phasemeter*, Class. Quantum Grav 21, 2004

[30] Heinzel, G. et al.: *Interferometry for the LISA technology package (LTP) aboard SMART-2*, Class. Quantum Grav 20, 2003

[31] Jennrich, O. et al.: *Interferometry developments for LISA and SMART-2*, Class. Quantum Grav 19, 2002

[32] Wand, V. : *Interferometry at low frequencies: Optical measurements for LISA and LISA Pathfinder*, Ph.D. Thesis, University of Hannover, 2007

[33] Wand, V. et al.: *LISA Phasemeter development*, AIP Conference Proceedings 873, 2006

[34] Bykov, I. et al.: *LISA phasemeter development: Advanced prototyping*, Journal of Physics: Conference Series 154, 2009

[35] Shadock, D. et al.: *Overview of the LISA Phasemeter*, AIP Conference Proceedings 873, 2006

[36] Thorpe, J.I. et al.: *Benchtop Models of LISA Interferometry at the University of Florida*, Class. Quantum Grav. 23, 2006

[37] Gardner, F.M.: *Phaselock Techniques*, 3rd ed, Wiley-Interscience, 2005

[38] Crawford, J.A.: *Advanced Phase-Lock Techniques*, Artech House, 2008

[39] Heinzel, G., Rüdiger, A., Schilling, R.: *Spectra by FFT, windows and new flat-top windows*, AEI Hannover, 2002

[40] Widrow, B. and Kollar, I.: *Quantization noise*, Cambridge Univ. Press, 2008

[41] Kane, T.J., Byer, R.L: *Monolithic, unidirectional single mode Nd:YAG ring laser*, Optics Letters Vol.10, 1985

[42] Freitag, I. et al.: *Power scaling of diode-pumped monolithic Nd:YAG lasers to output powers of several watts*, Optics Communication 115, 1995

[43] Zho, B. et al.: *Efficient, frequency-stable lase-diode-pumped Nd:YAG laser*, Optics Letters Vol.10, 1985

[44] Troebs, M. et al.: *Frequency stabilization and actuator characterization of an ytterium-doped distributed-feedback fiber laser for LISA*, J. Opt. Soc. Am. B, Vol. 26, 2009

[45] Troebs, M. et al.: *Lasers for LISA: overview and phase characteristics*, J. Phys.: Conf. Ser. 154, 2009

[46] Harb, C.C et al.: *Suppression of the Intensity Noise in a Diode-Pumped Neodymium:YAG Nonplanar Ring Laser*, IEEE Journal of Quantum Electronics Vol.30, 1994

Acknowledgements

I am very grateful to Karsten Danzmann who gave me the opportunity to do my PhD research at the AEI in Hannover. He always took the time when I needed to discuss important things and he always found the right, motivating words when things were not running as desired.

My gratitude also goes to Gerhard Heinzel. His extensive scientific knowledge (sometimes still a miracle to me) was of great help and the discussions with him usually lead to problem-solving insight.

Many thanks to Søren Brandt for being the second referee of this thesis (though informed short in time).

Thanks also to Jakob Flury and Wolfgang Meyer for being members of the board of examiners.

My special thanks go to Iouri Bykov for introducing me to the subject and for his support during my scientific work. His experience in analog and digital electronics was of great value.

I would also like to thank Michael Tröbs and Benjamin Sheard for many fruitful discussions in many situations where I had not much experience.

Thanks to Simon Barke for his help on experimentally mimicking gravitational wave signals and for providing his (partly self-made) devices to perform the corresponding measurements.

The support of the IT department (Konrad Mors, Dierk Linsenmaier, Guido Conrad, Claus Ebert and Stephan Herdam) and that of our electronics workshop (Andreas Weidner, Heiko zur Mühlen, Philipp Kormann and Hans-Jörg Hochecker) was a great help.

I am also grateful to Kirsten Labove, Brigitte Gehrmann and Klaus Haupt for helping me to organise many things apart from actual scientific work.

For proofreading of this thesis I would like to thank Gerhard Heinzel, Michael Tröbs, Markus Otto and Iouri Bykov. Your remarks were of great value to improve this thesis. Thank you very much! All remaining errors are, of course, my own responsibility.

Finally I would like to thank Allan Hornstrup, Søren Brandt, Søren Møller Petersen (DTU), Anders Engaard, Rolf Ostergaard, Torben Rasmussen, Torben Vendt Hansen (Axcon), Jens Reiche, Juan Jose Esteban Delgado, Oliver Gerberding, Simon Barke, Iouri Bykov and Gerhard Heinzel (AEI). It was a great pleasure to be a member of this unique team!

Lebenslauf

persönliche Daten

Name:	Kullmann
Vornamen:	Joachim Wolfgang Robert
Geburtsdatum:	19.10.1970
Geburtsort:	Großburgwedel

Schulausbildung

1977-1981:	Grundschule, Burgdorf
1981-1983:	Orientierungsstufe, Burgdorf
1983-1990:	Gymnasium, Burgdorf; Abitur

Tätigkeiten vor dem Studium

1990-1992:	Wehrdienst in Hannover

Studium

WS 1992/93:	Beginn des Physik-Studiums, Uni Hannover
WS 2005/06:	Studienunterbrechung
SS 2006:	Wiederaufnahme des Studiums, Uni Hannover
SS 2007:	Studienabschluß am AEI Hannover
2008-2012:	Promotionsstudium am AEI Hannover